工學博士學位論文

Fabrication of ruthenium/conducting polymer hybrid nanoparticle and its application as hydrogen chemical sensor

루테늄/전도성 고분자 하이브리드 나노입자 제조 및 수소 화학센서로의 응용

2019年 8月

서울大學校 大學院

化學生物工學部

吳 廷 均

Fabrication of ruthenium/conducting polymer hybrid nanoparticle and its application as hydrogen chemical sensor

by

Jungkyun Oh

Submitted to the Graduate School of Seoul National University in Partial Fulfillment of the Requirements for the Degree of Doctor of Philosophy

August, 2019

Thesis Adviser: Jyongsik Jang

Abstract

Recently, nanomaterial research receives attention due to excellent physical and chemical properties and electrical characters. Especially, inorganic and organic components hybrid nanomaterials are researched in various industrial areas because each component complements weaknesses and strengthens advantages. In particular, hybrid nanomaterials with metal and conducting polymer prevent poor mechanical properties such as brittleness and deficient processibility of polymeric nanomaterials and lack of stability due to the Ostwald ripening process of low dimensional metal nanaomaterials. Also, the combination of metallic materials with polymeric compounds provides an excellent functionality with high performance as well as enhanced stability and good processability. However, the limitation of applied metal, only Pt, Au, and Ag, and fabrication method of uniform hybrid nanomaterials are important tasks for researchers.

Smart chemical sensor is transducer based device which has excellent performance to detect environmental elements. It needs sensing materials to detect target analyte which display electrical, thermal, or optical signal change by target analyte. High-performance

sensing transducer is absolutely wanted because the sensor has to preindicate combustible, flammable, and toxic gases, monitoring air-fuel ratio in combustion engines, detecting food spoilage, and ambient oxygen level monitoring to prevent dangerous situations in diverse industrial environments. There are six standards to decide high-performance sensing transducer: 1) low minimum detectable level (MDL) to target analyte; 2) Wide detection range; 3) Selectivity; 4) Fast response and recovery time; 5) Cycle stability; 6) Sensing ability at room temperature.

This dissertation describes facile and creative method to fabricate ruthenium nanoclusters decorated carboxylic polypyrrole nanoparticles, studies electrical and structural characters of composites scienctifically, and suggests them as sensing transducer for hydrogen sensor.

First, carboxyl functional groups included polypyrrole nanoparticles (CPPyNPs) were fabricated by microemulsion. Then, ultrasonication and chemical reducing agent methods were used to embed ruthenium nanoclusters, reduced from ruthenium precursors, on the surface of carboxylated polypyrrole nanoparticles. Furthermore, the density of ruthenium nanoclusters on the CPPyNP surface was controlled by

injected ruthenium precursor concentration and the effect of variable ruthenium densities on CPPyNP surface for hydrogen sensing performance was analyzed. As a result, higher ruthenium density on CPPyNP surface showed lower minimum detectable level and wider detecting range for hydrogen gas detection.

Second, chemical treatment by acid and base aqueous solvents was processed to Ru/CPPyNPs and structural changes of ruthenium nanoclusters and CPPyNPs were observed. There was no transition in ruthenium nanoclusters. However, polypyrrole polymer chain was reversibly changed among neutral, polaron, and bipolaron states by treatment of acid and base aqueous solvents. Hence, the response and recovery times of hydrogen gas detection were changed due to transition of charge carrier (hole) density and mobility in polypyrrole backbone structure.

At last, Ru/CPPyNPs application as sensing material for wireless chemical sensor was demonstrated because the wireless chemical sensor becomes important technology for future IoT age. Especially, passive RFID tag is focused for wireless sensor because no battery is needed for tag operation. Thus, miniaturization and adaptation of wireless sensor is practicable. For these purposes, oxygen plasma and

silane treatment were applied to the part of RFID tag to introduce amino functional groups and these groups were connected with carboxyl functional groups on CPPyNPs rigidly and stably. As a result, the reflectance change by hydrogen gas was displayed and the amount of change was differed from various hydrogen gas concentrations.

Clearly, this dissertation proves the facile fabrication of ruthenium nanoclusters uniformly decorated carboxylated polypyrrole nanoparticles and the possibility of application for hydrogen chemical sensor and wireless sensor. The facile and creative hybrid nanocomposites fabrication method and chemical treatment to modify structural chain are expected to utilize for fabrication of other nanomaterials.

Keywords: Hybrid nanomaterial; polypyrrole; ruthenium; smart chemical sensor; wireless sensor; hydrogen gas

Student Number: 2014-22613

List of Abbreviations

A: ampere

AAO: anodic aluminium oxide

AFM: atomic force microscopy

APS: ammonium persulfate

APTS: 3-aminopropyltrimethoxysilane

a.u.: arbitrary unit

cm: centi-meter

CP: conducting polymer

CPPyNP: carboxylated polypyrrole nanoparticle

dB: decibel

DMT-MM: 4-(4,6-Dimethoxy-1,3,5-triazin-2-yl)-4-methyl-morpholinium chloride

DTAB: dodecyltrimethylammonium bromide

EMI: electromagnetic interference

eV: electronvolt

ex-situ: off-site conservation

FE-SEM: field-emission scanning electron microscopy

FET: field-effect-transistor

FT-IR: Fourier-transform infrared spectroscopy

g: gram

GHz: gigahertz

h: hour

hcp: hexagonal close packed

HF: high-frequency

HOMO: the highest occupied molecular orbital

HR-TEM: high resolution transmission electron microscopy

I: current

IC: integrated circuit

IDA: interdigitated micro array

in-situ: in-site conservation

kHz: kilohertz

LED: light-emitting diode

LF: low-freqeuncy

LUMO: the lowest occupied molecular orbital

M: molar concentration

MDL: minimum detectable level

MFC: mass flow controller

MHz: megahertz

min: minute

ml: milliliter

M_w: molecular weight

NC: nanocube

NCIRF: national center for inter-university research facilities

nm: nanometer

NP: nanoparticle

PANI: polyaniline

PC: polycarbonate

PEDOT: poly(3,4-ethylenedioxythiophene)

pH 1_Ru/CPPyNP: pH 1 aqueous solvent treated Ru/CPPyNP_3.0

pH 10_Ru/CPPyNP: pH 10 aqueous solvent treated Ru/CPPyNP_3.0

pH 13_Ru/CPPyNP: pH 13 aqueous solvent treated Ru/CPPyNP_3.0

pH 4_Ru/CPPyNP: pH 4 aqueous solvent treated Ru/CPPyNP_3.0

pH 7_Ru/CPPyNP: pH 7 aqueous solvent treated Ru/CPPyNP_3.0

pH: potential of hydrogen

pOH: potential of hydroxide

ppm: part of million

PPy: polypyrrole

PT: polythiophene

PVA: polyvinyl alcohol

Re: reflectance

RFID: radio frequency identification

rpm: revolutions per minute

RT: room temperature

Ru/CPPyNP: ruthenium nanoclusters decorated carboxylated polypyrrole nanoparticle

Ru/CPPyNP_0.5: Gravimetric ratio of $RuCl_3$: CPPyNP = 0.333 : 1

Ru/CPPyNP_1.5: Gravimetric ratio of $RuCl_3$: CPPyNP = 0.5 : 1

Ru/CPPyNP_3.0: Gravimetric ratio of $RuCl_3$: CPPyNP = 1 : 1

Ru/CPPyNP_4.0: Gravimetric ratio of $RuCl_3$: CPPyNP = 1.333 : 1

Ru/CPPyNP_5.0: Gravimetric ratio of $RuCl_3$: CPPyNP = 1.667 : 1

Ru: ruthenium

S: electrical conductivity

s: second

SD: source-drain

TEM: transmission electron microscopy

UHF: ultrahigh-frequency

V: voltage

VLSI: very-large-scale integration

vol%: volume percentage

wt%: weight percent

XPS: X-ray photoelectron spectroscopy

XRD: X-ray diffraction

1-D: one dimensional

3^{rd}: third

μm: micro-meter

%: percent

℃: celsius degree

List of Figures

13_Ru/CPPyNP).

Figure 36. (a) Normalized resistance change upon sequential exposure to various concentrations of hydrogen gas, (b) Sensitivity change upon sequential pH difference with same hydrogen concentration, and (c) Calibration line as function of hydrogen gas concentration (black: pH 1_Ru/CPPyNP; red: pH 4_Ru/CPPyNP; blue: pH 7_Ru/CPPyNP; magenta: pH 10_Ru/CPPyNP; green: pH 13_Ru/CPPyNP).

Figure 37. (a) Response and (b) recovery time of acid or base treated Ru/CPPyNPs with 100 ppm concentration hydrogen gas (black: pH 1_Ru/CPPyNP; red: pH 4_Ru/CPPyNP; blue: pH 7_Ru/CPPyNP; magenta: pH 10_Ru/CPPyNP; green: pH 13_Ru/CPPyNP).

Figure 38. (a) Normalized resistance changes of different hybrid CPPyNPs upon sequential periodic exposure to 1 ppm of hydrogen gas. (b) Sensitivity changes of hybrid CPPyNPs with periodic exposure to 1 ppm of hydrogen gas for 15 days (black: pH 1_Ru/CPPyNP; red: pH 4_Ru/CPPyNP; blue: pH 7_Ru/CPPyNP; magenta: pH 10_Ru/CPPyNP; green: pH 13_Ru/CPPyNP).

Re is the reflectance after the exposure time of 2 min.

Figure 44. Reflectance calibration curves of different Ru/CPPyNP based wireless sensors as a function of distances between sensor electrode and antenna reader (10 - 40 cm): (a) Ru/CPPyN_0.5; (b) Ru/CPPyNP_1.5; (c) Ru/CPPyNP_3.0 (black: 0.5 ppm; red: 1 ppm; blue: 5 ppm; magenta: 25 ppm; green: 100 ppm).

Figure 45. Changes in the reflectance properties of Ru/CPPyNP based wireless sensors with different pHs. Ru/CPPyNP_3.0 was commonly used for acid or base treatment: (a) pH 1 treated; (b) pH 4 treated; (c) pH 7 treated; (d) pH 10 treated; (e) pH 13 treated.

Figure 46. Reflectance calibration curves of different Ru/CPPyNP_3.0 based wireless sensors as a function of distances between sensor electrode and antenna reader (10 - 40 cm): (a) pH 1 treated; (b) pH 4 treated; (c) pH 10 treated; (d) pH 13 treated (black: 0.5 ppm; red: 1 ppm; blue: 5 ppm; magenta: 25 ppm; green: 100 ppm).

Figure 47. Photographs of the RFID tag sensor under different deformations (a) flat, (b) twisting and (c) rolling. (d) The

normalized reflectance change under different deformations (black: flat; red: twisting; blue: rolling).

Figure 48. (a) Relative change in the resistance of the UHF-RFID sensor tag with different bending angles (inset: photo images of diversely bended UHF-RFID sensor tag). (b) The resistance of the UHF-RFID sensor tag after repetitive foldings.

List of Tables

Table of Contents

1. Introduction

1.1 Background

1.1.1. Conducting polymer

During the last decades, conducting polymers (CPs) have instigated a lot of interests due to their superior electrical property, stability, and biocompatibility and from the viewpoint of both fundamental and applied studies by virtue of the exclusive natures originated from their unique π-conjugated system [1-2]. Since the discovery of polyacetylene in 1977, various kinds of conducting polymers have been continuously investigated, including polypyrrole (PPy), polyaniline (PANI), polythiophene (PT), and poly(3,4-ethylenedioxythiophene) (PEDOT) (**Figure 1**) [3]. Commonly, conducting polymers show polyconjugated chains consisting of alternating single (σ bond) and double (π bond) bonds, and these π-π conjugated systems play an important role in determining the electrical and optical properties of conducting polymers. According to the report, the significant parameters governing the physical properties of conducting polymers involve the conjugated length, the intra-/inter-chain interaction, and the extent of disorder.

Due to many advantages as the polymer characters and unique chemical/electrochemical properties, conducting polymers have been widely studied in applications including transistors, batteries, light-emitting diodes (LEDs), sensors, antistatic coatings, fuel cells, solar cells, and supercapacitors (**Figure 2**).

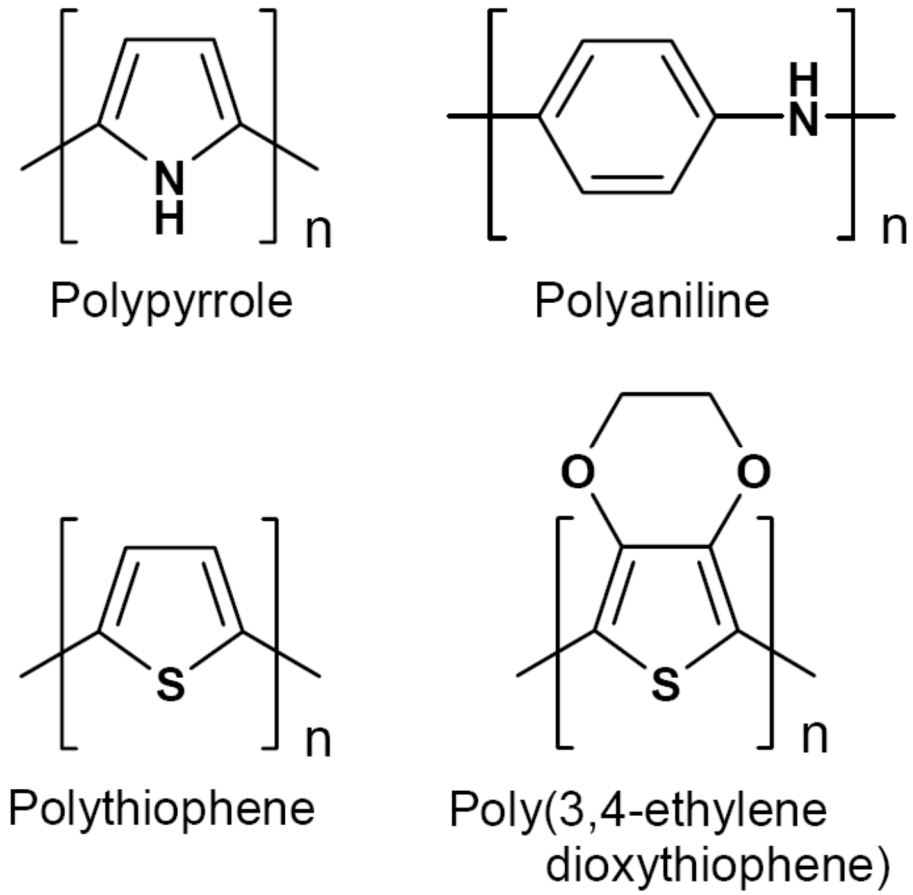

Figure 1. Molecular structures of representative conducting polymers [4].

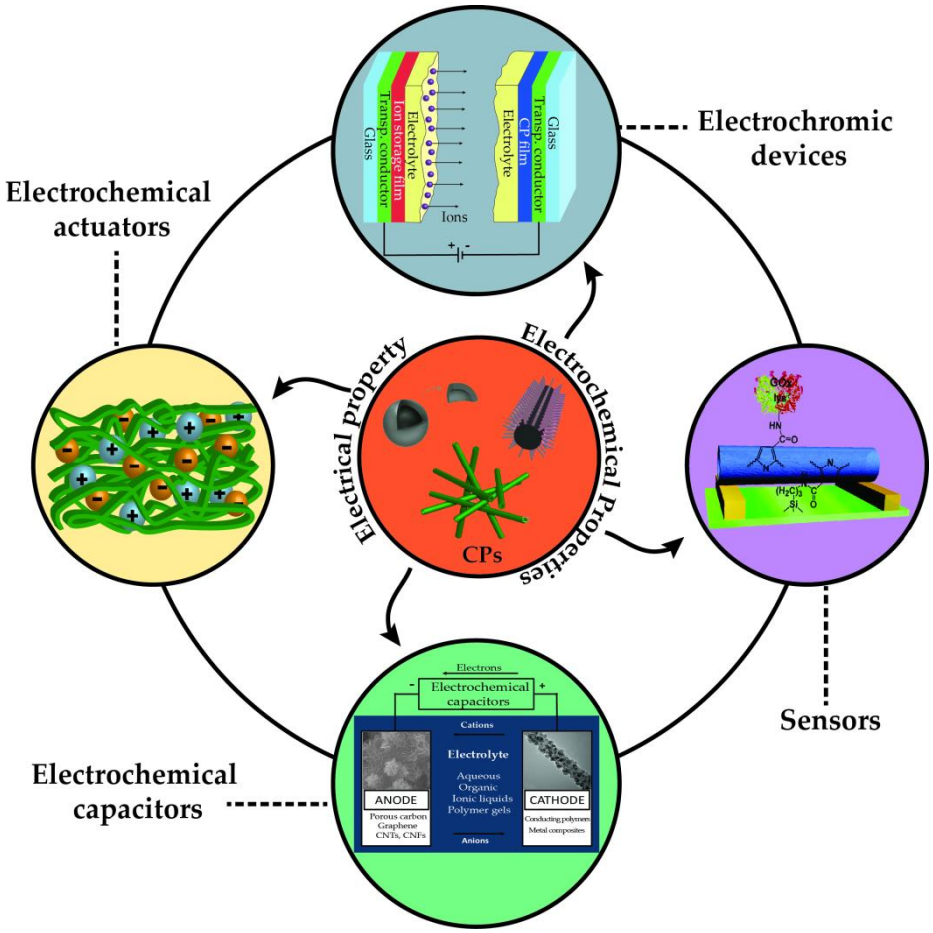

Figure 2. Applications of conducting polymers [5].

1.1.1.1. Doping

CPs have been doped using diverse methods in order to achieve high conductivities [6]. Their conductivities can change from insulator to metal upon doping states. Dopants in the polymer go under redox processes in which charges are transferred with subsequent formation of charge carriers [7]. The dopant of CPs not only withdraws electrons from the CPs, but also adds electrons to the CP backbone. For further explanation, electrons are extracted from the highest occupied molecular orbital (HOMO) of the valence band (oxidation) or transferred to the lowest occupied molecular orbital (LUMO) of the conduction band (reduction) during doping mechanism. The oxidation/reduction process creates charge carriers in the form of neutral, polaron (radical ions), or bipolaron (dications or dianions) in the polymer. The charge carriers along polymer chains produce conductivity and the oxidation and reduction processes of polymers correspond to *p*-type and *n*-type doping, respectively [8]. In *p*-type doping, the electron moves directly from the HOMO of the polymer to the dopant species and creates a hole in the polymer backbone [9]. On the other hand, electrons from the dopant species move to the LUMO of the polymer in *n*-type doping and it increases electron density [10].

Thus, the density and mobility of charge carriers can be controlled by doping [11].

As shown in **Figure 3**, CPs can experience both *p*-type and *n*-type doping. The doping process generates positive or negative polarons or bipolarons state. These charge carriers are delocalized over the polymer chains, which facilitate the electronic conductivity. Normally, the positively charged carriers in *p*-doping are more stable than negatively charged form, *n*-doping. As a result, *p*-doping is more popular in academic research for practical applications.

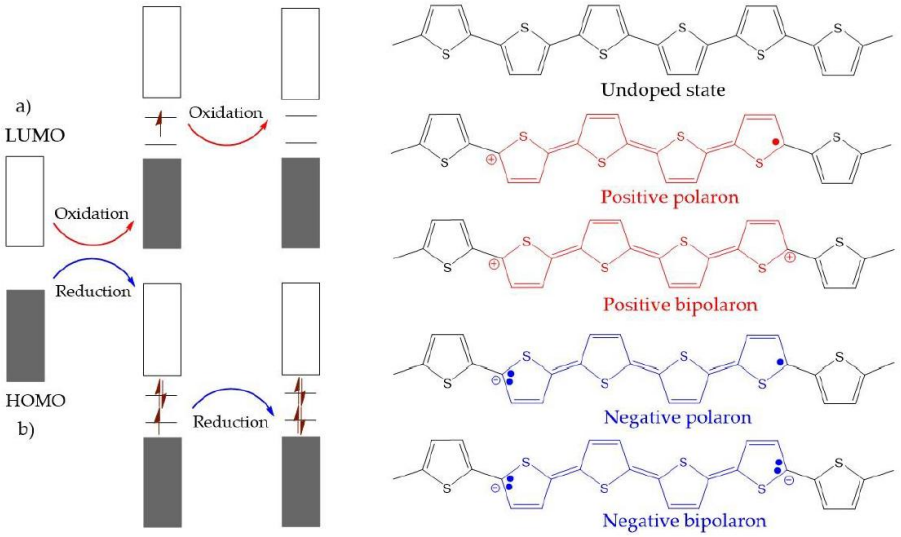

Figure 3. The electronic band and chemical structures of polythiophene (PT) with (a) *p*-type doping and (b) *n*-type doping [5].

1.1.1.2. Polypyrrole

Polypyrrole is one of the most well-known conducting polymers composed of five membered heterocyclic rings and represented beneficial characteristics including high electrical conductivity, redox property, and environmental stability [12]. Polypyrrole can be readily prepared by electrochemical and chemical approaches in both aqueous and non-aqueous solutions [13]. Electrochemical polymerization commonly occurs as films deposited on substrates. On the other hand, chemical polymerization produces as powders. The repeating units of polypyrrole are liked predominantly through α-α coupling and the polypyrrole chains are intrinsically planar and linear. However, many conformational and structural defects can be formed like **Figure 4** during polymerization process [14]. Conformational defects are α-α bondings with nonregular rotation and structural defects involve α-β bonds, hydroxyl groups, and carbonyl groups. The hydroxyl and carbonyl groups can be introduced into the polymer chain due to overoxdiation, and the α-β coupling leads to branching and crosslinking. These defects introduce structural disorders in the polymer chain and affect the conjugation length and conductivity.

Polypyrrole has four different electronic band structures by the

transition for doping level of the polypyrrole chain (**Figure 5**) [12, 15]. In the neutral state, polypyrrole is an insulator with a large π- π* band gap of *ca*. 3.16 eV. However, the polypyrrole chain is doped with counterions (mostly anions) to maintain electroneutrality during polymerization. When a negative charge is extracted from the neutral segment of polypyrrole chain by the doping process, a local deformation from benzenoid to quinoid structure occurs to form a polaron (a radical cation) (**Figure 6a** and **b**). The formation of a polaron gives rise to two localized electronic levels (bonding and antibonding cation levels) within the band gap while the unpaired electron occupies the bonding state (S = 1/2). As the oxidative doping proceeds further, another electron is removed from a polypyrrole chain, resulting in the formation of a double charged bipolaron (a dication S = 0) as described in **Figure 6c**. At higher oxidation level (a doping level of *ca*. 33 %), the overlap between bipolarons is occurred, leading the formation of two narrow bipolaronic bonds.

Doping properties of conducting polypyrrole can be altered by treatment with aqueous bases and acids [16-17]. The counter anion exchange process (Chemical compensation) and proton transfer process interpret this phenomenon. The protonic acid doping

conduction mechanism has been widely investigated and accepted in the case of polyaniline and similar mechanism is occurred in polypyrrole. Otherwise, proton transfer and irreversible change occur in polypyrrole due to strong base exposure.

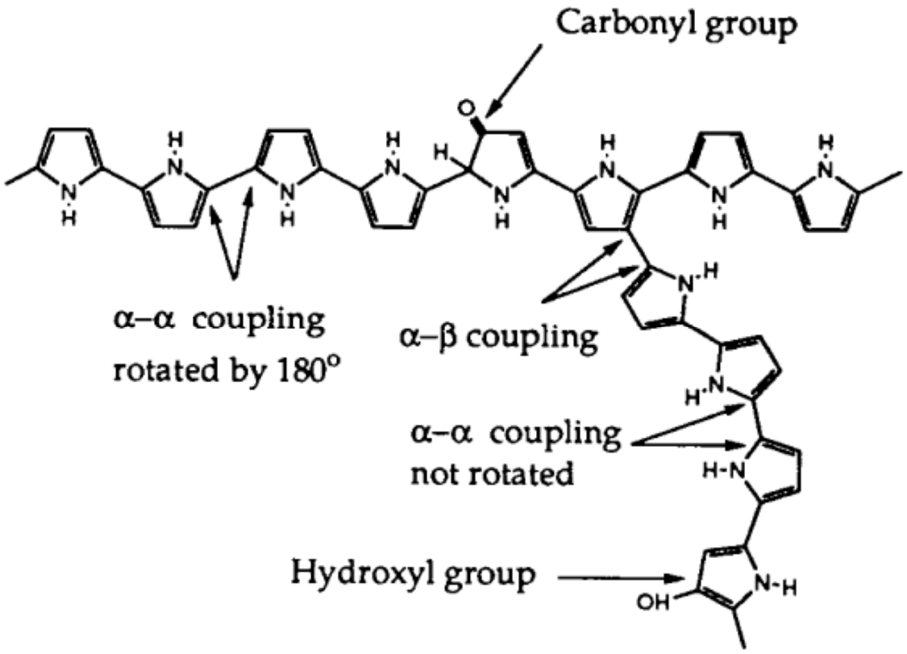

Figure 4. Possible chemical structures in polypyrrole chains [14].

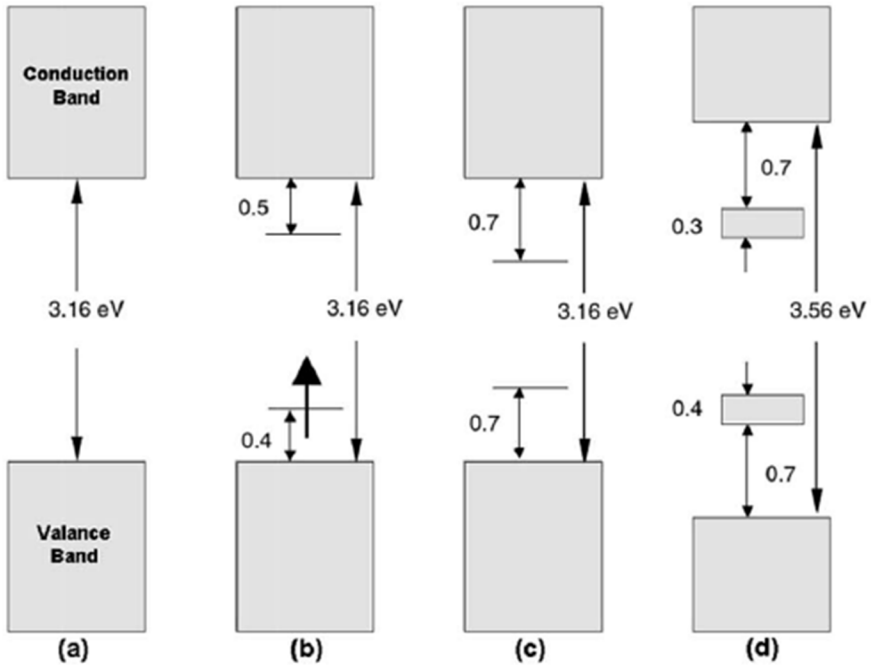

Figure 5. Electric energy diagrams for (a) neutral, (b) polaron, (c) bipolaron, and (d) fully doped polypyrrole [12].

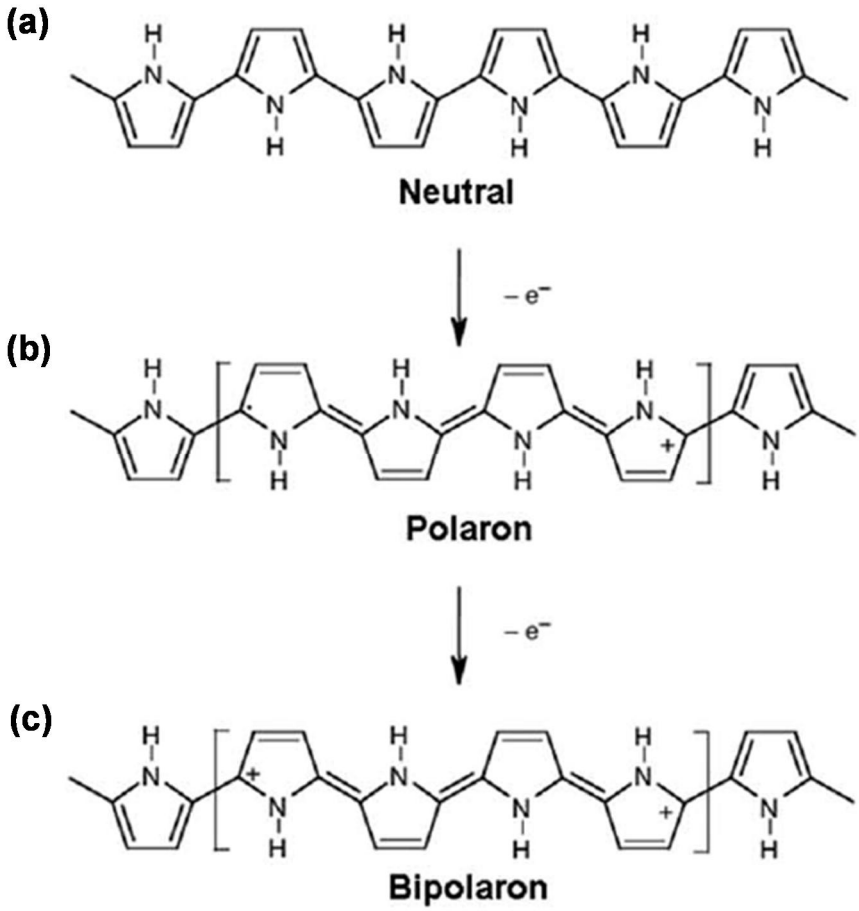

Figure 6. Electronic structures of (a) neutral, (b) polaron in partially doped, and (c) bipolaron in fully doped polypyrrole [12].

1.1.2. Nanomaterial

The development of material science and technology provides the smaller and smaller dimensions with higher precision and enhanced performance. Currently, nanotechnology is concerned with fabrication of functional materials and structures in the range of 1 - 100 nm using chemical and physical methods and application area of these nano-sized materials [18-20]. Size control of nanoscale material leads to superior physical and chemical properties with molecular and supermolecular structures. Assembling the nanostructures into the ordered array is necessary to render them functionally and operationally. Novel nanostructured materials and devices with the enhanced capabilities can be generated by the combination of nanobuilding units and strategies for assembling them. Nanomaterials include various morphologies such as nanoparticle, core-shell nanostructure, hollow nanosphere, nanofiber, nanotube, nanopattern, and nanocomposite, *etc* (**Figure 7**).

Nanomaterials are divided into nanosized metal, metal oxide, semiconductor, biomaterial, oligomer and polymer, *etc*. The widespread interest in nanostructured materials mainly originates from the fact that their properties (optical, electrical, mechanical and

chemical performance) are usually different from those of the bulk materials [21-22]. These phenomena arise from the quantum chemical effects including quantum confinement and finite size effect as well as the nano-sized filler effect [23]. The ability to selectively tune defects, electronic states, and surface chemistry has motivated the development of diverse methods to fabricate metallic, inorganic, and polymeric nanomaterials.

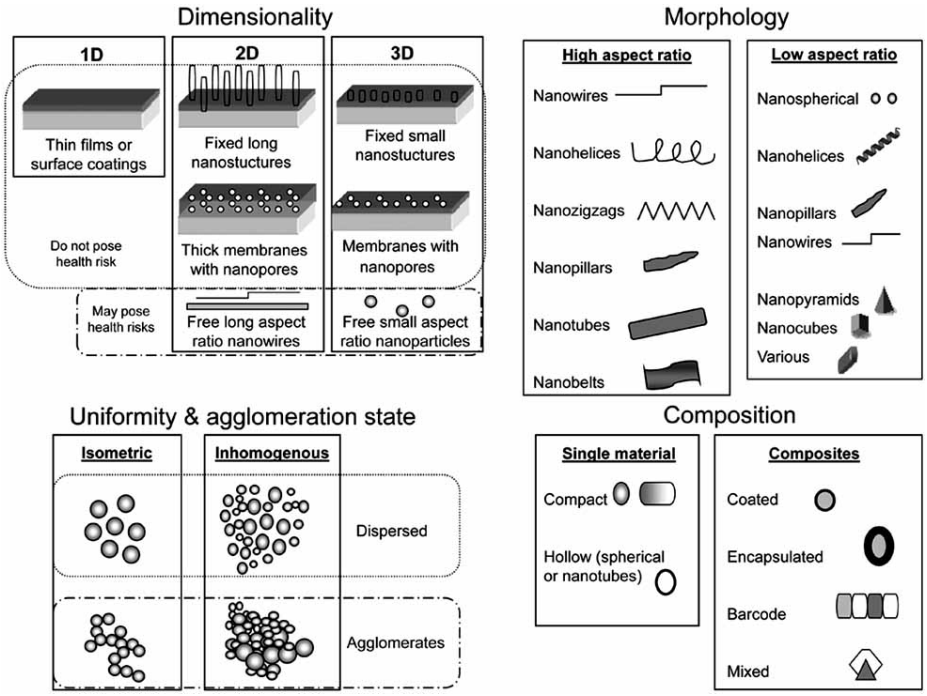

Figure 7. Dimensionality and morphology classification of nanomaterial [24].

1.1.2.1. Conducting polymer nanomaterial

Polymer nanomaterials have a variety of advantages over other nanomaterials because they have a wide range of source materials and tunable surface functionalities. Especially, conducting polymer nanomaterials receive great interest owing to their availability in diverse and important applications in current technology including electroluminescence, electromagnetic interference (EMI) shielding materials, photovoltaic cells, displays, supercapacitors, batteries, molecular wires, field-effect-transistors (FETs), and sensors, *etc* [25-28].

Many fabrication methods have been developed for conducting polymer nanomaterials. Among other synthetic strategies, template method is one of the promising and powerful tools to fabricate conducting polymer nanomaterials with diverse morphologies. Template method involves the inclusion of additives such as inorganic or organic constituents inside the void spaces of host material. These voids act as the template, deforming the shape, size, and orientation of the produced compound. In general, template method is classified into three types: hard template, soft template, and template free. Each method has intrinsic characteristics. First, hard template method is

good to control fabrication of 1-D nanostructures (*e.x.*, nanotube and nanorod) by using anodic aluminium oxide (AAO) membrane, track-etched polycarbonate (PC), or zeolite as template (**Figure 8**) [29-30]. Second, soft template method has been used for the fabrication of various morphologies for conducting polymer nanomaterials. There are several soft templates such as surfactant, liquid crystalline polymer, cyclodextrin, and functionalized polymer. Surfactants, which imply cationic, anionic and non-ionic amphiphiles, are mostly used for the formation of micelle as the nanoreactor among them [31-33]. The ratio of surfactants in solvent decides the void space of micelle and monomers of conducting polymer fulfill this void space to form morphology of nanomaterial (**Figure 9**). Also, the ratio of water and oil in solvent is related to the formation of micelle. Third, template-free technique has been extensively studied for the fabrication of conducting polymer nanomaterials. Compared to hard and soft template methods, this methodology provides a facile and practical route to produce pure, uniform, and highly qualified nanofibers. Template-free methods encompass various methods such as electrochemical synthesis, chemical polymerization, aqueous/organic

interfacial polymerization, radiolytic synthesis, and dispersion polymerization [34-36].

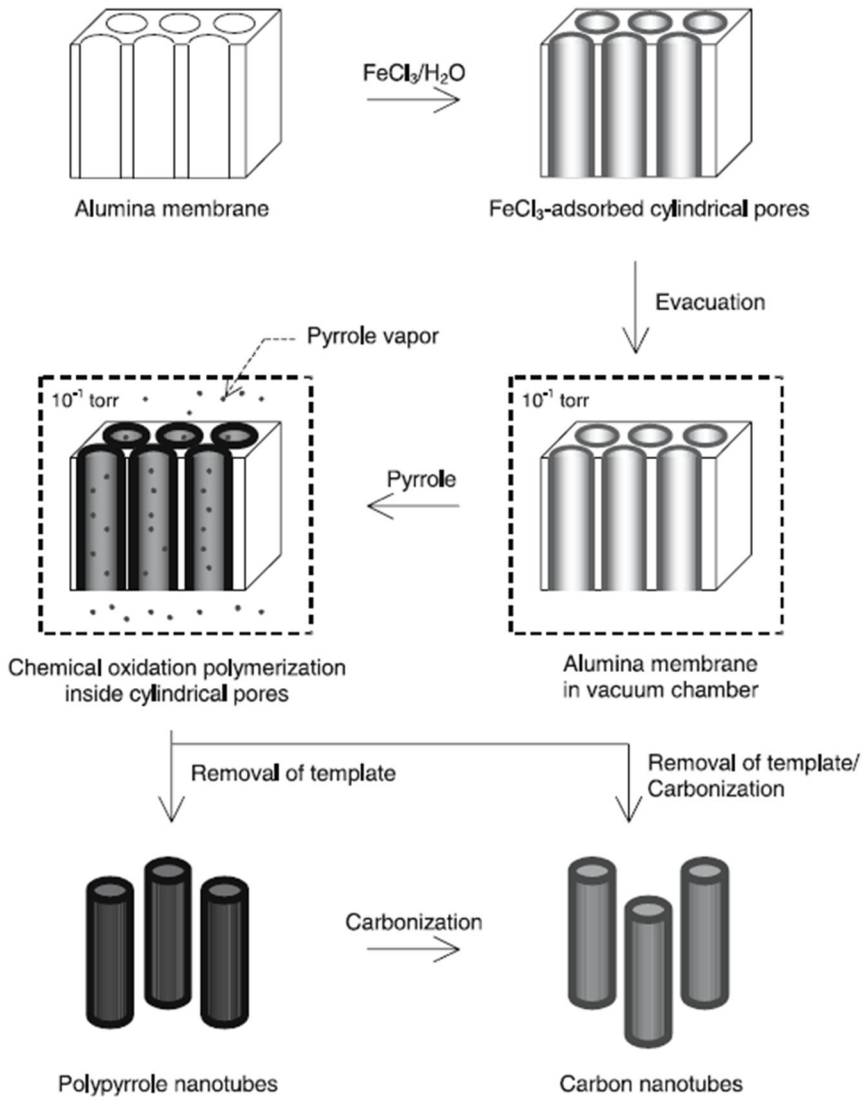

Figure 8. Fabrication of polypyrrole nanotube using hard template (AAO) method [12].

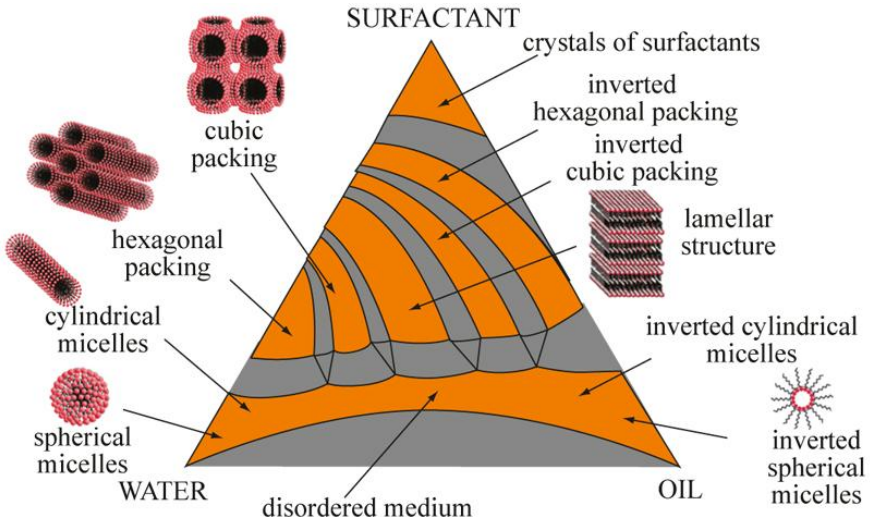

Figure 9. Phase diagram of surfactants [37].

1.1.2.1.1. Polypyrrole nanoparticle

Polypyrrole (PPy), one of the most promising conducting polymers, has been extensively challenged to fabricate nanoscale structures because of their easy synthesis, tunable conductivity, reversible redox property, and environmental stability. In particular, spherical PPy nanoparticles have been prepared by chemical oxidation polymerization with the aid of surfactant or stabilizer in aqueous solution. Above all, microemulsion polymerization has been extensively utilized to synthesize various nanometer-sized conducting polymer particles [38-40].

PPy nanoparticles with the diameter of 60 – 90 nm are polymerized with $FeCl_3$ as initiator and dodecyltrimethylammonium bromide (DTAB) as surfactant in aqueous solutions containing PVA as the stabilizer [41]. At room temperature (RT), the polymerization of pyrrole occurs at high rate. When the concentration of pyrrole increases, the resulting PPy nanoparticles become coarser with broad particle size distribution. Furthermore, the increase in concentration of PVA results in faster polymerization and finer PPy nanoparticles. Such a phenomenon is due to the reinforcement of the structural-mechanical barrier formed by the stabilizer at the surface of the nanoparticle,

preventing the growth of PPy nanoparticles during the polymerization process.

Transition of polymerization condition easily changes the size of PPy nanoparticles. Low temperature polymerization is appropriate to reduce the inner space of micelles by virtue of deactivating the chain mobility of the surfactant [42]. Thus, PPy nanoparticles as small as 2 nm in diameter can be prepared through chemical oxidation polymerization inside the micelles made of cationic surfactants at low temperature. As the polymerization temperature increases, PPy nanoparticle grows as a result of the enhanced chain mobility of the surfactant. Furthermore, the size of PPy nanoparticle decreases with shortening the chain length of the surfactant. The micelle aggregation number, which is defined as the number of surfactant molecules required to form a micelle, becomes smaller as the chain length of surfactant decreases. The reduced micelle aggregation number gives rise to the formation of smaller nanoparticles. On the other hand, the longer surfactant chains provide more free volume inside micelle, which leads to the increment of particle size. Importantly, the thermodynamically stable micelle acts successfully as the nanoreactor for synthesize of PPy nanoparticles.

1.1.2.2. Metal nanomaterial

Metal nanomaterials have revolutionized several applications in nanoscience including plasmonics, catalysis, sensing, electronics, photonics, information storage, medicine, energy conversion, cosmetics, among others [43-49]. Their high and tunable performance arises from the fact that properties in metal nanomaterials strongly correlate to their individual or combined physical and chemical features. For instance, properties are strongly dependent on composition (mono vs bimetallic), size (the effect of quantum confinement), geometric/shape (faceting or arrangement of atoms on the surface), and structure (hollow vs solid interiors). During the solution-phase synthesis of metal nanomaterials, all these parameters can be controlled so that, at least in principle, it is possible to optimize performances for the wealth of applications. As one of classical examples, controlling the shape of metal nanoparticle provides an effective strategy to control its catalytic properties.

There are two fundamental strategies used to prepare metal nanomaterials: bottom-up and top-down (**Figure 10**) [50]. The bottom-up approach is a basic technique to prepare metal nanostructures by reducing their ions and the growing of the nano-architectures is usually stopped by agent such as surfactant or

stabilizer. Bottom-up techniques include chemical reduction, photochemical reduction, electrochemical reduction, templating, and thermal methods [51-55]. On the other hand, the top-down approach involves removing materials from the bulk substrate to leave behind the desired nanostructures. Common top-down methods include photolithography, electron beam lithography, and nanosphere lithography [56-57].

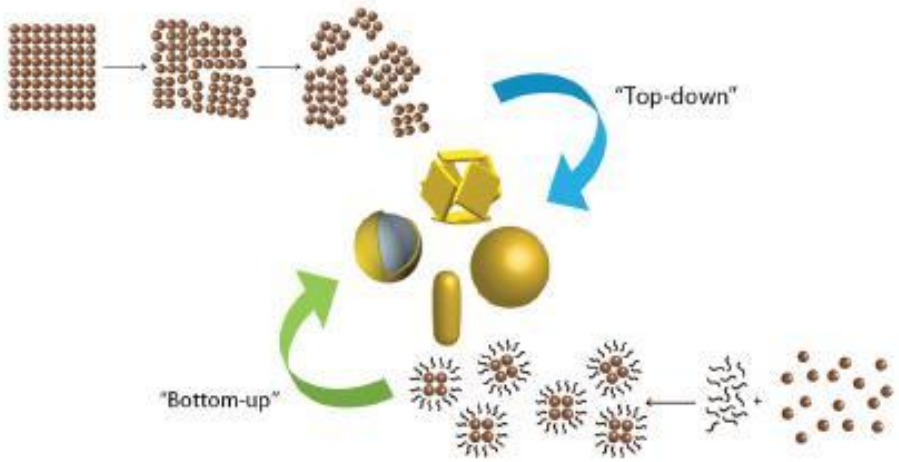

Figure 10. Top-down and bottom-up approaches for producing controlled nanomaterials [50].

1.1.2.3. Metal/conducting polymer hybrid nanomaterial

The synthesis of new materials with improved properties and performance is a continually expanding frontier at the material science. In general, polymeric nanomaterials themselves display poor mechanical properties such as brittleness and deficient processibility [58-59]. On the other hand, inorganic nanomaterials, such as metal and metal oxide, have lack of stability due to the Ostwald ripening process of low dimensional nanomaterials, leading to large aggregated nanoparticles [60-61]. The combination of inorganic materials with polymeric compounds provides an excellent functionality with high performance as well as enhanced stability and good processibility. Therefore, many efforts have been devoted to synthesize novel functionalized hybrid nanomaterials for their potential applications [62-63].

Metal/conducting polymer nanostructures have been extensively studied because of their potential applications ranging from electronic and optical devices to sensing and catalyst [64-66]. Generally, there are two synthetic approaches for the preparation of metal/conducting polymer nanostructures: in-situ and ex-situ methods [67]. The ex-situ method involves metal architecture formation first and dispersing

them into polymer matrix [68]. In the case of in-situ approach, metal nanoparticles can be coincidently generated inside polymer structure by reduction of metallic precursor which is dissolved into polymer or polymerizing solution [69].

1.1.3. Sensor application

Infrared spectroscopy and gas chromatography are highly accurate methods for analysis and detection of various gases and their mixtures. However, due to high cost, huge data sampling, and instrumental maintenance, application of these techniques for in-situ gas detection and monitoring in households and industry becomes unrealistic [70]. Thus, solid state sensors are being widely used for more than last two decades in many of these detection applications including detection of combustible, flammable, and toxic gases, monitoring air-fuel ratio in combustion engines, detecting food spoilage, and ambient oxygen level monitoring [71-74].

Sensor is a transducer device to detect some characteristic environmental elements. This device is composed of the active sensing material with signal transducer. The role of these two important components in sensor system is to transmit signal without any amplification from the selective compound or from the change in reaction. The sensor devices produce any one of the electrical, thermal or optical output signals, which could be converted to digital signals for subsequent processing.

There are several critical elements for highly effective sensor detecting system: 1) high sensitivity; 2) wide detection range 3) selectivity to target analyte; 4) fast response/recovery time; 5) cycle stability; and 6) low working temperature [75-76]. To satisfy these demands, nanomaterial based sensor electrode has been emerged as promising candidate on count of its small size such as high surface to volume ratio and unique optical/electrical properties. Recently, inorganic elements and CPs composite nanomaterials are suggested as sensing transducers to maximize sensitivity and selectivity for target analyte [77].

1.1.3.1. Resistive chemical sensor

Chemi-resistive gas sensing technology was introduced five decades ago by Seiyama who demonstrated gas sensing properties of ZnO thin films by incorporation into the simple electronic device [78]. Since then, it has witnessed tremendous research and advancement owing to low cost, ease of fabrication and ever contracting device size, with comparable sensing properties as compared to other gas sensing technologies.

Chemi-resistive gas sensing is simply based on the principle of change in electrical resistance of the device due to exchange of electrons between the analyte gas and the sensitive material, as depicted in **Figure 11**. Sensing occurs either at the surface or in the bulk of the material, leading to concentration dependent change in either charge carrier concentration or carrier mobility, which can be easily transformed into an electrical signal using a suitable transducer. Sensor sensitivity and selectivity is closely related to the resistance of the sensing material.

Chemi-resistive gas sensors can be distinguished as the one operating at high temperatures and others working at room temperature. High temperature is required to optimize charge carrier

densities and to achieve activation energy for grain boundary diffusion. On the other hand, low energy requirements for operation and higher stability have ushered in tremendous research in room temperature chemi-resistive gas sensors, especially those involving carbon and conducting polymer-based materials [79]. Advancements in the field of carbon and conducting polymer-based gas sensors have made fabrication of flexible sensors possible and it can be scalable to industrially required sizes [80-81]. Further, carbon ring-based sensing materials can be easily spin-coated onto the interdigitated electrodes or even ink-printed making sensor fabrication easier and economical [82-83]. Such sensors can also be incorporated into very-large-scale integration (VLSI) circuits [84].

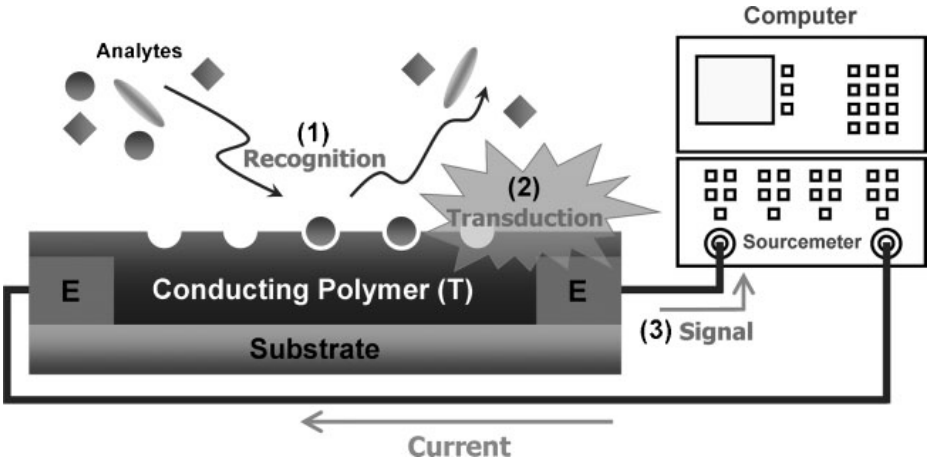

Figure 11. Schematic illustration of resistive chemical sensor [85].

1.1.3.1.1. Hydrogen gas sensor

Hydrogen is a non-poisonous, colorless, odorless, and tasteless gas that combusts in air to produce water. Also, hydrogen gas is widely used in industrial applications, including fossil-fuel production, chemical compound synthesis, power plant operation, and fuel-cell applications, *etc* [86-88]. Furthermore, hydrogen energy has received a great deal of attention for next-generation applications, such as hydrogen-based zero-carbon emission vehicles. However, due to wide explosive range of concentration (4 to 75 vol%), safe storage is a critical issue when working with hydrogen containing gases [89-90]. Additionally, hydrogen can cause asphyxiation with abnormal concentration in atmosphere. Thus, rapid and fast responsive hydrogen sensor with high sensitivity and selectivity is necessary to monitor hydrogen concentration levels [91-92].

1.1.3.2. Wireless sensor

Wireless sensor is a device in which sensing electronic transducers are spatially and galvanically separated from their associated readout/display components. Compared to traditional tethered sensor, wireless sensor includes the non-obtrusive nature of its installation, higher nodal density, and lower installation cost without the need for extensive wiring [93-95]. These attractive features of wireless sensors facilitate its development toward measurements in a wide range of physical, chemical, and biological parameters of interest. Examples of currently available wireless sensors include devices for sensing of pH, pressure, and temperature in medical, pharmaceutical, animal health, livestock condition, automotive, and other applications [96-98]. Unfortunately, although there are a numerous practical applications, the available wireless gas sensors fall short of meeting emerging measurement needs in complex environments. In particular, existing wireless gas sensors cannot perform highly selective gas detection in the presence of high levels of interferences and cannot quantitate several components in gas mixtures.

1.1.3.2.1. RFID wireless sensor

Wireless gas sensors are based on different detection principles depending on the type of sensing materials and associated transducers used to provide the required sensitivity, selectivity, and stability of measurements [99-100]. In particular, the power requirements for different gas sensing transducers and sensing systems that have been adapted or could be adapted for wireless sensing. Depending on the available power for operation, there are two broad types of wireless sensors: active sensors and passive sensors.

Several representative examples of active and passive radio frequency identification (RFID) sensors are presented in **Figure 12**. The limiting form factor for active RFID sensors (**Figure 12a** and **b**) is the size of their power source [101]. The limiting form factor for passive RFID sensors is the antenna size (**Figure 12c-f**). Typical operating frequencies of RFID devices are 125 - 135 kHz (LF, low-frequency tags), 13.56 MHz (HF, high-frequency tags), 868 - 956 MHz (UHF, ultrahigh-frequency tags), and 2.45 GHz (microwave tags).

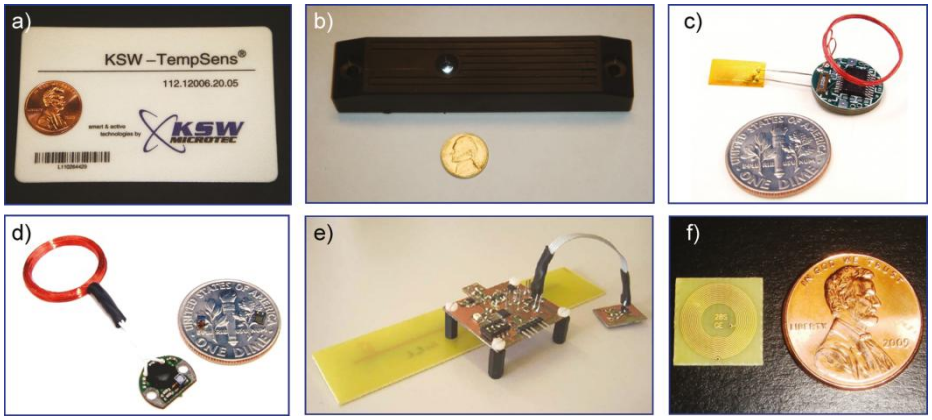

Figure 12. Examples of active and passive RFID sensors. Active sensors with (a) thin-film and (b) AAA-type batteries. Passive sensors with analog input into IC memory chip for operation at (c) LF, (d) HF, and (e) UHF frequency ranges; (f) passive sensor based on the common HF RFID tag with sensing material applied directly to the resonant antenna of the sensor [102].

1.2. Objectives and Outlines

1.2.1. Objectives

The aim of this dissertation is to describe the novel method for fabrication of ruthenium nanoclusters decorated carboxylated polypyrrole nanoparticles (Ru/CPPyNPs) and apply as chemiresistive hydrogen gas sensor. In detail, Ru/CPPyNPs are synthesized by simple chemical reducing process and optimized to obtain improved electrical ability for hydrogen gas detection. Furthermore, passive radio frequency identification (RFID) tag based gas sensor, wireless smart chemical sensor, is suggested as developed technology, offering a way forward for the future.

1.2.2. Outlines

This dissertation focused on the fabrication of Ru/CPPyNPs and investigation of their hydrogen gas detection ability as the chemiresistive smart sensor. This dissertation involves the following subtopics:

I. Ruthenium/polypyrrole hybrid nanoparticle for hydrogen chemical sensor

II. Acid-base treatment of Ru/CPPyNPs to control the chemiresistive properties of hydrogen chemical sensor

III. Wireless hydrogen sensor application of Ru/CPPyNPs

A detailed outline of the study is as follows:

I. Facile synthesis way of Ru/CPPyNPs is described to prepare transducer nanomaterial for high-performance hydrogen gas chemical sensor. Ru/CPPyNP is prepared via chemical reducing agent and ultrasonication method. Furthermore, the density of Ru nanoclusters on the CPPyNP surface is controlled by injected amount of Ru precursor in CPPyNP aqueous solution. Diverse microscopies and material analysis instruments are used to observe morphology change of Ru/CPPyNPs by increment of inserted Ru precursor concentration and confirm element composition. Also, the real-time responsive resistance changes are measured for different concentrations of hydrogen gas with variable viewpoints to test the performance of Ru/CPPyNPs as transducer for hydrogen gas detection.

II. As far as known, chemical treatment, treatment by acid and base solvents, provides structural transition of prisine conducting polymer backbone. Therefore, the structural change of metal/conducting polymer hybrid nanoparticles by acid and base aqueous solvents is confirmed both theoretically and experimentally in this part. To prove experimental results, various experimental analysis methods are used to observe backbone structure of Ru/CPPyNP. Further, Ru/CPPyNPs are exposed to hydrogen gas for constant and repeatable time to demonstrate the performance difference by treatment of acid and base solvents.

III. Wireless smart sensor for biological or chemical element detection is one of the important technologies for future industry. Especially, technology using passive RFID tag is focused due to no power requirement. Thus, the facile and fresh approach is proposed to combine Ru/CPPyNPs and ultrahigh frequency (UHF)-RFID tag for wireless hydrogen gas sensor. The combined RFID tag is exposed to hygrogen gas with different concentration and distance to observe the refletance signal change. Also, flexiblity test is examined to confirm the potential for wearable and flexible device.

2. Experimental Details

2.1. Ruthenium/polypyrrole hybrid nanoparticle for hydrogen chemical sensor

2.1.1. Materials

Poly(vinyl alcohol) (PVA, M_w 9000), $FeCl_3$ (97%), dodecyltrimethylammonium bromide (DTAB, ≥98%), pyrrole (98%), and $NaBH_4$ (≥98%) were purchased from Aldrich Chemical Company and used without further purification. Ammonium persulfate (APS, 98%) and pyrrole-3-corboxylic acid were purchased from Sigma-Aldrich Company and Acros Organics. Ruthenium (Ⅲ) chloride hydrate (99.98%) was acquired from Aldrich Chemical Company. 3rd distilled water was used as the solvent of polypyrrole.

2.1.2. Fabrication of ruthenium/polypyrrole hybrid nanoparticle

Uniform sized carboxylated polypyrrole nanoparticles (CPPyNP) with 65 nm diameter were prepared with PVA, $FeCl_3$, and the mixture of pyrrole and pyrrole-3-carboxylic acid monomers as following (**Figure 13**). A micro-emulsion method was used to obtain the carboxylated polypyrrole nanoparticles (CPPyNPs). To synthesize the

CPPyNPs, PVA was dissolved in distilled water to make 1 wt% PVA aqueous solution. This solution was stirred for 12 h at 60°C with uniform stirring rate. The DTAB and $FeCl_3$ powders were injected into the PVA aqueous solution simultaneously, which was then stirred for 1 h at the rate of 1,000 revolutions per minute (rpm). A pipette was used to add the aqueous solution of pyrrole and pyrrole-3-carboxylic acid hydrate monomers and the resulting mixture was rotated at 1,000 rpm for 2 h. This solution was centrifuged to remove reagents without removing resultants, then diluted with distilled water and stirred for 4 h at the rate of 400 rpm and the temperature of 60°C. After this process had been repeated five times, the solid CPPyNPs were placed in the 60°C oven to dry.

The prepared CPPy nanoparticles were dissolved in 60 ml distilled water at 0.05 wt% and ultrasonicated 0.5 h for mono-disperse state. 1 wt% $RuCl_3$ aqueous solution was added to CPPyNP aqueous solution and also ultrasonicated for 30 min. Then, 0.01 g of $NaBH_4$ powder was injected to mixed solution and the solution was stirred with 500 rpm for 3 h at 25℃. At last, the solution was centrifuged with water and ethanol several times to eliminate impurities. The solution was

dried for 12 h at 60℃ to form ruthenium/carboxylated polypyrrole nanoparticle (Ru/CPPyNP) powder.

2.1.3. Electrical measurement of Ru/CPPyNP attached chemiresistive sensor

To measure the electrical properties of the polymer coating, the aqueous Ru/CPPyNP solution was sonicated and drop-casted onto interdigitated micro array (IDA) electrode. Among diverse chemiresistive sensing systems, IDA-based chemiresistive sensors have several strengths to apply chemical sensing device (**Figure 14**). The spin-coating method at the rate of 1,000 rpm was used for duration of 60 s to obtain a uniformly coated electrode array. To reduce the resistance gap between IDA electrode and Ru/CPPyNPs, the coated electrode array was stored in inert atmosphere for 24 h at room temperature. To measure the influence of hydrogen (H_2) gas exposure on the electrical properties of the Ru/CPPyNP-coated IDA electrodes, they were placed in the vacuum chamber, which was customly designed for gas sensing with the vapor inlet/outlet pressure of 100 Torr. Various gas concentrations of hydrogen (0.5 - 100 ppm) were controlled by mass flow controller (MFC, KNH Instruments,

Pocheon, Korea) system. The real-time resistance monitoring was conducted with constantly applied current of 10^{-6} A and resistance change was defined by following equation.

$$S = \frac{\Delta R}{R_0} = \frac{(R - R_0)}{R_0}$$

S: sensitivity

R: real-time resistance

R_0: initial resistance

After the sensor electrode had been exposed to gas for several minutes, compressed inert gas was introduced to the vacuum chamber to remove any molecule that had become attached to Ru/CPPyNPs. This step refreshed the electrode, enabling its reuse, and hence repeated measurement of the sensor performance.

2.1.4. Characterization

Field-emission scanning electron microscopy (FE-SEM) and high resolution transmission electron microscopy (HR-TEM) images were obtained using a JEOL 6700 and a JEOL JEM-200CX (JEOL Ltd., Tokyo, Japan), respectively. Transmission electron microscopy (TEM) images were acquired by a JEM-2100 (JEOL) installed at the National Center for Inter-university Research Facilities (NCIRF) at Seoul

National University. X-ray photoelectron spectroscopy (XPS) spectra were recorded using M16XHF-SRA (Mac Science Co., Yokohama, Japan). X-ray diffraction (XRD) was obtained using M18XHF SRA (MAC Science Co.). The four-probe method was used to measure the electrical conductivity at ambient temperature with the source meter (Keithly Instruments Inc., Cleveland, OH, USA).

Figure 13. Schematic illustration of the formation of carboxylated polypyrrole nanoparticles in the aqueous PVA solution through dispersion polymerization [103].

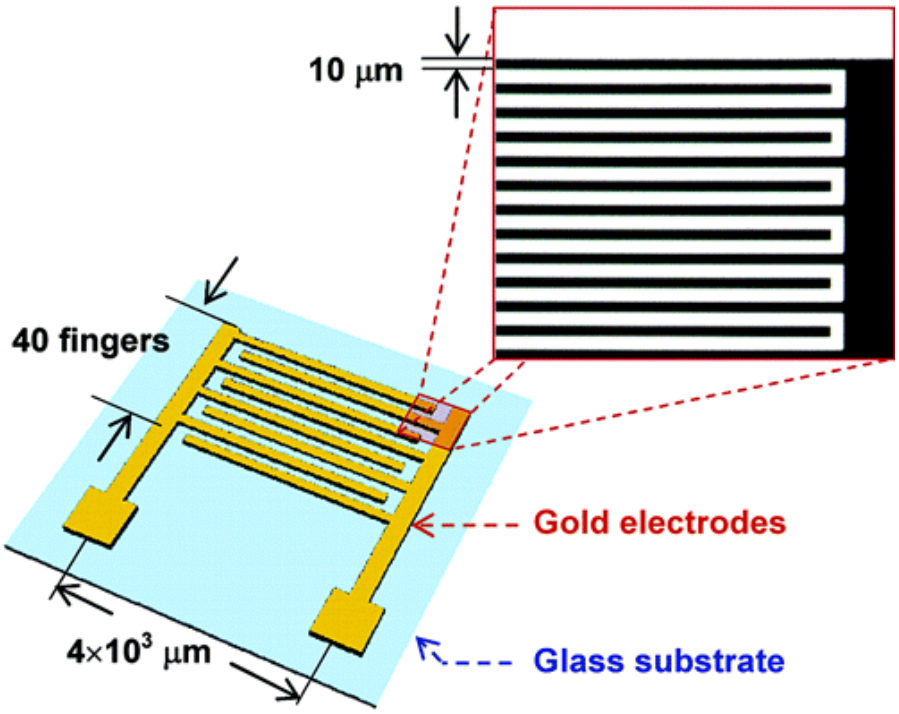

Figure 14. Schematic illustration and optical micrograph of the gold microelectrode array on glass substrate (finger dimensions: 10 μm width, 50 nm thickness, 4 × 10^3 μm length, 10 μm inter-electrode spacing) [104].

2.2. Acid-base treatment of Ru/CPPyNPs to control the chemiresistive properties of hydrogen chemical sensor

2.2.1. Materials

Poly(vinyl alcohol) (PVA, M_w 9000), $FeCl_3$ (97%), dodecyltrimethylammonium bromide (DTAB, ≥98%), pyrrole (98%), and $NaBH_4$ (≥98%) were purchased from Aldrich Chemical Company and used without further purification. Ammonium persulfate (APS, 98%) and pyrrole-3-corboxylic acid were purchased from Sigma-Aldrich Company and Acros Organics. Ruthenium (Ⅲ) chloride hydrate (99.98%) was acquired from Aldrich Chemical Company. Potassium hydroxide (NaOH, 95%) and hydrochloric acid (HCl, 35~37%) were purchased from Samchun pure chemical company. 3rd distilled water, maintaining accurate pH 7, was used as the solvent of polypyrrole.

2.2.2. Acid-base treatment of Ru/CPPyNPs

Amount of Ru/CPPyNP powder was injected in pH 1 and 4 buffer solution originated from hydrochloric acid commercial solution. Hydrochloric acid commercial solution was diluted by distilled water to make pH 1 and 4 buffer solution. Ru/CPPyNP powder dissolved

buffer solutions were sonicated for 3 h at room temperature to spread Ru/CPPyNP powder in buffer solution uniformly. Then, the solutions were stirred at vigorous speed for 12 h. Finally, the powder was isolated from solvent by centrifuge method and dried in 60℃ oven. Same procedures were repeated with pH 10 and 13 buffer solution made by potassium hydroxide commercial solution. Furthermore, to maintain pH 7 state with Ru/CPPyNP powder, we used 3rd distilled water.

2.2.3. Electrical measurement of acid-base treated Ru/CPPyNPs attached chemiresistive sensor

To measure the electrical properties of the polymer coating, the diverse Ru/CPPyNP acid and base solutions were sonicated and drop-casted onto an interdigitated micro array (IDA) electrode. The spin-coating method at the rate of 1,000 rpm was used for duration of 60 s to obtain a uniformly coated electrode array. To reduce the resistance between IDA electrode and Ru/CPPyNPs, the coated electrode array was stored in inert atmosphere for 24 h at room temperature. To measure the influence of hydrogen (H_2) gas exposure on the electrical properties of the Ru/CPPyNP-coated IDA electrodes, they were placed

in the vacuum chamber, which was customly designed for gas sensing with the vapor inlet/outlet pressure of 100 Torr. Various gas concentrations of hydrogen (0.5 - 100 ppm) were controlled by mass flow controller (MFC, KNH Instruments, Pocheon, Korea) system. The real-time resistance monitoring was conducted with constantly applied current of 10^{-6} A and resistance change was defined by following equation.

$$S = \frac{\Delta R}{R_0} = \frac{(R - R_0)}{R_0}$$

S: sensitivity

R: real-time resistance

R_0: initial resistance

After the sensor electrode had been exposed to gases for several minutes, compressed inert gas was introduced to the vacuum chamber to remove any molecules that had become attached to Ru/CPPyNPs. This step refreshed the electrode, enabling its reuse, and hence repeated measurement of the sensor performance.

2.2.4. Characterization

High-resolution transmission electron microscopy (HR-TEM) and transmission electron microscopy (TEM) images were obtained using

a JEOL JEM-200CX and a JEM-2100 (JEOL) (JEOL Ltd., Tokyo, Japan), respectively, installed at the National Center for Inter-university Research Facilities (NCIRF) at Seoul National University. FT-IR spectra were collected with PerkinElmer Frontier spectrophotometer in attenuated total reflection mode. Raman spectra were recorded with LabRam Aramis (Horiba Jobin Yvon) spectrometer. X-ray photoelectron spectroscopy (XPS) spectra were recorded using M16XHF-SRA (Mac Science Co., Yokohama, Japan). X-ray diffraction (XRD) was obtained using M18XHF SRA (MAC Science Co.). The four-probe method was used to measure the electrical conductivity at ambient temperature with the source meter (Keithly Instruments Inc., Cleveland, OH, USA).

2.3. Wireless hydrogen sensor application of Ru/CPPyNPs

2.3.1. Materials

The poly(vinyl alcohol) (PVA, M_w 9000), dodecyltrimethyl-ammonium bromide (DTAB), ferric chloride ($FeCl_3$) (97%), pyrrole (98%), $NaBH_4$ (≥98%) and (3-aminopropyl)triethoxy silane (APTS) were purchased from Sigma Aldrich Co. (St. Louis, MO, USA) and used without purification. The pyrrole-3-carboxylic acid hydrate (95%) and the 4-(4,6-Dimethoxy-1,3,5-triazin-2-yl)-4-methyl morpholinium chloride (DMT-MM) were purchased from Acros Organics (Acros Organics, NJ, USA) and Fluka (Buchs, Switzerland), respectively. Ruthenium (Ⅲ) chloride hydrate (99.98%) was acquired from Aldrich Chemical Company. Potassium hydroxide (NaOH, 95%) and hydrochloric acid (HCl, 35~37%) were purchased from Samchun pure chemical company. 3rd distilled water, maintaining accurate pH 7, was used as the solvent of polypyrrole.

2.3.2. Fabrication of Ru/CPPyNPs introduced UHF-RFID wireless sensor

To attach the Ru/CPPyNPs firmly along the line of the ultrahigh frequency radio frequency identification (UHF-RFID) tag, the part of

RFID tag was treated with APTS. The passive UHF-RFID tags were composed of antenna pattern and microcontroller integrated circuit (IC) chip (EPC global Class-1 Generation-2 (GEN2) protocol) on the plastic substrate ($2 US dollars by the piece). The passive UHF-RFID reader antenna (MT-242025, cost: $1500 U.S. dollars) was purchased from TingMagic Corporation. The frequency range of the reader antenna was 865 – 956 MHz. To prevent pollution of other parts of UHF-RFID tag, the whole RFID tag was wrapped with commercially available plastic tape everywhere apart from at the desired position of the Ru/CPPyNP solution coating. To form the oxygen functional groups, O_2 plasma treatment was used. Then, the tape-wrapped RFID tag was soaked in 5 wt% APTS aqueous solution and the solution was rotated for 6 h at constantly slow rate. After the APTS solution stirring treatment, the RFID tag was removed from the solution and dried at room temperature for 12 h. A glass bath was glued onto the section of the RFID tag that had been treated with APS and diverse Ru/CPPyNP solutions and DMT-MM aqueous solutions were introduced to the glass bath simultaneously. The treated tag was left to dry in standard atmospheric conditions for 24 h to combine Ru/CPPyNPs and RFID tag stably.

2.3.3. Radio frequency measurement of the Ru/CPPyNPs attached UHF-RFID wireless hydrogen sensor

The prepared UHF-RFID tag was placed in the vacuum chamber and exposed to diverse concentrations of hydrogen gas (H_2), ranging from 0.5 to 100 ppm. The concentrations were controlled by the mass flow controller (MFC, KNH Instruments, Pocheon, Korea). The wireless sensor response was transmitted from the RFID tag to the RFID reader antenna, which was connected to the network analyzer. The network analyzer read the frequencies and complex impedances reflected by the wireless sensor tag. To investigate whether the sensor could transmit signals over a range of distances, the distance between the Ru/CPPyNPs-based RFID tag and the reader antenna was varied. The values obtained for the complex impedance were analyzed by KaleidaGraph (Synergy Software, Reading, PA, USA) and the PLS_Toolbox (Eigenvector Research Co. Manson, WA, USA), which were operated using Matlab (The MathWorks, Inc., Natick, MA, USA).

2.3.4. Characterization

A JEOL 6700 instrument was used to obtain FE-SEM images. The topography of atomic force microscopy (AFM) was determined by a Digital Instrument Nanoscope IIIA (Veeco Instruments, Town of Oyster Bay, NY) in tapping mode using silicon tips with the resonant frequency of 320 kHz.

3. Results and Discussion

3.1. Ruthenium/polypyrrole hybrid nanoparticle for hydrogen chemical sensor

3.1.1. Fabrication of Ru/CPPyNP

Figure 15 suggests the schematic diagram of ruthenium (Ru) nanoclusters decoration on the carboxylated polypyrrole nanoparticle (CPPyNP) surface through ultrasonication instrument and following chemical reduction process by steady stirring. As shown in **Figure 16a**, CPPyNPs were prepared by microemulsion method. CPPyNPs are fabricated with same size and they are monodispersed well. For further investigation, single CPPyNP was observed with expanded magnification of TEM like **Figure 16b**. A CPPyNP has a diameter of *ca.* 65 nm and the surface of CPPyNP is smooth without any rimple or crack. The CPPyNPs were stirred in different concentration of $RuCl_3$ aqueous solutions at room temperature to induce charge-charge bonding between the Ru^{3+} ions and the negative charge of the O atom of the carboxylate group in the CPPy structure [105]. The mixed solution was ultrasonicated by tip-sonication instrument to disperse CPPyNPs and $RuCl_3$ uniformly in aqueous solution, break off the

interaction between Ru precursor and O atom of distilled water, and produce a lot of cavitation bubbles with H^+ and OH^- ions, responsible for reduction of metal ions. A small amount of $NaBH_4$ was added to the $RuCl_3$ and CPPyNP mixed solutions with stirring for 3 h at room temperature in order to reduce Ru^{3+} ions to Ru nanoparticles. **Figure 17** represents the multidimensional carboxylated polypyrrole nanoparticles (Ru/CPPyNPs) decorated with uniformly dispersed Ru nanoparticles on the surface.

Furthermore, **Figure 17a**, **b**, and **c** demonstrate the size and density of the decorated Ru nanoparticles, controlled by the gravimetric ratio between the powder of CPPyNPs and $RuCl_3$. The nanostructures of the hybrid CPPyNPs with 0.5, 1.5, and 3.0 ml of injected 0.05 % $RuCl_3$ aqueous solution to CPPyNP aqueous solution are denoted as Ru/CPPyNP_0.5, Ru/CPPyNP_1.5, and Ru/CPPyNP_3.0, respectively. As shown in **Table 1**, Ru/CPPyNP_0.5, Ru/CPPyNP_1.5, and Ru/CPPyNP_3.0 have Ru nanoparticle radii with *ca.* 2, 3.5, and 6 nm, respectively. In **Figure 17d**, the HR-TEM image of Ru nanoparticles indicates an interplanar spacing 0.20 nm for the (101) of hexagonal close-packed (hcp) Ru and confirms growth of pure crystalline nanoparticles following treatment. **Figure 18** shows TEM images of

the hybrid CPPyNPs with increasing Ru precursor concentration over 3.0 ml. Over the 3.0 ml of $RuCl_3$ aqueous solution, Ru nanoparticles form large scale structure and self-aggregation rather than decorated on the CPPyNP surface.

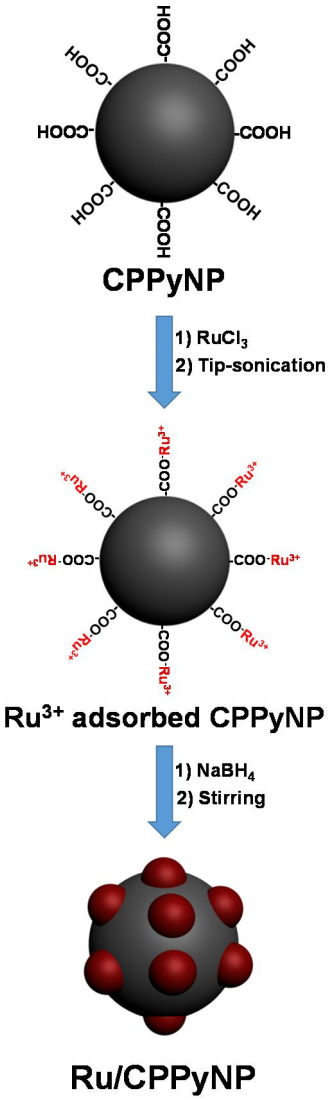

Figure 15. Schematic illustration for fabrication process of Ru/CPPyNP.

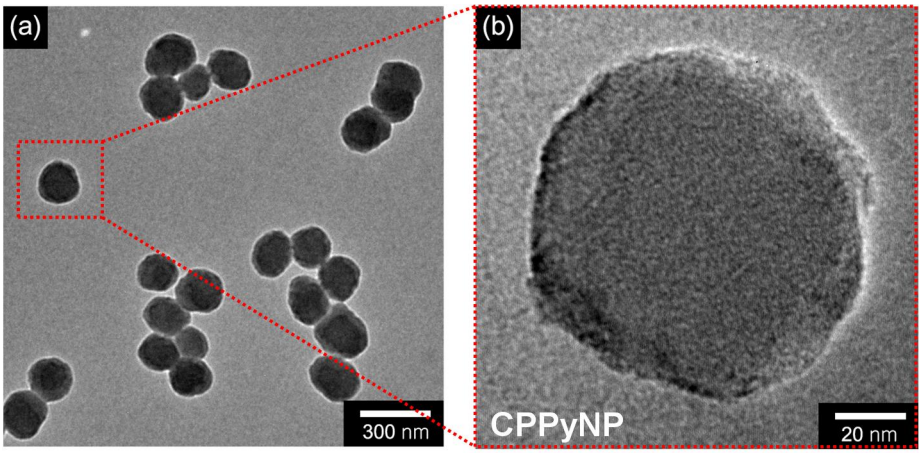

Figure 16. (a) TEM and (b) HR-TEM images of pristine CPPyNP.

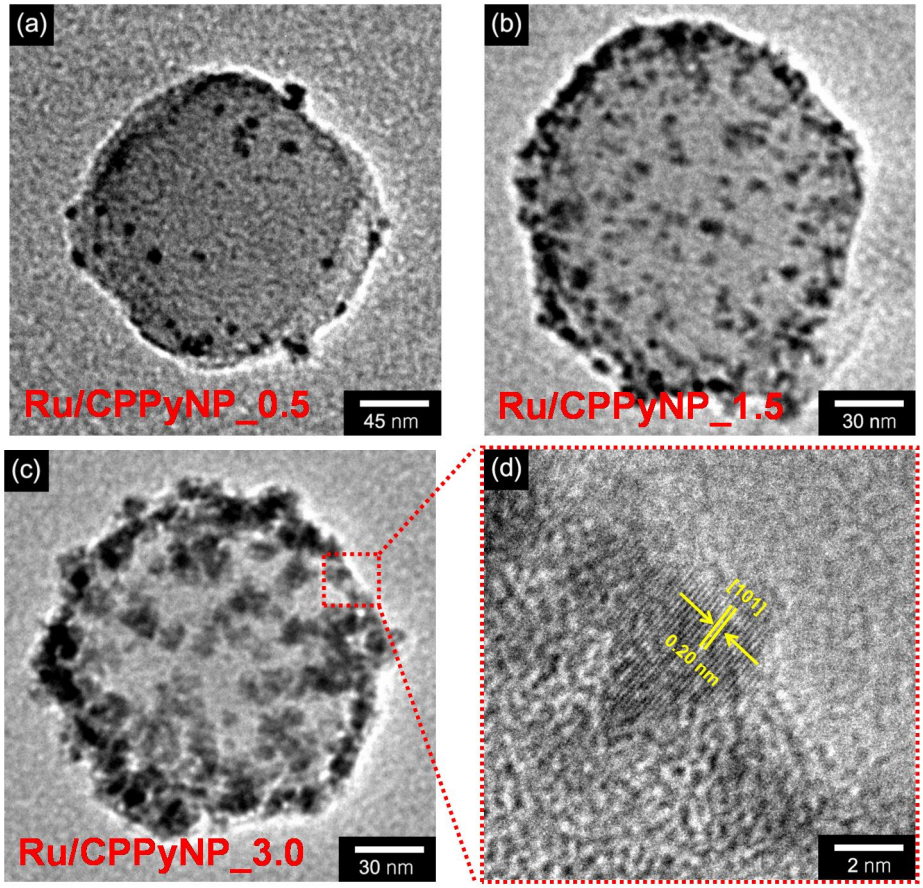

Figure 17. TEM images of Ru/CPPyNPs with different gravimetric ratio of CPPyNP and $RuCl_3$ powders (CPPyNP:$RuCl_3$) - (a) 6:1 (Ru/CPPyNP_0.5), (b) 2:1 (Ru/CPPyNP_1.5), (c) 1:1 (Ru/CPPyNP_3.0) (d) HR-TEM image of Ru nanoparticles on the Ru/CPPyNP_3.0 surface.

Table 1. Average sizes of Ru nanoparticles on the surface of Ru/CPPyNPs with different concentrations of Ru precursor aqueous solution.

Material	Ru nanoparticle size (nm)
Ru/CPPyNP_0.5	*ca.* 2.0
Ru/CPPyNP_1.5	*ca.* 3.5
Ru/CPPyNP_3.0	*ca.* 6.0

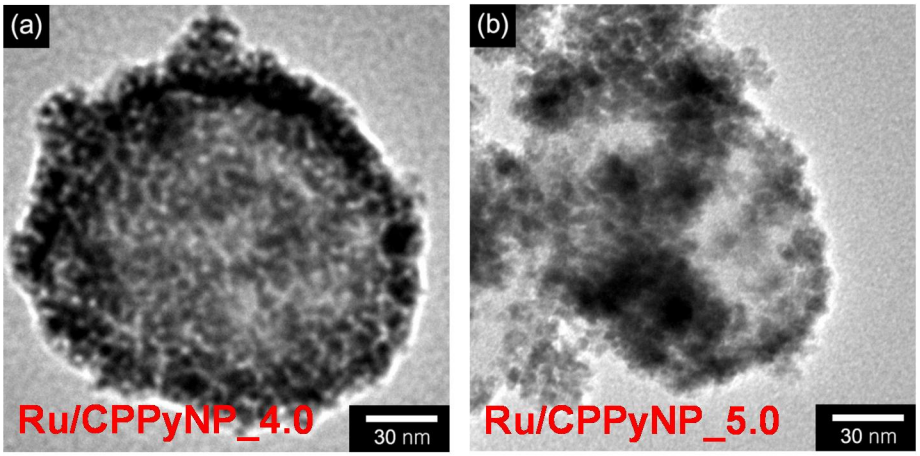

Figure 18. TEM images of Ru/CPPyNPs with different gravimetric ratio of CPPyNP and $RuCl_3$ (CPPyNP:$RuCl_3$) - (a) 1:1.333 (Ru/CPPyNP_4.0) and (b) 1:1.667 (Ru/CPPyNP_5.0).

3.1.2. Material analysis of Ru/CPPyNP

X-ray photoelectron spectroscopy (XPS) characterization was used to analyze the elemental composition of the hybrid nanomaterials. **Figure 19a** displays the wide range spectra of pristine CPPyNP and Ru/CPPyNP over 0 – 1350 eV. The XPS spectrum of pristine CPPyNP reveals only the presence of C, N, and O atoms, while the spectrum of Ru/CPPyNP expresses the presence of C, N, O and Ru atoms. The presence of Ru atoms in the Ru/CPPyNP spectrum indicates that Ru nanoparticles have been deposited onto the surface of the CPPyNP. **Figure 19a** gives evidence of partially reduced CPPyNP. The O 1s peak region of Ru/CPPyNP is slightly less intense than that of CPPyNP, which means a few oxygen-containing functional groups remained on Ru/CPPyNP. The partially reduced aspect of CPPyNP is further revealed in **Figure 19b** and **c**. Furthermore, the C 1s peak region of Ru/CPPyNP shows slightly higher intense that that of CPPyNP because the peak of Ru 3d is merged into the C 1s peak of Ru/CPPyNP. **Figure 19b** illustrates the C 1s peak region of CPPyNP, indicating distinguishable three peaks corresponding to C–C/C=C bonds (*ca.* 284.6 eV), C–N/C–O bonds (*ca.* 286.6 eV), and C=O (*ca.* 288.2 eV). **Figure 19c** shows the C 1s peak region of Ru/CPPyNP.

The peaks at 286.6 eV (C–N/C–O) are less intense when CPPyNP was transformed into Ru/CPPyNP, owing to bond breakage between C and O in the C–OH groups of CPPyNP by the chemical reduction process of $NaBH_4$ (**Figure 19c**). As a result, the peak of C–N/C–C of Ru/CPPyNP transforms from 286.6 eV to 286.0 eV because the peak of C–N appears clearly owing to decrease of C–O peak intense. The peak at 280.6 eV is found for high-resolution C 1s XPS of Ru/CPPyNP. This peak replies to Ru 3d peak because XPS peaks of C 1s and Ru 3d are overlapped at similar binding energy.

Furthermore, high-resolution XPS of Ru 3d, Ru 3p, and X-ray diffraction (XRD) analysis of Ru/CPPyNP were processed for further investigation of Ru presence. The Ru 3d high-resolution spectrum of Ru/CPPyNP is exhibited in **Figure 20a**. Because the spin-orbit split doublet corresponds to zero-valent metallic state Ru $3d_{5/2}$ and Ru $3d_{3/2}$, two peaks with binding energy values of 280.7 eV and 284.8 eV show the valance state of Ru +3. Same phenomenon is viewed in the high-resolution XPS peak of Ru 3p, displayed in **Figure 20b**. Two peaks with binding energy values of 462.5 eV for Ru $3p_{3/2}$ and 484.5 eV for Ru $3p_{1/2}$ show the valance state of Ru +3. **Figure 20c** shows XRD data for CPPyNP and Ru/CPPyNP for comparison. The broad peaks from

20 degree to 30 degree indicate amorphous structure of polypyrrole and both nanomaterials show the peaks for polypyrrole stably. The important diffraction peaks corresponding to (100), (002), (101), and (102) planes of ruthenium nanoparticle crystals (JCPDS card no. 06-0663) are indexed to the HCP phase Ru. It indicates that Ru nanoparticles are well formed on surface of CPPyNPs and the formation of Ru^0 is well performed.

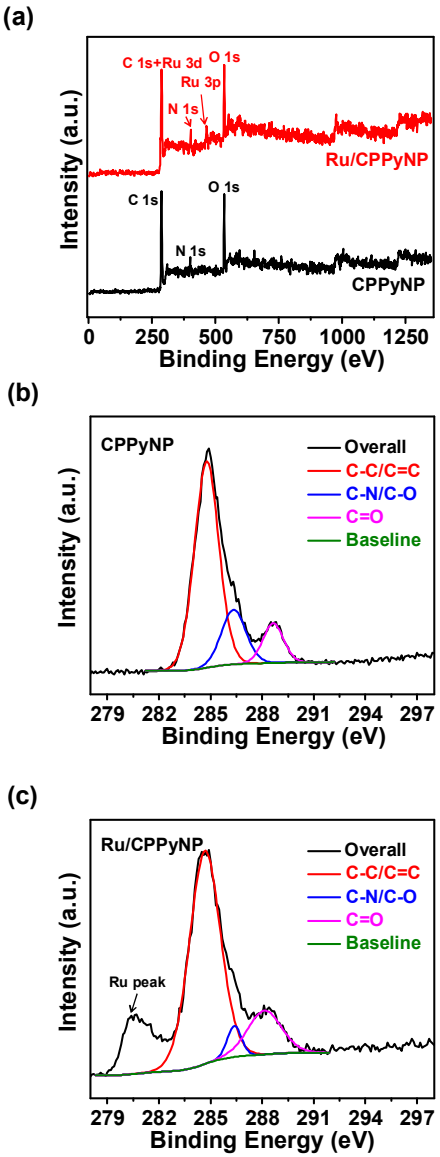

Figure 19. X-ray photoelectron spectroscopy (XPS) spectra of (a) CPPyNP and Ru/CPPyNP. High-resolution C 1s XPS spectra of (b) CPPyNP and (c) Ru/CPPyNP.

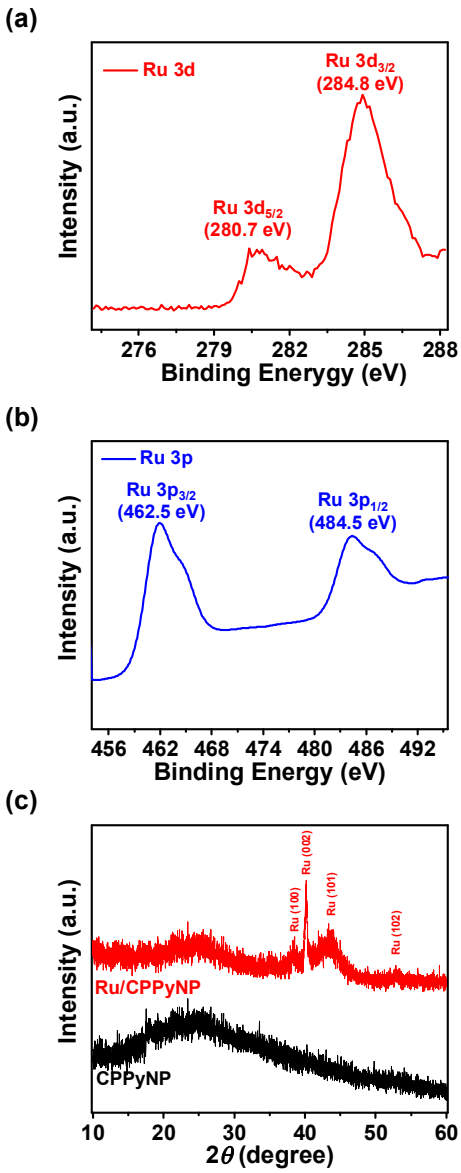

Figure 20. High-resolution XPS spectra of (a) Ru 3d and (b) Ru 3p. (c) X-ray diffraction (XRD) patterns of CPPyNP (black) and Ru/CPPyNP (red).

3.1.3. Characterization of Ru/CPPyNP chemiresistive sensor electrode

To measure the electrical properties of CPPyNP hybrid nanomaterials, Ru/CPPyNPs were immobilized on the interdigitated array (IDA) sensor electrode. The uniformly conductive pathway and effective surface area are the important elements to optimize the performance of sensor electrode and several approaches have been attempted. As a result, spin coating process, one of deposition methods, was chosened to deposit Ru/CPPyNPs uniformly on IDA electrode like **Figure 21b**. Compared to empty electrode, **Figure 21a**, Ru/CPPyNPs fill the electrode densely.

To verify the roles of Ru nanoparticles in determining electrical properties of hybrid nanoparticles, the four-probe instrument was used to measure electrical conductivity of each hybrid nanomaterial. As shown in **Figure 22a**, the electrical conductivities of CPPyNP, Ru/CPPyNP_0.5, Ru/CPPyN_1.5, Ru/CPPyNP_3.0 record 48 S cm^{-1}, 65 S cm^{-1}, 98 S $cm^{-1,}$ 127 S cm^{-1} owing to inborn metal characteristic of ruthenium, respectively. Furthermore, because ruthenium has larger work function than polypyrrole work function, ruthenium nanoclusters on CPPyNP surface flocculate the electrons. Due to *p*-type

semiconducting characteristics of polypyrrole, hole is the charge carrier of polypyrrole. As a result, agglutination of electrons on ruthenium nanoclusters increase hole density in hybrid nanoparticles and the electrical conductivity of hybrid nanoparticle moves up. Similar tendency is watched in current–voltage (*I-V*) curve measurement.

Current–voltage (*I–V*) curves are analyzed to estimate the electrical contact of Ru/CPPyNPs on the IDA gold alloy electrode surface. **Figure 22b** shows the I_{SD}-V_{SD} properties of each Ru/CPPyNP made with different Ru nanoparticle populations. The curves are linear forms for voltage from -0.1 V to 0.1 V and the *dI/dV* value increases with growing numbers of Ru nanoparticles on the CPPyNP surface. According to the results, Ru nanoparticles enhanced the conductivity of the CPPyNPs and Ru/CPPyNPs and attach on IDA gold electrode with good electrical contact, called ohmic contact.

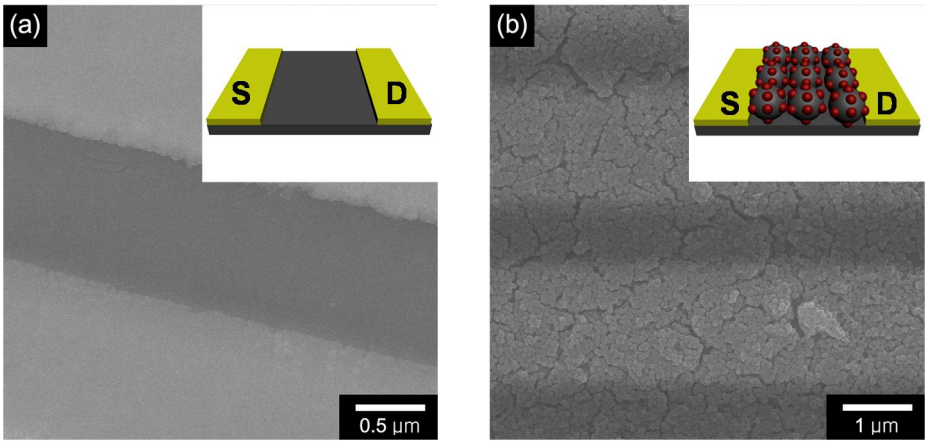

Figure 21. FE-SEM images of (a) interdigitated micro array (IDA) electrode and (b) Ru/CPPyNPs on the IDA substrate.

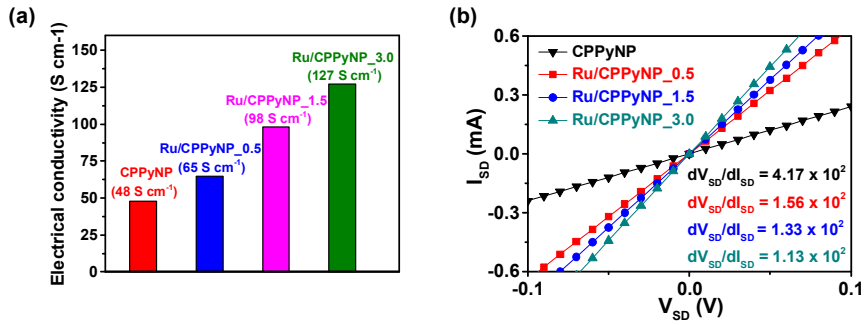

Figure 22. (a) Electrical conductivities (Red: CPPyNP; Blue: Ru/CPPyNP_0.5; Magenta: Ru/CPPyNP_1.5; Green: Ru/CPPyNP_3.0) and (b) I-V curves (Black: CPPyNP; Red: Ru/CPPyNP_0.5; Blue: Ru/CPPyNP_1.5; Blue-green: Ru/CPPyNP_3.0) of different CPPyNP based nanomaterials.

3.1.4. Electrical measurement of Ru/CPPyNP based hydrogen gas chemical sensor

To measure the sensing characteristics of the Ru/CPPyNPs based sensor electrode, the real-time responsive resistance changes were measured for different concentrations of hydrogen gas and are illustrated in **Figure 23a**. Ru/CPPyNPs with three different conditions (Ru/CPPyNP_0.5, Ru/CPPyNP_1.5, and Ru/CPPyNP_3.0) were spread on electrode as transducer to detect hydrogen. Upon each exposure of hydrogen gas, the Ru/CPPyNP based electrodes exhibit an increase in resistance over a several second period to reach a saturated value. When hydrogen flow to Ru/CPPyNP based electrode stops, the resistance of electrode returns to primary resistance before exposure to hydrogen gas with several second period. These effects are obtained by the catalytic chemical reaction between ruthenium and hydrogen gas (**Figure 24**). Detailed process is described below. Initially, the hydrogen molecules adsorb to the ruthenium nanoparticle surface. The two H atoms react with the ruthenium nanoparticles which are components of the coating layer to form the complex hybrid, RuH_x. The resistance of the composite particle based electrode increases with the phase transition of the ruthenium layer from Ru to RuH_x [106].

Then, RuH_x is transformed to the original ruthenium structure (Ru) by exposure to oxygen containing gas to cause H_2O formation between the hydrogen atoms and oxygen gas [107-108]. To confirm this mechanism, high resolution-transmission electron microscopy (HR-TEM) was used to observe the states of ruthenium nanoparticles on the surface of CPPyNP, before hydrogen sensing and after hydrogen sensing (**Figure 25**). As a result, the HR-TEM images of Ru nanoparticle indicate that pure crystalline nanoparticles maintain their original state after hydrogen sensing. Thus, the ruthenium coating layer plays a key role in the hydrogen detection mechanism as follows. The ruthenium nanoparticles bond to the hydrogen gas molecules via a chemisorption interaction. In other words, enhancing the population of ruthenium nanoparticles on the surface of CPPyNPs induces an increase in the number of active sites available to the hydrogen gas. Therefore, composites with thicker ruthenium layer coating exhibit high sensitivity to hydrogen gas. The minimum detectable levels (MDLs) of the composites are as follows - Ru/CPPyNP_0.5: 25 ppm; Ru/CPPyNP_1.5: 5 ppm; Ru/CPPyNP_3.0: 0.5 ppm. Therefore, a better sensitive response is achieved with a large amount of ruthenium active sites, as a result of the enhanced catalytic activity towards the

hydrogen gas. Also, resistance change increases with increment of hydrogen gas concentration, exposed to Ru/CPPyNP surface, because more ruthenium nanoparticles transit simultaneously from Ru to RuH_x with higher hydrogen gas concentration.

Figure 23b shows the changes in sensitivity as a function of ruthenium density for the composite nanoparticles, with respect hydrogen concentration. The sensitivity (S) is determined from the saturation point of the normalized resistance change, measured 20 s after the resistance change at the highest point of normalized resistance change. As show in graph, the Ru/CPPyNP_3.0 based sensor displays nonlinear changes in sensitivity at low concentration of hydrogen gas. Linear behavior is observed over a wide range of concentrations (5 – 100 ppm). Therefore, the Ru/CPPyNP_3.0 based sensor electrodes demonstrate reversible and reproducible responses to different analyte concentrations, and their responses are more pronounced as the gas concentration increases. Other Ru/CPPyNP based sensors with different Ru density on CPPyNP surface show similar characteristic when they expose to various concentration of hydrogen gas. However, linear behaviors of these sensors are observed with narrower range of hydrogen concentration than Ru/CPPyNP_3.0

based sensor because they have less Ru nanoparticles on CPPyNP surface than Ru/CPPyNP_3.0. As a result, Ru/CPPyNP_3.0 based sensor shows the best performance among others.

Excellent cycle stability is required for electrode materials in the practical implementation of sensor devices. **Figure 23c** presents the electrical response of various composite nanoparticles upon periodic exposure to 25 ppm of hydrogen gas at room temperature. These particles reveals a similar response for the sensitivity each time and the sensor was used without retardation of the response or recovery times. Moreover, composite CPPyNP based sensors maintained their sensing ability toward exposure to 25 ppm of hydrogen gas during 15 days (**Figure 23d**). This is because the structure of the CPPyNP layer prevents morphology collapse from the phase transition of ruthenium (Ru) to ruthenium halide (RuH_x) during hydrogen detection. Therefore, the Ru/CPPyNP based sensor electrodes exhibit high stability for repetitive hydrogen gas detection.

Intimate research for response and recovery time of sensor was progressed for further investigation of sensor performance. The response times of Ru/CPPyNPs with different Ru densities on CPPyNP surface are demonstrated in **Figure 26a**. The response time

of Ru/CPPyNP becomes shorter when the Ru concentration of Ru/CPPyNP increases. The enhanced surface area of the Ru/CPPyNP by Ru nanoparticles allows rapid diffusion times, as well as enhanced sensitivity with the increase in the thickness of the ruthenium layers (Ru/CPPyNP_0.5 < Ru/CPPyNP_1.5 < Ru/CPPyNP_3.0), because thicker ruthenium layers provide higher surface to volume ratio and increase the interaction with the target analyte. In result, the response times of nanocomposite based sensor are 46 s, 37 s, and 31 s for Ru/CPPyNP_0.5, Ru/CPPyNP_1.5, and Ru/CPPyNP_3.0, respectively. On the other hand, opposite results are occurred in recovery time investigation (**Figure 26b**). The recovery time increases with the increment of Ru nanoparticles ratio on CPPyNPs surface because the increased amount of phase transferred materials, ruthenium halide (RuH_x), has to return to ruthenium (Ru) during recovery time. Thus, the recovery times of CPPyNP composite based sensors are 47 s, 53 s, and 58 s for Ru/CPPyNP_0.5, Ru/CPPyNP_1.5, and Ru/CPPyNP_3.0, respectively. Ru/CPPyNP based sensor shows developed performance compared to other hydrogen sensor (**Table 2**). There is only few ruthenium based hydrogen senor. Therefore, palladium based hydrogen sensors, the most famous and high-performed hydrogen

sensor, are cited to compare performance with Ru/CPPyNP based sensor.

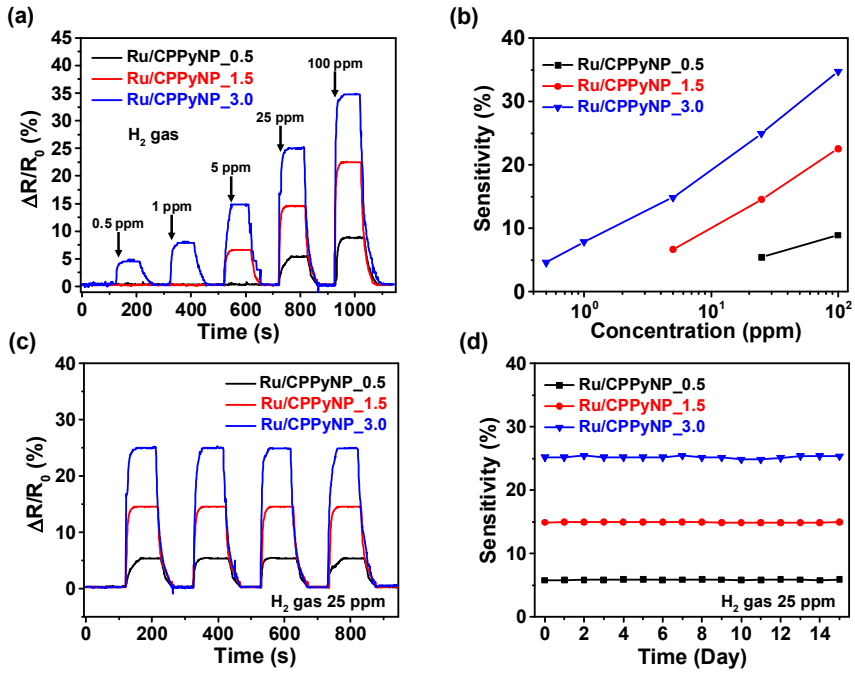

Figure 23. (a) Normalized resistance change upon sequential exposure to various concentrations of hydrogen gas (black: Ru/CPPyNP_0.5; red: Ru/CPPyNP_1.5; blue: Ru/CPPyNP_3.0). (b) Calibration lines as function of hydrogen gas concentrations (black: Ru/CPPyNP_0.5; red: Ru/CPPyNP_1.5; blue: Ru/CPPyNP_3.0). (c) Normalized resistance changes of different hybrid CPPyNPs upon sequential periodic exposure to 25 ppm of hydrogen gas. (d) Sensitivity changes of hybrid CPPyNPs with periodic exposure to 25 ppm of hydrogen gas for 15 days (black: Ru/CPPyNP_0.5; red: Ru/CPPyN_1.5; blue: Ru/CPPyNP_3.0).

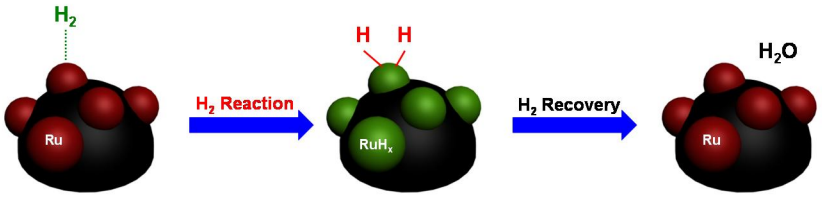

Figure 24. Hydrogen gas detection mechanism of Ru/CPPyNPs at room temperature.

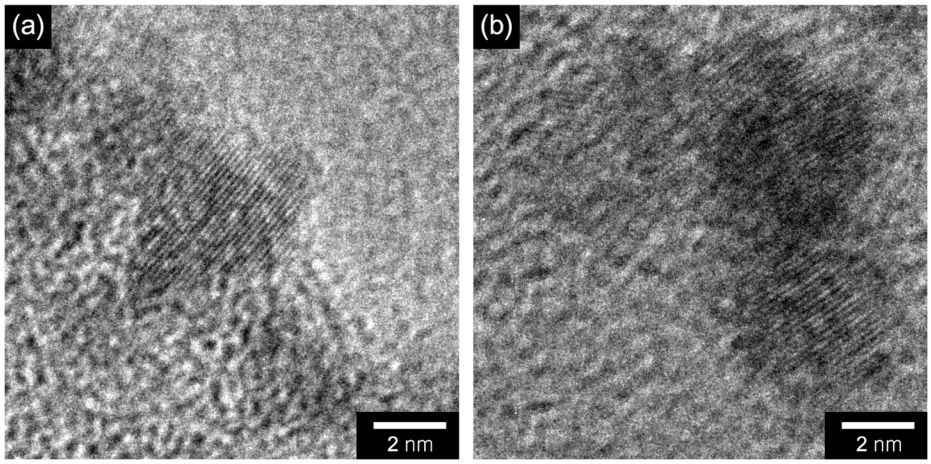

Figure 25. HR-TEM images of Ru nanoparticles on the CPPyNP surface (a) before hydrogen sensing and (b) after hydrogen sensing.

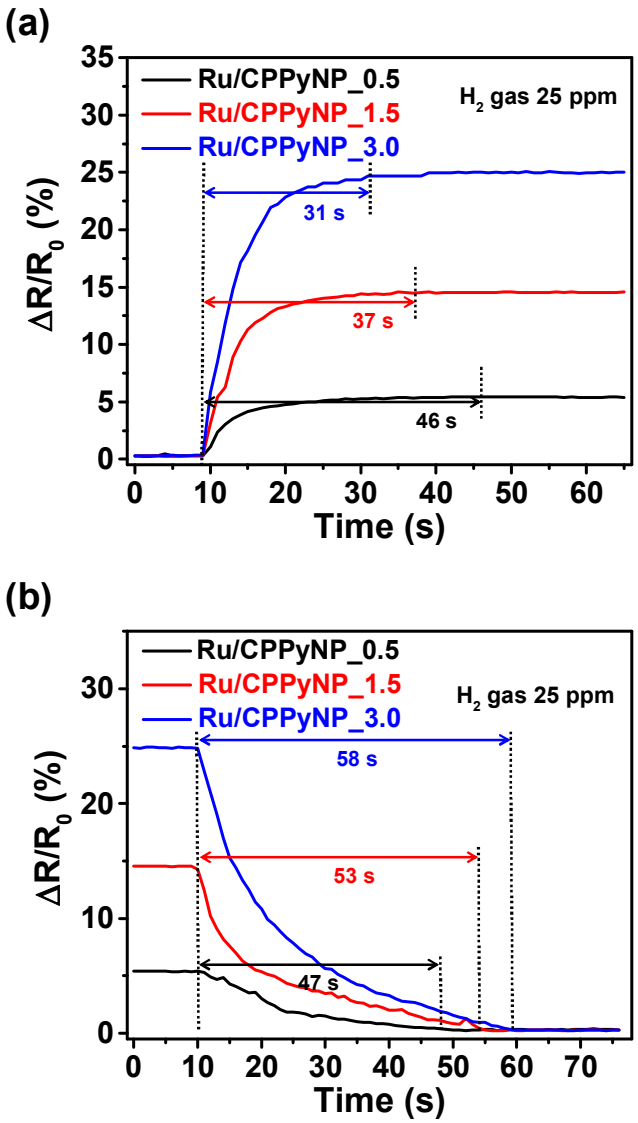

Figure 26. (a) Response and (b) recovery times of Ru/CPPyNPs with different Ru densities toward 25 ppm of hydrogen gas (black: Ru/CPPyNP_0.5; red: Ru/CPPyNP_1.5; blue: Ru/CPPyNP_3.0).

Table 2. Hydrogen gas sensing ability of different nanomaterials based sensing electrodes.

Configuration	Working temperature	MDL[a]	Response time	Recovery time	Reference
Pd NP[b]s on graphene	25℃	20 ppm	≥15 min	≥30 min	[81]
Pd NPs on graphene nanoribbons	25℃	30 ppm	≥60 s	≥300 s	[109]
Pd NC[c]s on graphene	25℃	6 ppm	20 min	54 min	[110]
Pd-NiO particle	150℃	30 ppm	131 s	151 s	[111]
Ru/CPPyNP_3.0	25℃	0.5 ppm	31 s	58 s	This work

[a] Minimum detectable level

[b] nanoparticle

[c] nanocube

To confirm the effect of metal and conducting polymer hybrid nanomaterial for hydrogen sensor, hydrogen detection measurements with only CPPyNP and Ru nanoparticles are progressed and the results are featured in **Figure 27**.

In **Figure 27a**, normalized resistance change of CPPyNPs based sensor is introduced with sequential exposure to increased concentration of hydrogen from 5 ppm to 250 ppm. There is no signal change of CPPyNP based sensor despite of long time exposure to high grade hydrogen. As a result, the researcher conflicts that there is no chemical reaction among hydrogen gas and CPPyNPs.

In sequence, chemiresistive hydrogen sensing performance was processed with Ru nanoparticles based sensor and the result is displayed in **Figure 27b**. As shown in figure, Ru nanoparticles react to only 250 ppm of hydrogen, extremely high concentration of hydrogen gas, and the resistance change is extremely low (1.5 %≥). From these results, the researcher can postulate that conducting polymer nanostructures enhance charge carrier concentration and mobility upon analyte gas exposure owing to *p*-type semiconducting behavior of conducting polymer under ambient conditions. Furthermore, Ru/CPPyNP composite generally forms a porous structure with

increased surface area which eases gas diffusion and it offers better sensing response. In other words, Ru nanoparticles on CPPyNP layer increase the overall active sensing surface area, which increases the number of gas adsorption sites.

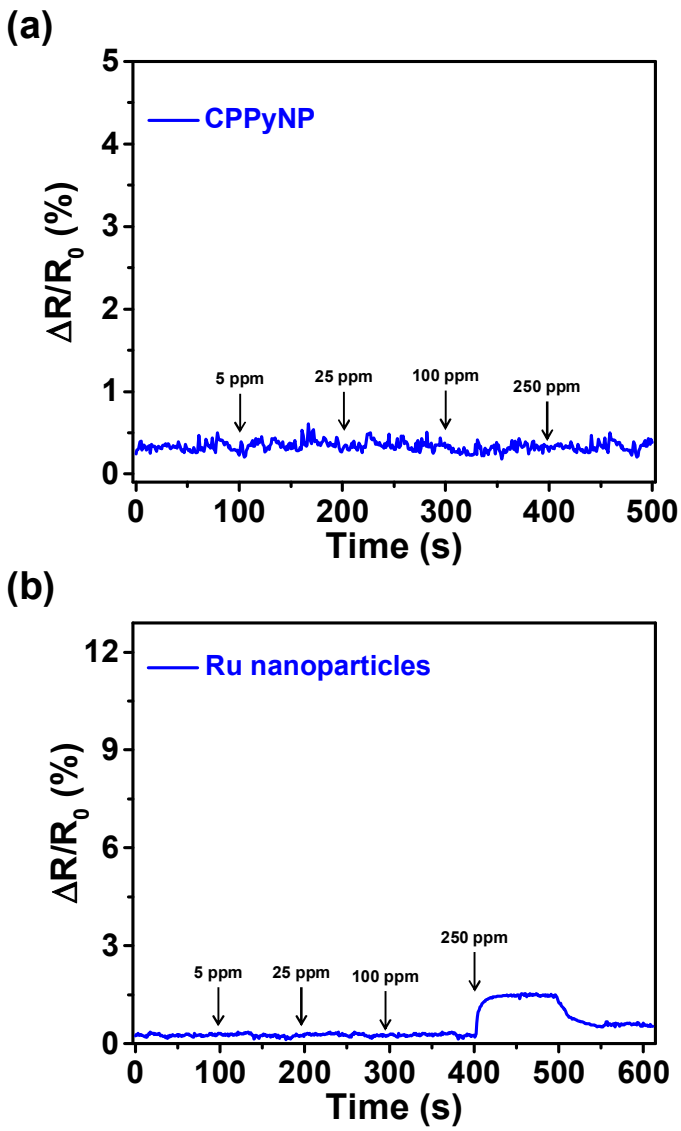

Figure 27. Normalized resistance changes upon sequential exposure to various concentrations of hydrogen gas to (a) pristine CPPyNPs and (b) ruthenium nanoparticles.

3.2. Acid-base treatment of Ru/CPPyNPs to control the chemiresistive properties of hydrogen chemical sensor

3.2.1. Morphology change observation of Ru/CPPyNPs by acid-base treatment

The charge carrier density and mobility of conducting polymer are reversibly changed by chemical treatment of acid and base solutions. **Figure 28** illustrates the procedure to change state of hybrid polypyrrole nanomaterial. In this experiment, Ru/CPPyNP, fabricated with 1:1 gravimetric ratio of CPPyNP and ruthenium precursor, was used. Ru/CPPyNP was inserted to solvent and sonicated for 12 h to disperse nanoparticles uniformly in the solvent. Five types of solvent are used for chemical treatment of Ru/CPPyNP, pH 1, 4, 7, 10 and 13. Hydrochloric acid (HCl) aqueous solution was used to make pH 1 and 4 solvent. Potential of hydrogen (pH) is concluded by hydrogen ion (H^+) concentration and following equation decides pH of solvent.

$$\mathrm{pH} = -\log[H^+]$$

According to the equation, 10^{-1} M HCl aqueous solution was used as solvent for Ru/CPPyNP to treat nanocomposites with pH 1 (pH 1_Ru/CPPyNP) and 10^{-4} M HCl aqueous solution was used to treat Ru/CPPyNPs with pH 4 (pH 4_Ru/CPPyNP). On the other hand,

potassium hydroxide (NaOH) aqueous solution, which is base solution, was used to transfer pH state of Ru/CPPyNPs to pH 10 and 13. The pH of base solution is decided by following equations.

$$\text{Potential of hydroxide (pOH)} = -\log[OH^-]$$

$$\text{pH} + \text{pOH} = 14$$

$$\text{pH} = 14 - \text{pOH} = 14 + \log[OH^-]$$

As a result, 10^{-1} M NaOH aqueous solution was used as solvent for Ru/CPPyNP to treat nanocomposites with pH 13 (pH 13_Ru/CPPyNP) and 10^{-4} M NaOH aqueous solution was used to treat Ru/CPPyNPs with pH 10 (pH 10_Ru/CPPyNP). 3rd distilled water was used as solvent for dissolving Ru/CPPyNPs to treat them with pH 7 (pH 7_Ru/CPPyNP).

Then, Ru/CPPyNP powders uniformly dispersed solutions with five types of acid and base solvents were stirred steadily with low rate for another 12 h to react Ru/CPPyNPs and solvents entirely. At last, the solutions were centrifuged and remained solid body, chemically treated Ru/CPPyNPs, dried at 60℃ oven for overnight.

To confirm morphology transitions of acid and base treated Ru/CPPyNPs, transmission electron microscopy (TEM) measurement was introduced to each nanomaterial (**Figure 29**). Because electrical

state of conducting polymer changes reversibly with different pH solvents, Ru/CPPyNPs were soluted in the same solvents that were used for acid and base treatment. The morphology of pH 7_Ru/CPPyNP is used as criteria for comparison because the fabrication process of Ru/CPPyNP was progressed in 3rd distilled water. pH 7_Ru/CPPyNP shows *ca.* 65 nm diameter of CPPyNP and Ru nanoparticles are uniformly dispersed on the surface of CPPyNP. The size of Ru nanoparticles is *ca.* 6 nm in average. Other Ru/CPPyNPs with diverse pHs display subequal morphologies with pH 7_Ru/CPPyNP. For further investigation, high resolution-transmission electron microscopy (HR-TEM) was used to observe transition of Ru nanoparticles with pH change (**Figure 30**). Each image shows lattice structure of ruthenium. In **Figure 30b - e**, the HR-TEM images of Ru nanoparticles indicate interplanar spacing of 0.20 nm for the (101) and spacing of 0.23 nm for the (100) of hexagonal close-packed (hcp) ruthenium and confirms growth of pure crystalline nanoparticles following treatment. Although **Figure 30a**, pH 1_Ru/CPPyNP, displays only the interplanar spacing of 0.23 nm for the (100), it can be indicated that pure crystalline of hexagonal close-packed (hcp) ruthenium nanoparticles are maintained its characteristic

during pH 1 acid treatment. From these results, it is confirmed that acid and base treatments of Ru/CPPyNPs make no difference of nanocomposite morphologies.

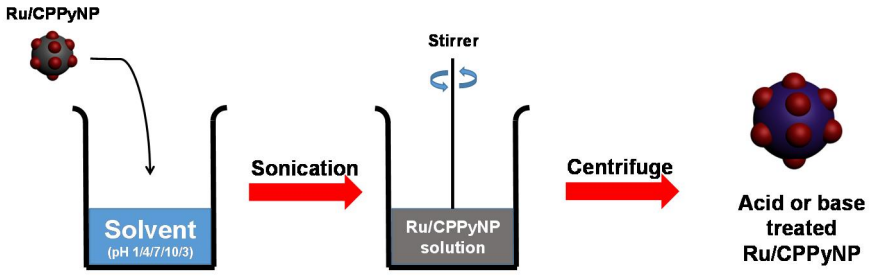

Figure 28. Schematic diagram for acid or base treatment steps of Ru/CPPyNPs.

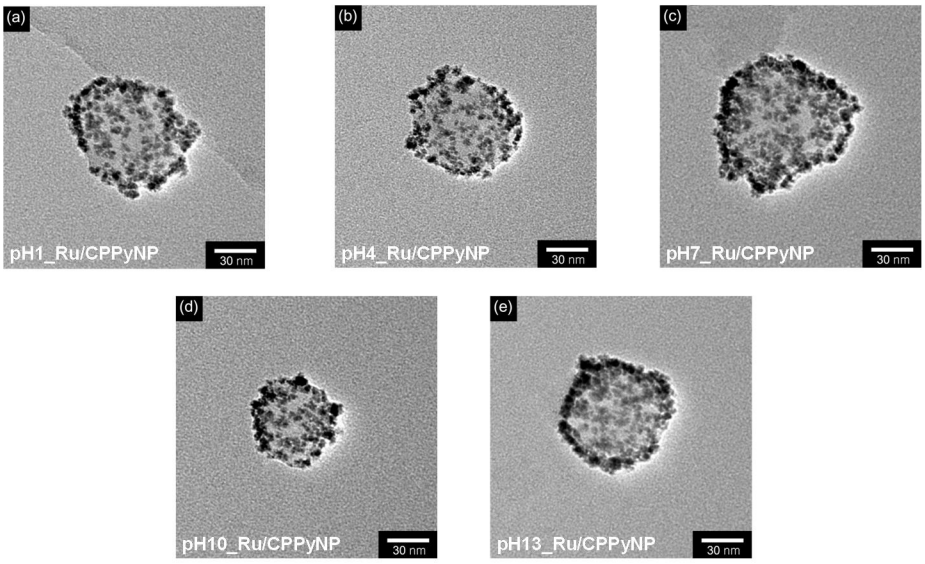

Figure 29. TEM images of Ru/CPPyNPs with different pH solvents - (a) 10^{-1} M HCl aqueous solution treated Ru/CPPyNP (pH 1_Ru/CPPyNP), (b) 10^{-4} M HCl aqueous solution treated Ru/CPPyNP (pH 4_Ru/CPPyNP), (c) 3rd distilled water treated Ru/CPPyNP (pH 7_Ru/CPPyNP), (d) 10^{-4} M NaOH aqueous solution treated Ru/CPPyNP (pH 10_Ru/CPPyNP), and (e) 10^{-1} M NaOH aqueous solution treated Ru/CPPyNP (pH 13_Ru/CPPyNP).

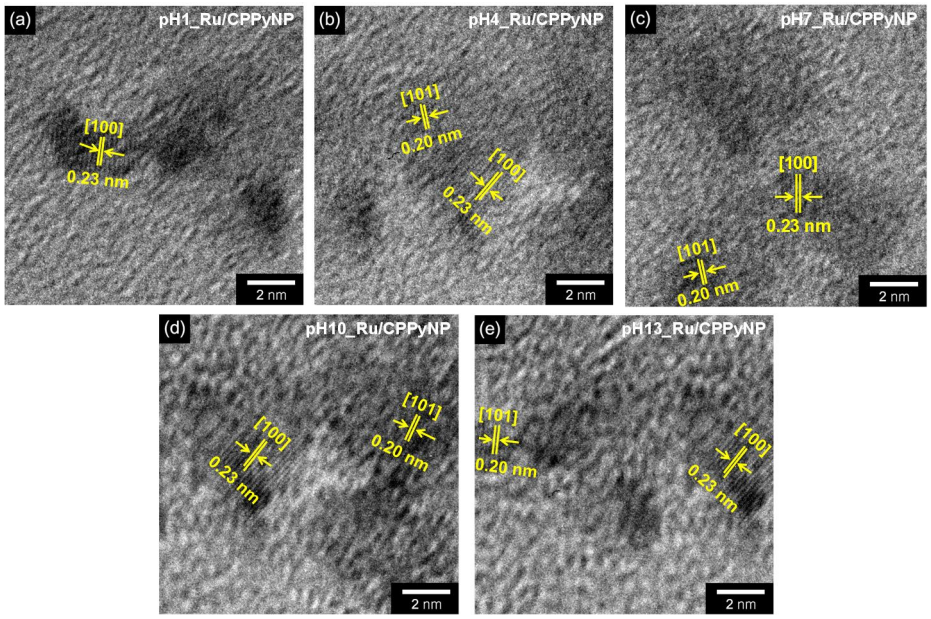

Figure 30. HR-TEM images of Ru nanoparticles on the acid or base treated Ru/CPPyNP surface - (a) 10^{-1} M HCl aqueous solution treated Ru/CPPyNP (pH 1_Ru/CPPyNP), (b) 10^{-4} M HCl aqueous solution treated Ru/CPPyNP (pH 4_Ru/CPPyNP), (c) 3rd distilled water treated Ru/CPPyNP (pH 7_Ru/CPPyNP), (d) 10^{-4} M NaOH aqueous solution treated Ru/CPPyNP (pH 10_Ru/CPPyNP), and (e) 10^{-1} M NaOH aqueous solution treated Ru/CPPyNP (pH 13_Ru/CPPyNP).

3.2.2. Material analysis of acid and base treated Ru/CPPyNPs

Variable material measurement methods were used to analyze the structural differences among Ru/CPPyNPs, treated by solvents with five different pHs. First of all, **Figure 31a** shows the Raman spectra results of Ru/CPPyNPs. Ru/CPPyNPs display characteristic peaks at 1555 cm^{-1} in common, corresponding to their C=C stretching vibrations. However, the peak height of each Ru/CPPyNP is different. When the pH of Ru/CPPyNP solvent decreases, the Raman spectrum peak at 1555 cm^{-1} increases. The increment of peak height at 1555 cm^{-1} means that the number of C=C stretchings in polypyrrole chain structure increases. Polypyrrole (PPy) chains in **Figure 33** explain the Raman spectra results. HCl treated Ru/CPPyNPs have PPy chains in CPPyNPs structure like **Figure 33a** and NaOH treated Ru/CPPyNPs have PPy chains like **Figure 33c** in CPPyNPs backbone. As shown in figures, more C=C strechings are obtained in acid treated PPy chain than base treated PPy chain. As a result, the Raman spectrum of pH 1 treated Ru/CPPyNPs shows higher intensity of 1555 cm^{-1} peak than that of pH 13 treated Ru/CPPyNPs.

For further investigation of PPy chain structure, Fourier-transform infrared spectroscopy (FT-IR) measurement was processed for

Ru/CPPyNPs (**Figure 31b**). There are three main peaks of Ru/CPPyNPs to compare the intensity change due to pH differences of Ru/CPPyNPs treated solvents, 914, 1040, and 1558 cm^{-1} of wavenumber. The absorption bands at 914, 1040, and 1558 cm^{-1} are assigned to the N–H, C–H in plane vibrations, and C=C ring stretching of PPy, respectively [112-114]. These new characteristic absorption bands confirm the formation of PPy layer in Ru/CPPyNP structure. Moreover, the peaks at 1558 cm^{-1} of C=C stretching ring in PPy structure have as shift that the structure of C=C bond of polypyrrole rings changed during the treatment with hydrochloric acid. The peak intensity of each absorption band increases with increment of hydrogen ion concentration in solvents. These results are also explained by polypyrrole structures described in **Figure 33**. The peak intensity of N–H bonding in plane vibrations increases with decrease of pH value due to structural transformation by acid and base treatment. Other peak intensities at 1040 and 1558 cm^{-1} also show similar tendencies with decrease of pH value.

To confirm the modification of ruthenium nanoparticles on CPPyNP surface by pH value of solvents, X-ray diffraction (XRD) analysis was used to Ru/CPPyNPs with diverse pH solvents (**Figure 31c**). As a

result, all measured results show same peak intensity to XRD characterization of Ru/CPPyNPs. The important diffraction peaks corresponding to (100), (002), (101), and (102) planes of ruthenium nanoparticle crystals (JCPDS card no. 06-0663) are indexed to the HCP phase of Ru. It indicates that Ru nanoparticles were well formed on surface of CPPyNPs and the formation of Ru^0 was well performed. Also, the results in **Figure 31c** show that the treatment of acid and base to Ru/CPPyNPs doesn't affect the phase of Ru nanoparticles. Because nano-sized materials have different and high physical properties to bulk materials with same elements, nano-sized Ru particles are not modified by chemical reduction and oxidization.

Figure 32 and **Figure 34** describe X-ray photoelectron spectroscopy (XPS) results for detailed investigation of Ru/CPPyNPs. First, **Figure 32** shows the results of high resolution N 1s peaks for Ru/CPPyNPs with different pHs. The structural changes of CPPyNPs are analyzed by these results. **Figure 32c** becomes as the datum point for structural changes by pH because it is XPS data for pH 7 solvent treated Ru/CPPyNPs. There are two noticeable nitrogen peaks. The predominant peak at 400.3 eV is correlated with pyrrolic nitrogen (–NH–) in the pyrrole ring [115-116]. The lower binding energy

component, evidenced by a shoulder peak at 398.0 eV, corresponds to the imine nitrogen (–N=). Based on these data, protonation levels at the nitrogen sites in Ru/CPPyNPs can be calculated in terms of (–N=/N_{total}) [117]. The (–N=/N_{total}) ratio indicates the doping level because the ratio of –N= structures in polypyrrole rings decreases by positive charges in the pyrrole rings. Therefore, lower (–N=/N_{total}) ratios correspond to higher doping levels. **Figure 32d** and **e**, pH 10 and 13 solvents treated Ru/CPPyNPs, display enlarged area of –N= peak compared to that of pH 7 solvent treated Ru/CPPyNPs. These results are observed because N^+ ratio in pyrrole ring structure decreases. On the other hand, HCl treated Ru/CPPyNPs, pH 1 and 4 solvents treated Ru/CPPyNPs, demonstrate decreased area of –N= peak in **Figure 32a** and **b**. pH 4 solvent treated Ru/CPPyNPs show similar area amount to pH 7 solvent treated Ru/CPPyNPs. However, because N_{total} area of **Figure 32b** is larger than that of **Figure 32c**, the ratio of (–N=/N_{total}) for pH 4_Ru/CPPyNP is smaller than that of pH 7_Ru/CPPyNPs. As a result, Ru/CPPyNPs, treated with diverse pHs, show constant tendency of structural change due to protonation levels of polypyrrole rings.

Figure 34 analyzes the high resolution Ru 3d and Ru 3p peaks of XPS method. The Ru 3d high-resolution spectra of Ru/CPPyNPs with various pH solvents are exhibited in **Figure 34a**. Because the spin-orbit split doublet corresponds to zero-valent metallic state Ru $3d_{5/2}$ and Ru $3d_{3/2}$, two peaks with binding energy values of 280.7 eV and 284.8 eV show the valance state of Ru +3. There is no difference among Ru 3d XPS peaks for different types of Ru/CPPyNPs. Same phenomenon is viewed in the high-resolution XPS peak of Ru 3p, displayed in **Figure 34b**. Two peaks with binding energy values of 462.5 eV for Ru $3p_{3/2}$ and 484.5 eV for Ru $3p_{1/2}$ show the valance state of Ru +3. From these results, the researcher postulates that there is no structural change of Ru nanoparticles by acid and base solvents treatment.

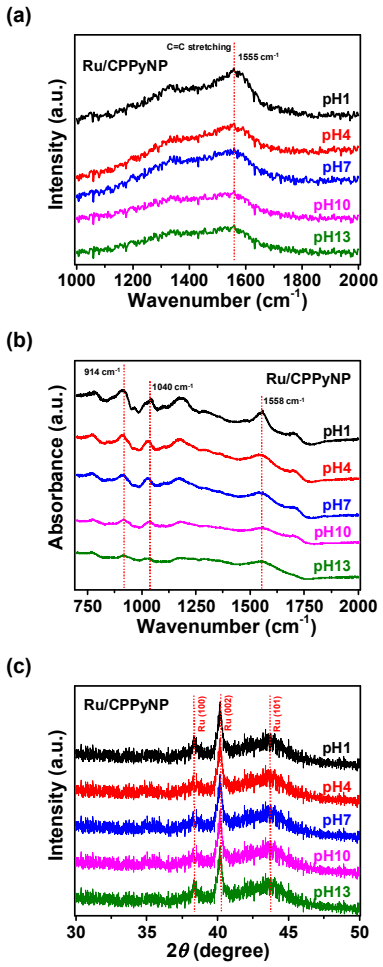

Figure 31. (a) Raman spectra, (b) Fourier-transform infrared spectroscopy (FT-IR), and (c) X-ray diffraction (XRD) of acid or base treated Ru/CPPyNPs (black: pH 1_Ru/CPPyNP; red: pH 4_Ru/CPPyNP; blue: pH 7_Ru/CPPyNP; magenta: pH 10_Ru/CPPyNP; green: pH 13_Ru/CPPyNP).

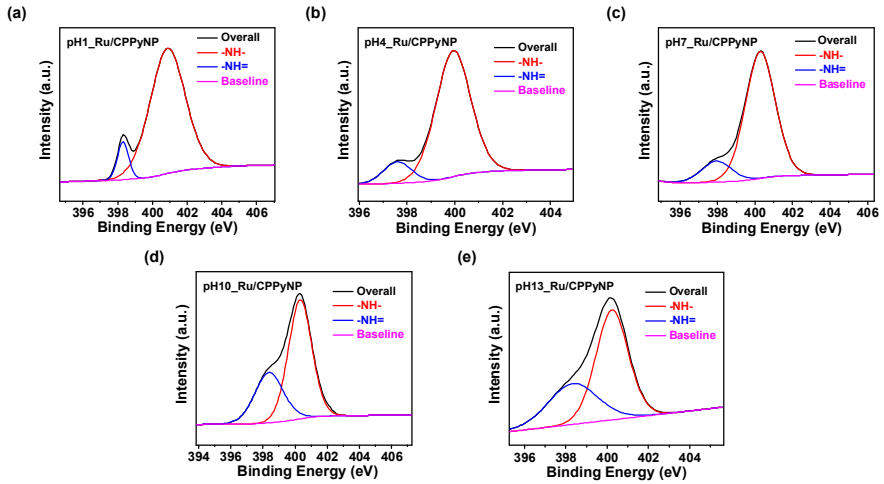

Figure 32. N 1s high resolution X-ray photoelectron spectroscopy (XPS) analysis of (a) pH 1_Ru/CPPyNP, (b) pH 4_Ru/CPPyNP, (c) pH 7_Ru/CPPyNP, (d) pH 10_Ru/CPPyNP, and (e) pH 13_Ru/CPPyNP.

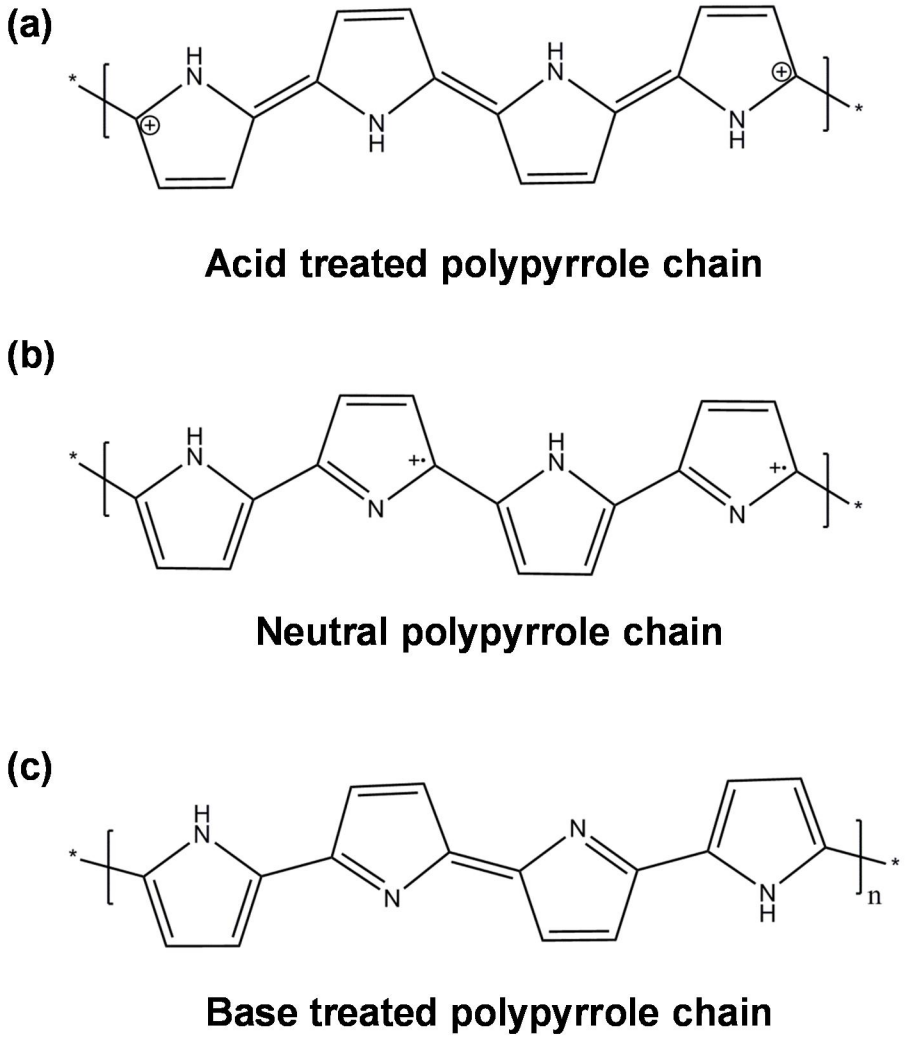

Figure 33. Chemical backbone structures of polypyrrole (PPy) illustrating (a) acid treated, (b) 3rd distilled water treated, and (c) base treated.

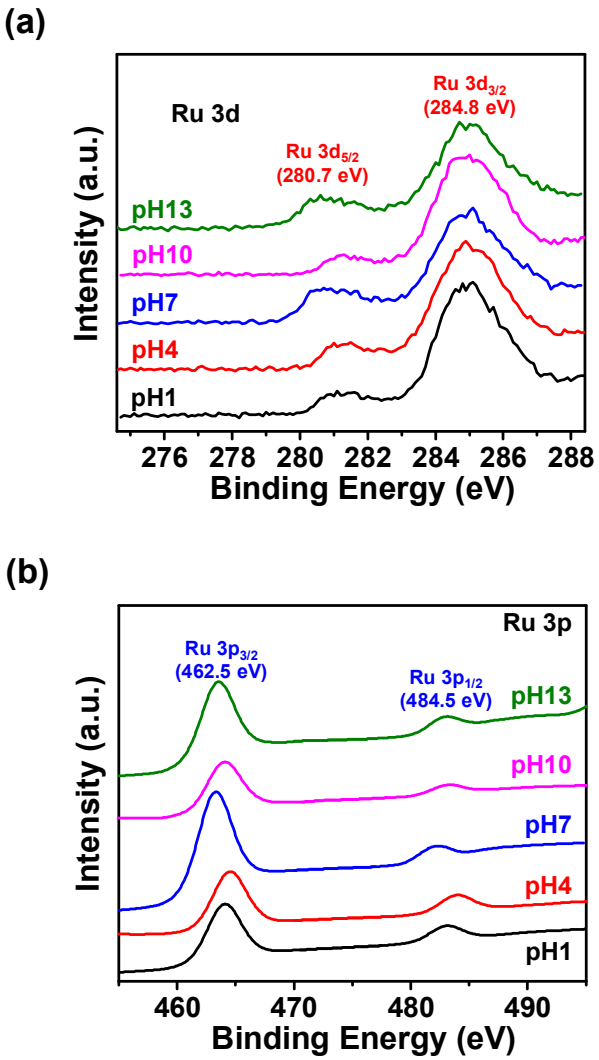

Figure 34. (a) Ru 3d and (b) Ru 3p high resolution X-ray photoelectron spectroscopy (XPS) analysis of Ru/CPPyNPs with diverse pH states (black: pH 1; red: pH 4; blue: pH 7; magenta: pH 10; green: pH 13).

3.2.3. Electrical characterization for acid and base solvents treated Ru/CPPyNPs

To verify the roles of acid and base solvents treatment in determining electrical properties of hybrid nanoparticles, the four-probe instrument was used to measure electrical conductivity of each hybrid nanomaterial. As shown in **Figure 35a**, the electrical conductivities of pH 1_Ru/CPPyNP, pH 4_Ru/CPPyNP, pH 7_Ru/CPPyNP, pH 10_Ru/CPPyNP, and pH 13_Ru/CPPyNP record 1.07 S cm^{-1}, 12.5 S cm^{-1}, 127 S $cm^{-1,}$ 209 S cm^{-1}, and 258 S cm^{-1} owing to protonation and structural changes of polypyrrole rings, respectively. Protonation of polypyrrole chains increases charge carrier (hole) density in polypyrrole and the electrical conductivity of polypyrrole increases. As an opposite phenomenon, deprotonation decreases charge carrier density of polypyrrole and the electrical conductivity decreases. Especially, huge decrement of electrical conductivities is observed in base solvents treated Ru/CPPyNPs. Similar tendency is found in current–voltage (*I–V*) curve measurement. Furthermore, current–voltage (*I–V*) curves were analyzed to estimate the electrical contact of Ru/CPPyNPs on the IDA gold alloy electrode surface. **Figure 35b** shows the I_{SD}-V_{SD} properties of each Ru/CPPyNP

treated with different acid and base solvents. The curves are linear forms for voltage from -0.1 V to 0.1 V and then the *dI/dV* value decreases with growing numbers of pHs for the solvents. According to the results, protonation of polypyrrole polymer rings enhanced the conductivity of the CPPyNPs and Ru/CPPyNPs attach on IDA gold electrode. Also, linearity of I_{SD}-V_{SD} properties explains good electrical contact between IDA gold alloy electrode and Ru/CPPyNPs, called ohmic contact. In result, acid and base treatments of Ru/CPPyNPs have no effect to electrical contact.

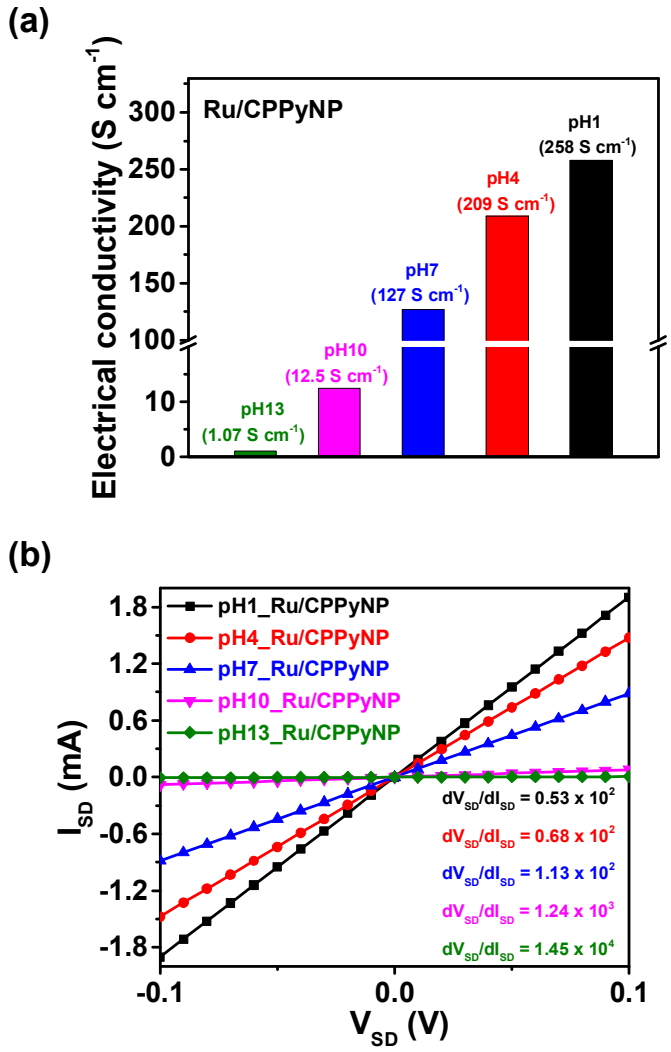

Figure 35. (a) Electrical conductivities and (b) I-V curves of different CPPyNP based hybrid nanomaterials (Black: pH 1_Ru/CPPyNP; Red: pH 4_Ru/CPPyNP; Blue: pH 7_Ru/CPPyNP; Magenta: pH 10_Ru/CPPyNP; Green: pH 13_Ru/CPPyNP).

3.2.4. Electrical measurement of acid and base treated Ru/CPPyNPs based hydrogen gas chemical sensor

Real-time measurement of acid and base treated Ru/CPPyNPs was processed to confirm the performance of hydrogen gas chemical sensor. To measure the sensing characteristics of the Ru/CPPyNPs based sensor electrode, the real-time responsive resistance changes were measured for different concentrations of hydrogen gas and are illustrated in **Figure 36a**. Ru/CPPyNPs with five different conditions (pH 1_Ru/CPPyNP, pH 4_Ru/CPPyNP, pH 7_Ru/CPPyNP, pH 10_Ru/CPPyNP, and pH 13_Ru/CPPyNP) were spread on electrode as transducer to detect hydrogen. Upon each exposure of hydrogen gas, the Ru/CPPyNP based electrodes exhibit an increase in resistance over several second period to reach a saturated value. When hydrogen flow to Ru/CPPyNP based electrode stops, the resistance of electrode returns to primary resistance before exposure to hydrogen gas with several second period. These effects are obtained by the catalytic chemical reaction between ruthenium and hydrogen gas. Each Ru/CPPyNP based electrode shows minimum detectable level (MDL) of hydrogen concentration as 0.5 ppm. Because hydrogen gas doesn't react to CPPyNPs, MDL of hydrogen is decided by the density of Ru

nanoparticles on CPPyNP surface. As mentioned before, Ru/CPPyNPs with same condition were used for hydrogen gas electrode so every electrode displays same MDL to hydrogen gas. However, each electrode demonstrates different sensitivity value for equivalent hydrogen concentration (**Figure 36b**). When pH value of Ru/CPPyNPs treated solvent increases, the resistance change ratio to initial resistance decreases. Because polypyrrole chain has *p*-type semiconductor characteristic, holes act as charge carrier to give electrical conductivity to polypyrrole rings. Acid treated polypyrrole chains show more protonated structure than neutral state polypyrrole chains with 3rd distilled water treatment. Therefore, pH 1_Ru/CPPyNP and pH 4_Ru/CPPyNP have increased charge carrier density compared to pH 7_Ru/CPPyNP. As a result, more charge carriers of acid treated Ru/CPPyNPs transfer through polypyrrole chains than pH 7_Ru/CPPyNPs and the changes of resistance are distinguished. Base treated Ru/CPPyNPs, pH 10_Ru/CPPyNP and pH 13_Ru/CPPyNP, display oppose tendency to those of acid treated Ru/CPPyNPs due to deprotonation phenomenon by base solvent treatment. Decrement of charge carrier density in polypyrrole chain causes decrement of resistance increment ratio. The sensitivity signal size decline by base

treated Ru/CPPyNPs is larger than the sensitivity signal size rise by acid treated Ru/CPPyNPs because the charge carrier density change is more dramatic in base solvent treated transducers.

Figure 36c shows the changes in sensitivity as function of pH values of Ru/CPPyNPs treated solvents for the composite nanoparticles, with respect hydrogen concentration. The sensitivity (S) is determined from the saturation point of the normalized resistance change, measured 20 s after the resistance change arrives at the highest point of normalized resistance change. As show in graph, whole Ru/CPPyNPs based sensor displays nonlinear changes in sensitivity at low concentration of hydrogen gas (0.5 to 1 ppm). But, linear behavior is observed over the wide range of concentrations (5 – 100 ppm). Therefore, the Ru/CPPyNP based sensor electrodes demonstrate reversible and reproducible responses to different analyte concentrations, and their responses are more pronounced as the gas concentration increased.

A profound research for response and recovery time of sensor was progressed for further investigation of sensor performance. 100 ppm of hydrogen gas concentration was identically used for measurement. The response times of Ru/CPPyNPs with different pH values are

demonstrated in **Figure 37a**. The response time of Ru/CPPyNP becomes shorter when the hydrogen ion concentration of Ru/CPPyNPs treated solvent increases. During the acidification, proton-acid doping occurred, and the β-C was preferentially protonated [118]. The change in the absorption peak of Raman spectroscopy for C=C stretching (**Figure 31a**) provided evidence that the doping structure of polypyrrole chains transfer from oxidized conjugated chain doped with counter anions to proton-acid doping after the acidification. The proton-acid doping is vital to improve the short-range ordering of polypyrrole backbone by increment of C=C stretching and conductivity of composite membrane owing to the efficient proton transport in the polypyrrole conjugated chains [119]. In other words, the charge carrier (hole) mobility increases by acidification of polypyrrole conjugated chains and this result influences the response time of Ru/CPPyNP based electrode to hydrogen gas. As a result, the response times of nanocomposite based sensor are 12 s, 23 s, 30 s, 56 s, and 78 s for pH 1_Ru/CPPyNP, pH 4_Ru/CPPyNP, pH 7_Ru/CPPyNP, pH 10_Ru/CPPyNP, and pH 13_Ru/CPPyNP, respectively. Same results are observed in recovery times of Ru/CPPyNP based sensors because charge carrier mobility

difference also influenced the charge carrier mobility during originating process (**Figure 37b**). The recovery times of nanocomposites based sensor are 32 s, 58 s, 78 s, 87 s, and 98 s for pH 1_Ru/CPPyNP, pH 4_Ru/CPPyNP, pH 7_Ru/CPPyNP, pH 10_Ru/CPPyNP, and pH 13_Ru/CPPyNP, respectively. The performance comparative table is figured in **Table 3**.

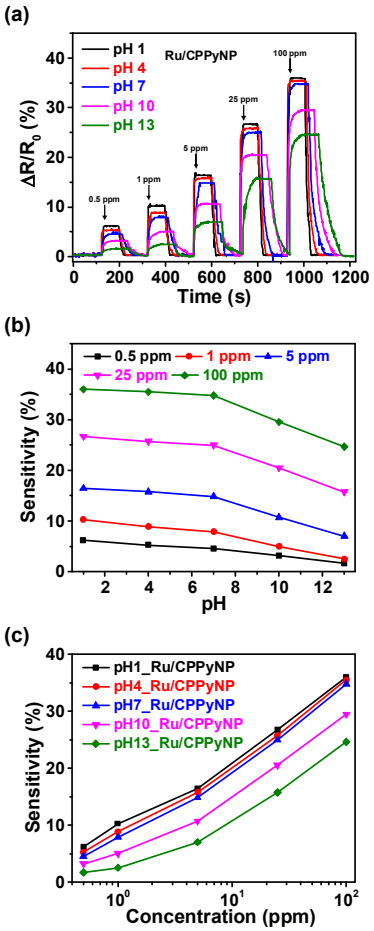

Figure 36. (a) Normalized resistance change upon sequential exposure to various concentrations of hydrogen gas, (b) Sensitivity change upon sequential pH difference with same hydrogen concentration, and (c) Calibration lines as function of hydrogen gas concentration (black: pH 1_Ru/CPPyNP; red: pH 4_Ru/CPPyNP; blue: pH 7_Ru/CPPyNP; magenta: pH 10_Ru/CPPyNP; green: pH 13_Ru/CPPyNP).

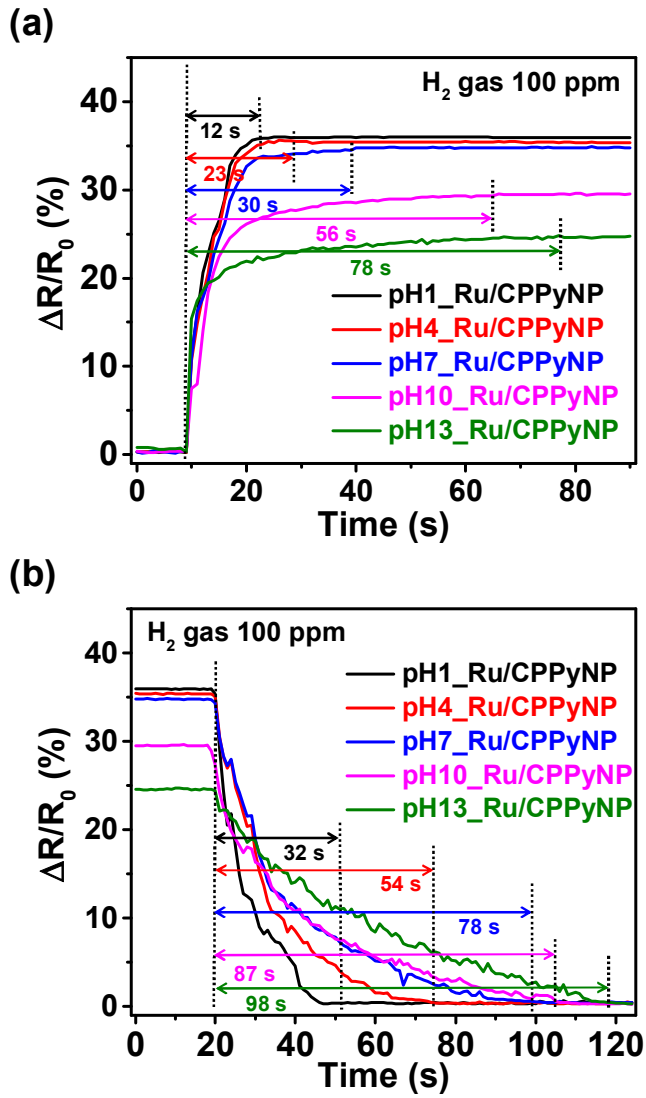

Figure 37. (a) Response and (b) recovery time of acid or base treated Ru/CPPyNPs with 100 ppm concentration hydrogen gas (black: pH 1_Ru/CPPyNP; red: pH 4_Ru/CPPyNP; blue: pH 7_Ru/CPPyNP; magenta: pH 10_Ru/CPPyNP; green: pH 13_Ru/CPPyNP).

Table 3. Hydrogen gas sensing ability of different pH values treated Ru/CPPyNPs.

Configuration	MDL[a]	Response time	Recovery time	S[b] for 25 ppm hydrogen
pH 1_Ru/CPPyNP	0.5 ppm	12 s	32 s	26.71 %
pH 4_Ru/CPPyNP	0.5 ppm	23 s	54 s	25.72 %
pH 7_Ru/CPPyNP	0.5 ppm	30 s	78 s	24.97 %
pH 10_Ru/CPPyNP	0.5 ppm	56 s	87 s	20.52 %
pH 3_Ru/CPPyNP	0.5 ppm	78 s	98 s	15.74 %

[a] minimum detectable level

[b] sensitivity

Excellent cycle stability is required for electrode materials in the practical implementation of sensor devices. **Figure 38a** presents the electrical response of various composite nanoparticles upon periodic exposure to 1 ppm of hydrogen gas at room temperature. These nanoparticles revealed a similar response for the sensitivity each time and the sensor was used without retardation of the response or recovery times. Moreover, composite CPPyNP based sensors maintained their sensing ability toward exposure to 1 ppm of hydrogen gas during 15 days (**Figure 38b**). This is because the structure of the CPPyNP layer prevents morphology collapse from the phase transition of ruthenium (Ru) to ruthenium halide (RuH_x) during hydrogen detection. Therefore, the Ru/CPPyNP based sensor electrodes exhibit high stability for repetitive hydrogen gas detection.

For further investigation to confirm the stability of Ru/CPPyNP based sensor electrodes, transmission electron microscopy (TEM) measurement was processed to display the states of Ru/CPPyNP before hydrogen sensing and after hydrogen sensing (**Figure 39**). As shown in figure, there is no morphological transition of Ru nanoparticles and CPPyNP. Consequentially, hydrogen sensing process doesn't affect the morphology of Ru/CPPyNP and the

Ru/CPPyNP based sensor electrodes demonstrate high stability for repetitive hydrogen gas detection procedure.

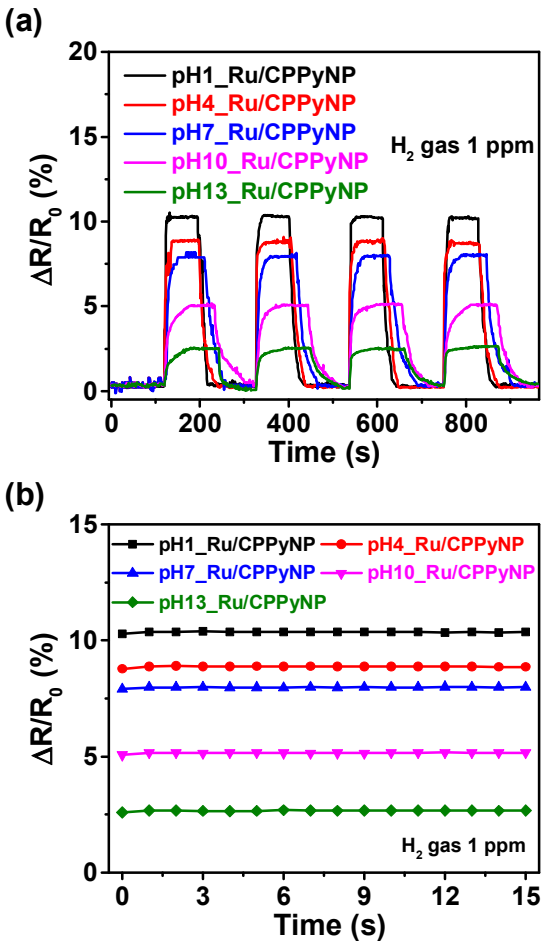

Figure 38. (a) Normalized resistance changes of different hybrid CPPyNPs upon sequential periodic exposure to 1 ppm of hydrogen gas. (b) Sensitivity changes of hybrid CPPyNPs with periodic exposure to 1 ppm of hydrogen gas for 15 days (black: pH 1_Ru/CPPyNP; red: pH 4_Ru/CPPyNP; blue: pH 7_Ru/CPPyNP; magenta: pH 10_Ru/CPPyNP; green: pH 13_Ru/CPPyNP).

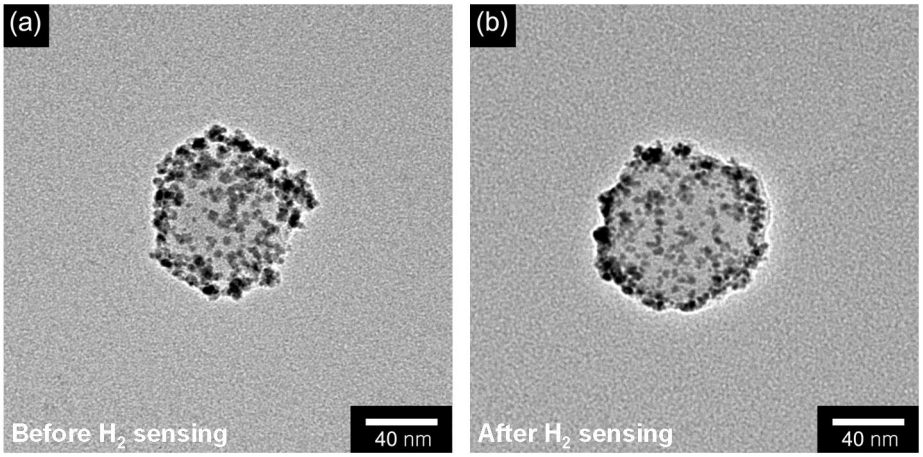

Figure 39. Transmission electron microscopy (TEM) images of Ru/CPPyNPs (a) before hydrogen sensing and (b) after hydrogen sensing.

3.3. Wireless hydrogen sensor application of Ru/CPPyNPs

3.3.1. Fabrication of UHF-RFID based wireless hydrogen gas sensor

Facile synthesis method was tried to fabricate wireless sensor using Ru/CPPyNP solution and ultrahigh frequency-radio frequency identification (UHF-RFID) antenna tag. Ru/CPPyNPs were bonded to passive UHF-RFID tag, containing a dipole antenna and an integrated circuit (IC) chip. **Figure 40** illustrates the detailed steps to modify UHF-RFID tag to wireless hydrogen gas sensor.

For the first step, UHF-RFID tag is covered with commercially available plastic tape to protect from damages, originated from Ru/CPPyNPs bonding process. Part of coating layer is removed and the cut-off part of coating layer is tuned to part of UHF-RFID aluminium tag. Ru/CPPyNPs can be attached stably on this part with chemical functionalization. Coating layer sticks tightly to UHF-RFID tag through press machine. For the next step, the tape-covered UHF-RFID tags are treated with oxygen (O_2) plasma and 3-aminopropyltrimethoxysilane (APTS) aqueous solution to create a specific functionalized region on the UHF-RFID tag. O_2 plasma treatment is actioned before APTS aqueous solution treatment to form

functional groups for APTS bonding on UHF-RFID tag. O_2 plasma treated UHF-RFID tag is soaked in APTS aqueous solution and the solution stirs more than 6 h to develop amino groups uniformly on UHF-RFID tag. In this sequence, diluted APTS aqueous solution, 5 wt% APTS aqueous solution, is used to prevent aggregation and membrane formation of APTS on UHF-RFID tag. Finally, Ru/CPPyNPs are bound to the functionalized region of the UHF-RFID antenna pattern through covalent bonding between the amino groups on the antenna pattern and carboxylic groups on the surface of Ru/CPPyNPs. Symbolically, the procedure of bonding is described:

$$\text{Ru/CPPyNPs} - \text{COOH} + \text{H}_2\text{N}(\text{CH}_2)_3\text{Si}(\text{O})_3 - \text{RFID antenna pattern}$$

$$\Rightarrow \text{Ru/CPPyNPs} - \text{CONH}(\text{CH}_2)_3\text{Si}(\text{O})_3 - \text{RFID pattern}$$

The covalent anchoring has the advantages of improving the union stability of Ru/CPPyNPs and UHF-RFID antenna pattern and enabling the formation of efficient electrical pathways during wireless sensing. Also, 4-(4,6-Dimethoxy-1,3,5-triazin-2-yl)-4-methylmorpholinium chloride (DMT-MM) 1wt% aqueous solution is injected in

Ru/CPPyNP aqueous solution to act as catalyst for peptide bond formation.

The real image of modified UHF-RFID tag as wireless hydrogen sensor is described in **Figure 41b**. With the naked eye, Ru/CPPyNPs are clearly attached on antenna pattern but the researcher used microscopy methods for further investigation. In **Figure 41a**, the boundary line of Ru/CPPyNPs and aluminium antenna pattern is observed by atomic force microscopy (AFM). The height of hydrogen sensing layer is measured by this method and it shows *ca.* 80 nm heights. Furthermore, field emission-scanning electron microscope (FE-SEM) was used to observe line of antenna pattern and Ru/CPPyNPs (**Figure 41c**). Ru/CPPyNPs spread uniformly on the surface and connect with antenna pattern smoothly.

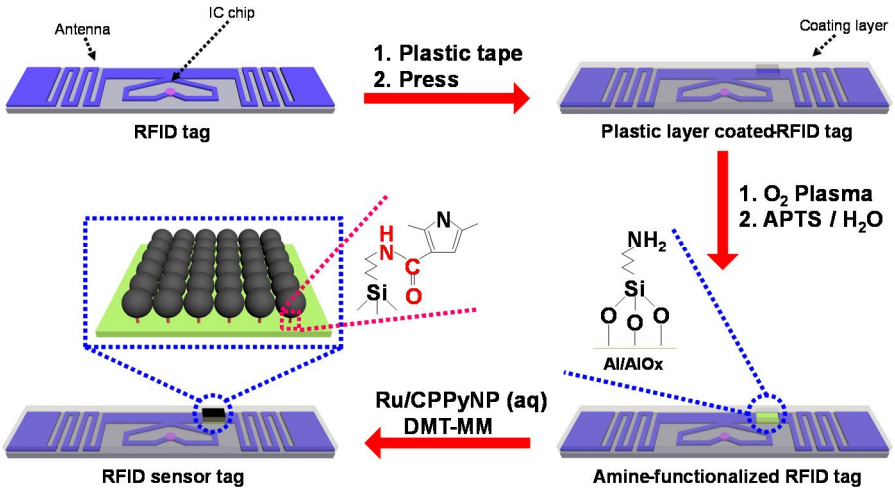

Figure 40. Schematic diagram of ultrahigh frequency-radio frequency identification (UHF-RFID) tag based hydrogen sensor with carboxyl functional groups covalently bonded to the aluminum film tag in the desired position.

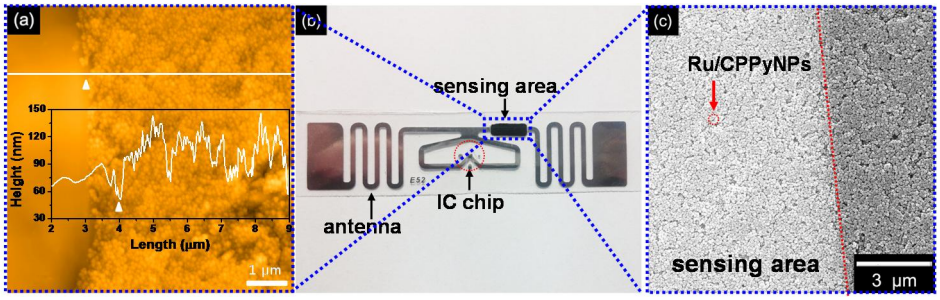

Figure 41. (a) Atomic force microscopy (AFM) image of Ru/CPPyNPs attached UHF-RFID tag as wireless sensor. (b) Photograph of the proposed UHF-RFID based gas sensor tag and (c) Field-effect scanning electron microscopy (FE-SEM) image of the Ru/CPPyNPs immobilized sensing area.

3.3.2. Wireless sensor measurements of Ru/CPPyNPs attached UHF-RFID tag

To initiate the wireless sensing, UHF-RFID antenna reader, which is connected to the network analyzer, is installed surrounding wireless sensor tag and emits an interrogation signal (**Figure 42**). The emitted electromagnetic field is absorbed by UHF-RFID tag and activates it. Then, the signal is reflected back to the RFID antenna reader, a process known as backscattering [120-122]. The response of wireless sensor tag is monitored in real-time by the network analyzer. When the mass flow controller (MFC) of hydrogen is operated and UHF-RFID wireless sensor tag is exposed to the hydrogen gas elements, the resistance of chemiresistive materials, Ru/CPPyNPs, is changed and it causes impedance mismatches between the dipole tag antenna and included IC chip. As a result, the network analyzer detects and displays the changes in the backscattering signal.

Figure 43a, **b**, and **c** display the change in the reflection amount radio frequency of diverse wireless sensor tags with different ratio of Ru (Ru/CPPyNP_0.5, Ru/CPPyNP_1.5, and Ru/CPPyNP_3.0, respectively) under the constant 2 min exposure to various concentration of hydrogen gas at room temperature. The distance of

measurement was 20 cm in a tale. The reflection signals are plotted as power of the radio waves reflected (Re, in dB) *versus* the frequency (MHz), as determined by the network analyzer. The UHF-RFID sensor tags without hydrogen exposing display largest reflectance among others due to outstanding impedance matching between antenna and IC chip. Also, there is no reflectance change of UHF-RFID tag when the sensor tag is exposed to nitrogen (N_2) gas more than 2 min. Therefore, N_2 gas is used to remove hydrogen residue after hydrogen sensing test. However, when the sensing layer of UHF-RFID tag is exposed to hydrogen gas, the hydrogen gas adsorbs on to Ru nanoparticles and electrons transfer to CPPyNPs, increasing the resistivity of the antenna. The increment of resistance becomes larger with the enhancement of the hydrogen gas concentration. The increasing resistance of tag antenna leads to impedance mismatching of between antenna and IC chip compared to no hydrogen exposure. Then, UHF-RFID sensor tag decreases radar cross section resulting in a diminish reflection [123]. Furthermore, similar to the IDA-based sensing system, the sensitivity of the wireless hydrogen sensor increases with Ru nanoparticle concentration on the surface of

CPPyNP (0.5 ppm for Ru/CPPyNP_0.5; 5 ppm for Ru/CPPyNP_1.5; 25 ppm for Ru/CPPyNP_3.0).

Figure 43d shows the wireless sensor response calibration (normalized reflection change) as a function of the hydrogen gas concentration. The normalized reflection change is expressed as $\Delta Re/Re_0 = (Re - Re_0)/Re_0$, where Re is the reflection after 2 min of hydrogen exposure and Re_0 is the reflectance at the beginning of the experiment. The normalized reflectance change of the radio waves increases with the hydrogen gas concentration for all sensor tag samples. Additionally, the reflectance difference (%) increases with the concentration of Ru particles on CPPyNP (26.39 % for Ru/CPPyNP_3.0; 9.43 % for Ru/CPPyNP_1.58; 4.53 % for Ru/CPPyNP_0.5 at 25 ppm of hydrogen). Furthermore, linear behavior is observed over a wide range of concentrations (1 – 100 ppm) for Ru/CPPyNP_3.0 based sensor tag. Therefore, the Ru/CPPyNP_3.0 based UHF-RFID tags demonstrate reversible and reproducible responses to different analyte concentrations, and their responses are more pronounced as the gas concentration increased. Other Ru/CPPyNP based tags with different Ru density on CPPyNP surface, Ru/CPPyNP_0.5 and Ru/CPPyNP_1.5, show similar

characteristic when they expose to various concentration of hydrogen gas. However, linear behaviors of these tags are observed with narrower range of hydrogen concentration than Ru/CPPyNP_3.0 based UHF-RFID tag because they have less Ru nanoparticles on CPPyNP surface than Ru/CPPyNP_3.0. From these results, UHF-RFID wireless hydrogen sensors are expected to apply on practical use.

Figure 44 demonstrates the reflectance alteration of wireless hydrogen sensors by the distance between UHF-RFID tag and antenna reader (**Figure 44a** for Ru/CPPyNP_0.5; **Figure 44b** for Ru/CPPyNP_1.5; **Figure 44c** for Ru/CPPyNP_3.0). When the hydrogen exposing concentration is fixed, the reflectance change decreases as the distance between wireless sensor tag and RFID antenna reader increase due to backscattering reducing effect with enhancement of remote distance. Furthermore, the researcher observes that the reflectance changes by remote distance are decreased with decrease of exposing hydrogen concentration.

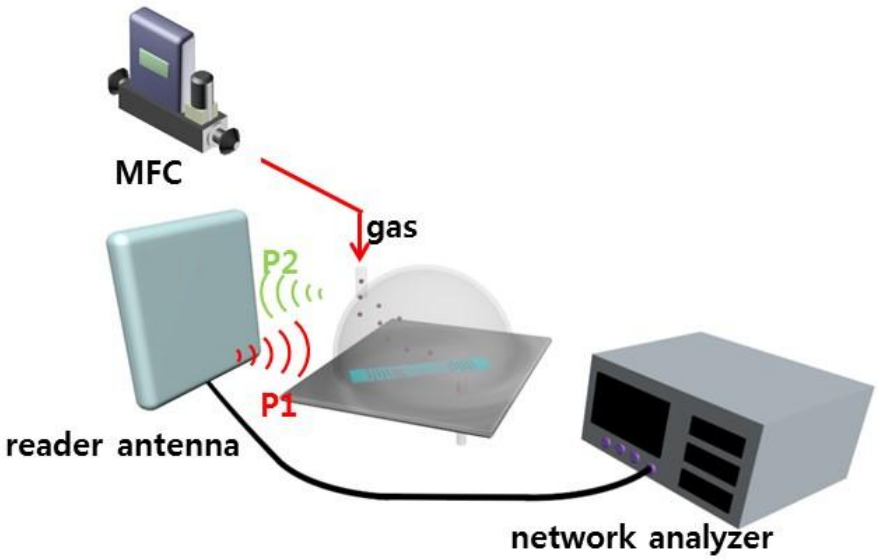

Figure 42. Schematic illustration of UHF-RFID based sensor system composed of UHF-RFID tag and antenna reader.

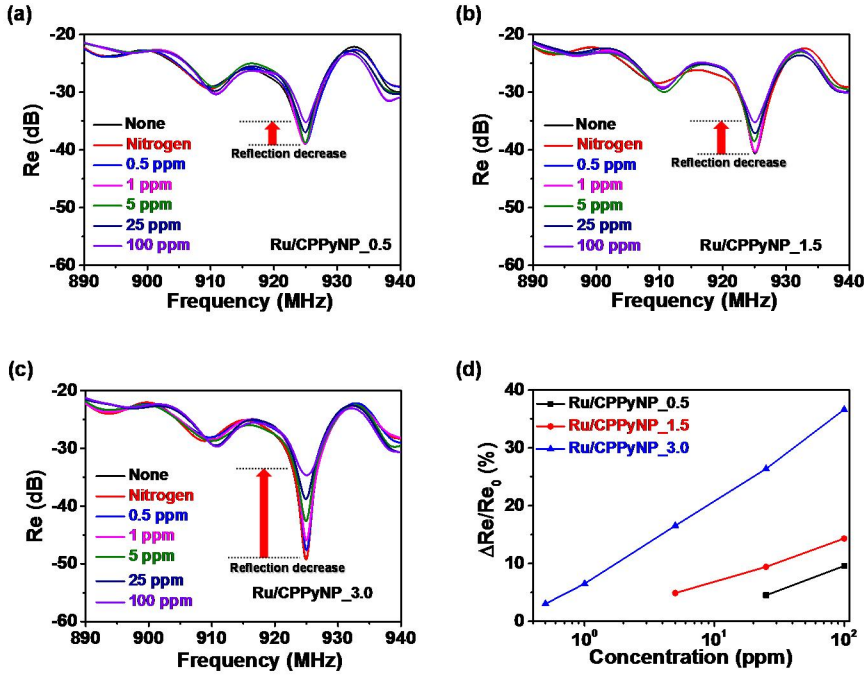

Figure 43. Changes in the reflectance properties of Ru/CPPyNP based wireless sensors with different Ru ratios: (a) Ru/CPPyNP_0.5; (b) Ru/CPPyNP_1.5; (c) Ru/CPPyNP_3.0. (d) The relationship between the concentration of hydrogen gas and the change of reflectance, which is calculated with $\Delta Re/Re_0 = (Re - Re_0)/Re_0$. Re_0 is the initial reflectance and Re is the reflectance after the exposure time of 2 min.

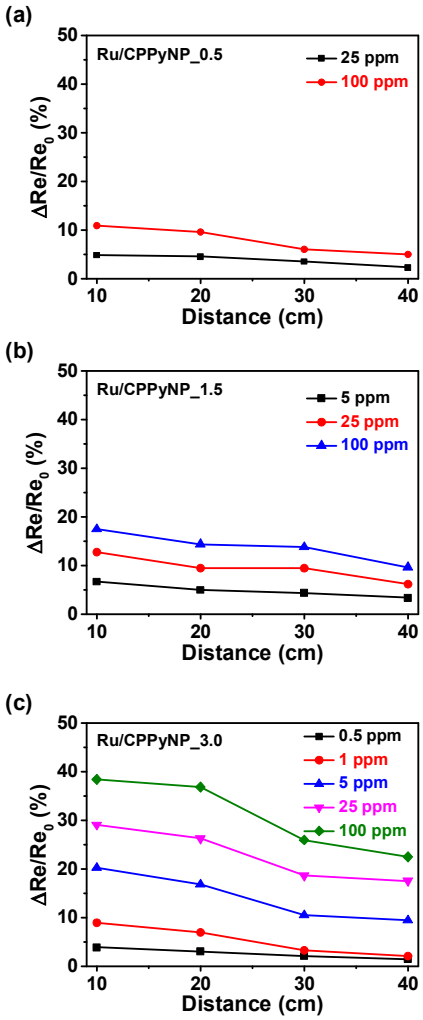

Figure 44. Reflectance calibration curves of different Ru/CPPyNP based wireless sensors as a function of distances between sensor electrode and antenna reader (10 - 40 cm): (a) Ru/CPPyN_0.5; (b) Ru/CPPyNP_1.5; (c) Ru/CPPyNP_3.0 (black: 0.5 ppm; red: 1 ppm; blue: 5 ppm; magenta: 25 ppm; green: 100 ppm).

Acid and base treated Ru/CPPyNP_3.0s (pH 1_Ru/CPPyNP, pH 4_Ru/CPPyNP, pH 7_Ru/CPPyNP, pH 10_Ru/CPPyNP, and pH 13_Ru/CPPyNP) are also applied to UHF-RFID tags for wireless hydrogen sensor. **Figure 45a - e** display the reflectance change under 2 min exposure of diverse hydrogen concentration. These wireless hydrogen sensors also don't react to nitrogen gas. So, N_2 gas was used to eliminate hydrogen residues from wireless hydrogen sensor too. All of these wireless hydrogen sensors show reaction to 0.5 ppm hydrogen gas, minimum detection level of Ru/CPPyN_0.5. Hence, the researcher can conclude that acid and base treatments don't influence detection limit of sensing nanomaterials due to preservation of Ru nanoparticles. However, the absolute figures of reflectance are increased with decrease of treated pH values. Because the resistances of Ru/CPPyNPs are decreased when treated pH values are decreased, the starting reflectances without hydrogen gas exposure are increased. But, the diminished percent of reflectance is almost same with all wireless hydrogen sensors because only state of ruthenium nanoparticles is transited by hydrogen gas and Ru nanoparticles maintain their forms despite of pH treatment. pH treatment just

changes the electrical state of CPPyNPs and transferred CPPyNPs are only related to mobility of charge carriers.

The reflectance variation of acid and base treated Ru/CPPyNPs based wireless hydrogen sensor was measured with distance change and featured in **Figure 46** except the data for pH 7 solvent treated Ru/CPPyNP because it overlaps with the measurement in **Figure 44c**. (**Figure 46a** for pH 1_Ru/CPPyNP; **Figure 46b** for pH 4_Ru/CPPyNP; **Figure 46c** for pH 10_Ru/CPPyNP; **Figure 46d** for pH 10_Ru/CPPyNP). When the hydrogen exposing concentration is fixed, the reflectance change decreases as the distance between wireless sensor tag and RFID antenna reader increase due to backscattering reducing effect with enhancement of remote distance. Furthermore, the researcher observes that the reflectance changes by remote distance are decreased with decrease of exposing hydrogen concentration. In addition, the acid treated Ru/CPPyNP and base treated Ru/CPPyNP show different tendency through the reflectance difference by remote distance. In acid treated case, the reflectance increases rapidly when the distance of antenna reader and wireless hydrogen sensor becomes closer. Especially, the transition from 30 cm to 20 cm makes the largest alteration of reflectance. On the other hand,

there are small gaps of reflectance by remote distance in base treated case. These consequences are originated from the electrical conductivity difference of sensing materials. The backscattering reducing effect by enhancement of remote distance is reduced by resistance increment of UHF-RFID tag antenna.

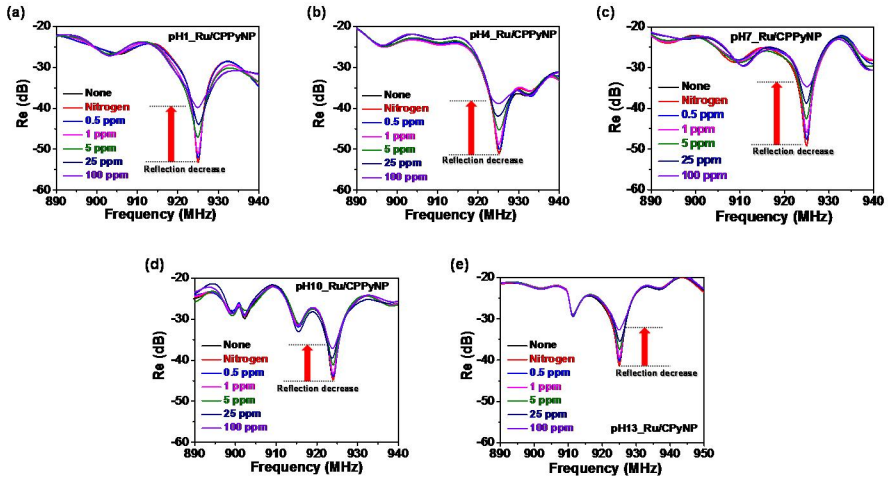

Figure 45. Changes in the reflectance properties of Ru/CPPyNP based wireless sensors with different pHs. Ru/CPPyNP_3.0 was commonly used for acid or base treatment: (a) pH 1 treated; (b) pH 4 treated; (c) pH 7 treated; (d) pH 10 treated; (e) pH 13 treated.

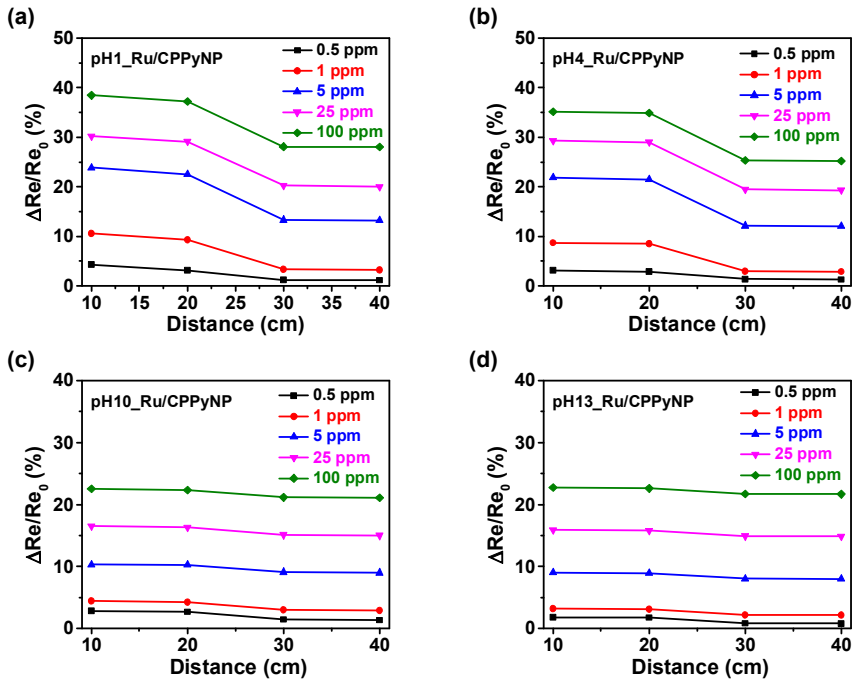

Figure 46. Reflectance calibration curves of different Ru/CPPyNP_3.0 based wireless sensors as a function of distances between sensor electrode and antenna reader (10 - 40 cm): (a) pH 1 treated; (b) pH 4 treated; (c) pH 10 treated; (d) pH 13 treated (black: 0.5 ppm; red: 1 ppm; blue: 5 ppm; magenta: 25 ppm; green: 100 ppm).

3.3.3. Flexibility test of Ru/CPPyNPs attached UHF-RFID tag for wireless hydrogen sensor

The flexibility test was processed with wireless hydrogen sensor to confirm the possibility for wearable and flexible device. The Ru/CPPyNPs attached UHF-RFID tag was deformed in the number of ways, such as bending, rolling or twisting. The deformed shapes are described in **Figure 47a - c**. **Figure 47d** displays the change in the resonance reflectance with formation of flat, rolling, and twisting. In rolling and twisting formation, the reflectances of modified UHF-RFID tag decrease slightly, compared to reflectance of flat formation: 2.09 % decrease for twisting formation; 4.18 % decrease for rolling formation. Because the electrical pathways are developed by connection of conducting nanoparticles, a part of connection is easily disconnected and minute crack is produced. As a result, the reflectance difference was observed.

For further investigation, the resistance of wireless hydrogen sensor tag was measured with bending formation. The sensor tag was inserted in bending machine and bended step by step. Detailed images of bending formations are featured in inset image of **Figure 48a**. As a result, the resistance of hydrogen sensor tag gradually increases when

the bending angle of UHF-RFID tag increases. On the other hand, different aspect is demonstrated in repetitive folding experiment for wireless hydrogen sensor. The sensor tag was folded for several times and the resistance was checked in flat formation for this experiment (**Figure 48b**). There is no resistance change over 200 times folding. As a result, the researcher convicts that the disconnection of electrical pathways among Ru/CPPyNPs is restored to original state with return to flat formation. For practical application of wireless hydrogen sensor to wearable and flexible device, the disconnection of sensing materials with deformed shapes must be upgraded.

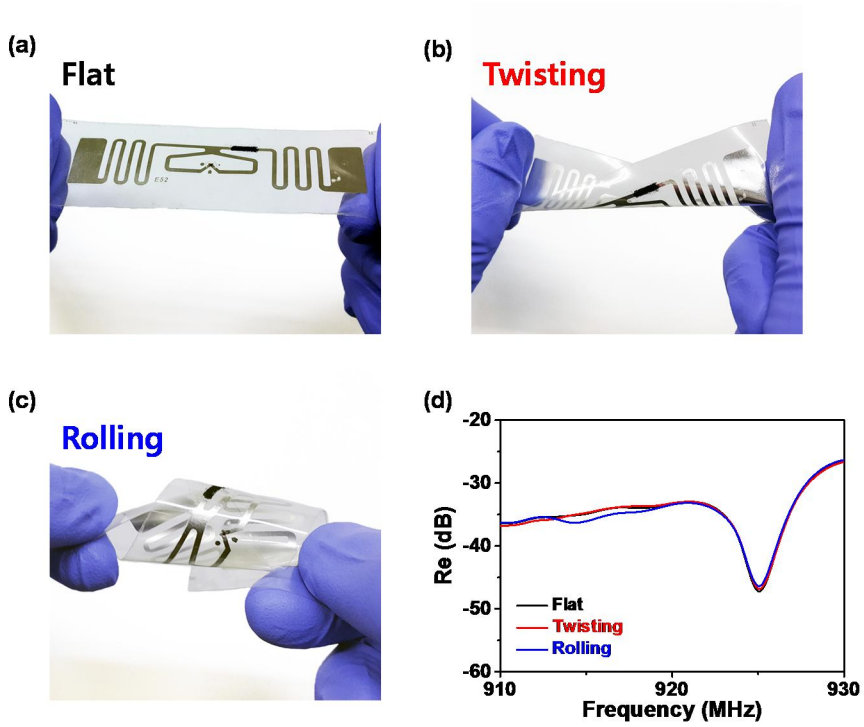

Figure 47. Photographs of the RFID tag sensor under different deformations (a) flat, (b) twisting and (c) rolling. (d) The normalized reflectance change under different deformations (black: flat; red: twisting; blue: rolling).

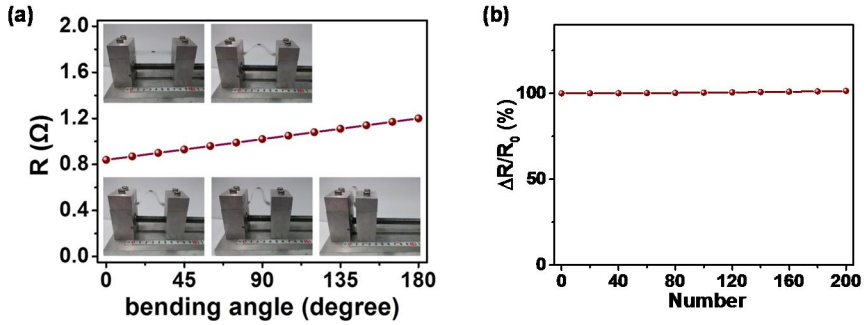

Figure 48. (a) Relative change in the resistance of the UHF-RFID sensor tag with different bending angles (inset: photo images of diversely bended UHF-RFID sensor tag). (b) The resistance of the UHF-RFID sensor tag after repetitive foldings.

4. Conclusion

Ruthenium nanoparticles decorated carboxylated polypyrrole nanoparticle (Ru/CPPyNP) was fabricated successfully by chemical reduction and ultrasonication process and employed in chemical and wireless hydrogen gas sensor. Controlling the density of Ru nanoparticles on CPPyNP surface and doping level of hybrid nanocomposites by acid and base solvents are also observed profoundly in this dissertation. The subtopics are concluded in the view point of each subtopic as follows:

1. Ru/CPPyNPs are facilely fabricated by stirring and ultrasonication methods and Ru nanoparticles are uniformly decorated on the surface of CPPyNPs. Charge-charge bonding between the Ru^{3+} ions and the negative charge of the O atom of the carboxylate group in the CPPy structure induces the attachment of Ru nanoparticles on the CPPy surface. Also, the density of Ru nanoparticles on the CPPyNP surface is easily controlled by concentration of Ru precursor in CPPyNP aqueous solution. Ru/CPPyNPs based hydrogen sensor electrodes show different performance by the Ru nanoparticles density on CPPyNPs because the hydrogen gas detection is obtained by catalytic chemical reaction

between ruthenium and hydrogen gas. Minimum detectable level (MDL) of Ru/CPPyNPs based hydrogen sensor is 0.5 ppm and linear detection range from 5 ppm to 100 ppm. Furthermore, increment of Ru nanoparticles on CPPyNP surface leads to shorter response time due to enhanced surface area of Ru/CPPyNP by Ru nanoparticles and longer recovery time owing to the increased amount of phase transferred materials.

2. Phase and structural transition of Ru/CPPyNPs by treatment of acid and base solvents are researched in this part. Polypyrrole chain structure in CPPyNP was reversibly transferred among neutral, polaron, and bipolaron states. However, metal nanoparticles on CPPyNP surface didn't change their states whether strong acid and base solvents are applied to nanocomposites or not. Structural transition of Ru/CPPyNPs effect the performance of Ru/CPPyNPs based hydrogen gas sensor. Acid solvent treated Ru/CPPyNPs display the increased resistance change and decreased response and recover times because the charge carrier (hole) density and mobility in polypyrrole chain grow larger due to bipolaron state of polypyrrole chain. On the other hand, base solvent treated Ru/CPPyNPs represent the opposite tendency of resistance

change, response time, and recovery time because the charge carrier (hole) density and mobility of polypyrrole chain decrease owing to neutral state of polypyrrole chain. There was no alteration in MDL because detection limit was only influenced by Ru nanoparticles density on the surface of CPPyNP.

3. Strong and stable bonding between passive wireless tag and transducers is one of the most important factors to apply the passive RFID tag as wireless smart sensor. Therefore, the covalent bondings, peptide bondings, between UHF-RFID tag and Ru/CPPyNPs were induced to make strong and stable bonds. Oxygen (O_2) plasma and (3-aminopropyl)triethoxy silane (APS) treatments were suggested on the part of UHF-RFID tag to introduce amine groups. These groups make peptide bond with carboxyl functional groups on Ru/CPPyNP surface. This object was observed by atomic force microscopy (AFM) and scanning electron microscopy (SEM) to confirm strong bonding. Furthermore, the reflectance change of wireless hydrogen sensor was detected by signal between antenna reader and UHF-RFID tag. The reflectance signal decreased during exposure to hydrogen gas owing to resistance increment of Ru/CPPyNPs and the degree of decrement

become bigger when the hydrogen gas concentration increases. Also, the wireless hydrogen sensor tag shows increment of resistance in bending formation. However, it maintains original resistance when it returns to flat formation from bending formation. The wireless sensor demonstrates few possibility of wearable sensor.

References

[1] G. A. Snook, P. Kao, A. S. Best, *J. Power Sources* **2011**, 196, 1.

[2] H. Shirakawa, *Angew. Chem. Int. Ed.* **2001**, 40, 2574.

[3] J. Jang, *Book Series: Advances in Polymer Science* **2006**, 199, 189.

[4] T.-H. Le, Y. Kim, H. Yoon, *Polymers* **2017**, 9, 150.

[5] R. Blueocean, Y. Kim, H. Yoon, *Electrical and Electrochemical Properties of Conducting Polymers*, **2017**.

[6] A. G. MacDiarmid, R. J. Mammone, R. B. Kaner, L. Porter, R. Pethig, A. J. Heeger, D. R. Rosseinsky, R. J. Gillespie, P. Day, *Philosophical Transactions of the Royal Society of London. Series A, Mathematical and Physical Sciences* **1985**, 314, 3.

[7] R. Kumar, *Conducting Polymers: Synthesis, Properties and Applications*, **2015**.

[8] B. Philip, J. Xie, J. K Abraham, V. Varadan, *A new synthetic route to enhance polyaniline assembly on carbon nanotubes in tubular composites*, **2004**.

[9] Y. Zhang, P. Blom, *Electron and hole transport in poly(fluorene-benzothiadiazole)*, **2011**.

[10] A. Nollau, M. Pfeiffer, T. Fritz, K. Leo, *Controlled n-type doping of a molecular organic semiconductor: Naphthalenetetracarboxylic dianhydride (NTCDA) doped with bis(ethylenedithio)-tetrathiafulvalene (BEDT-TTF)*, **2000**.

[11] Y. Zhang, B. de Boer, P. Blom, *Controllable Molecular Doping and Charge Transport in Solution-Processed Polymer Semiconducting Layers*, **2009**.

[12] P. Camurlu, *RSC Advances* **2014**, 4, 55832.

[13] E. M. Genies, G. Bidan, A. F. Diaz, *Journal of Electroanalytical Chemistry and Interfacial Electrochemistry*

1983, 149, 101.

[14] J. Jang, J. H. Oh, X. L. Li, *J. Mater. Chem.* **2004**, 14, 2872.

[15] A. O. Patil, A. J. Heeger, F. Wudl, *Chem. Rev.* **1988**, 88, 183.

[16] O. Inganäs, R. Erlandsson, C. Nylander, I. Lundström, *J. Phys. Chem. Solids* **1984**, 45, 427.

[17] H. Münstedt, *Polymer* **1986**, 27, 899.

[18] W. Yu, S. U. S. Choi, *Journal of Nanoparticle Research* **2004**, 6, 355.

[19] M. Lazzari, M. A. López-Quintela, *Adv. Mater.* **2003**, 15, 1583.

[20] C. N. R. Rao, A. K. Cheetham, *J. Mater. Chem.* **2001**, 11, 2887.

[21] J. Wang, *Analyst* **2005**, 130, 421.

[22] A. Erdem, *Talanta* **2007**, 74, 318.

[23] E. G. Barbagiovanni, D. J. Lockwood, P. J. Simpson, L. V. Goncharova, *Applied Physics Reviews* **2014**, 1, 011302.

[24] S. Tedesco, D. Sheehan, *Nanomaterials as Emerging Threats*, **2010**.

[25] C. L. Chen, S. R. Hwang, W.-H. Li, K.-C. Lee, G.-C. Chi, H.-T. Hsiao, C.-G. Wu, *Enhanced Electroluminescence of Polymer Light-Emitting Diodes with Direct Polyaniline Synthesized Anodes*, **2002**.

[26] N. E. Kamchi, B. Belaabed, J.-L. Wojkiewicz, S. Lamouri, T. Lasri, *J. Appl. Polym. Sci.* **2013**, 127, 4426.

[27] S. Cho, S. H. Hwang, C. Kim, J. Jang, *J. Mater. Chem.* **2012**, 22, 12164.

[28] H. Yoon, M. Chang, J. Jang, *Adv. Funct. Mater.* **2007**, 17, 431.

[29] J. Jang, K. J. Lee, Y. Kim, *Chem. Commun.* **2005**, DOI: 10.1039/B503831F3847.

[30] S. Ko, J. Jang, *Angew. Chem. Int. Ed.* **2006**, 45, 7564.

[31] Y. Xia, B. Gates, Y. Yin, Y. Lu, *Adv. Mater.* **2000**, 12, 693.

[32] F. S. Bates, *Science* **1991**, 251, 898.

[33] D. Zhao, J. Feng, Q. Huo, N. Melosh, G. H. Fredrickson, B. F. Chmelka, G. D. Stucky, *Science* **1998**, 279, 548.

[34] S. K. Pillalamarri, F. D. Blum, A. T. Tokuhiro, J. G. Story, M. F. Bertino, *Chem. Mater.* **2005**, 17, 227.

[35] S. Besson, T. Gacoin, C. Ricolleau, C. Jacquiod, J.-P. Boilot, *J. Mater. Chem.* **2003**, 13, 404.

[36] I. Kang, F. W. Wise, *Journal of the Optical Society of America B* **1997**, 14, 1632.

[37] A. M. Prokhorov, *Great Soviet encyclopedia*, Macmillan, **1982**.

[38] G. K. Mor, O. K. Varghese, M. Paulose, C. A. Grimes, *Adv. Funct. Mater.* **2005**, 15, 1291.

[39] J. Jang, J. H. Oh, *Adv. Mater.* **2003**, 15, 977.

[40] J. Jang, X. L. Li, J. H. Oh, *Chem. Commun.* **2004**, DOI: 10.1039/B316881F794.

[41] A. Y. Men'shikova, *Nanotechnologies in Russia* **2010**, 5, 35.

[42] J. Jang, J. H. Oh, G. D. Stucky, *Angew. Chem. Int. Ed.* **2002**, 41, 4016.

[43] M.-C. Daniel, D. Astruc, *Chem. Rev.* **2004**, 104, 293.

[44] N. L. Rosi, C. A. Mirkin, *Chem. Rev.* **2005**, 105, 1547.

[45] J. L. Elechiguerra, J. L. Burt, J. R. Morones, A. Camacho-Bragado, X. Gao, H. H. Lara, M. J. Yacaman, *Journal of nanobiotechnology* **2005**, 3, 6.

[46] J. Greeley, J. K. Norskov, M. Mavrikakis, *Annu. Rev. Phys. Chem.* **2002**, 53, 319.

[47] M. T. Reetz, E. Westermann, *Angewandte Chemie (International ed. in English)* **2000**, 39, 165.

[48] Y. Nishihata, J. Mizuki, T. Akao, H. Tanaka, M. Uenishi, M. Kimura, T. Okamoto, N. Hamada, *Nature* **2002**, 418, 164.

[49] A. Züttel, *Materials Today* **2003**, 6, 24.

[50] R. S. GEONMONOND, A. G. M. D. SILVA, P. H. C.

CAMARGO, *An. Acad. Bras. Cienc.* **2018**, 90, 719.
[51] S. Chen, D. L. Carroll, *Nano Lett.* **2002**, 2, 1003.
[52] G. S. Métraux, C. A. Mirkin, *Adv. Mater.* **2005**, 17, 412.
[53] R. Jin, Y. C. Cao, E. Hao, G. S. Metraux, G. C. Schatz, C. A. Mirkin, *Nature* **2003**, 425, 487.
[54] C. A. Foss, G. L. Hornyak, J. A. Stockert, C. R. Martin, *The Journal of Physical Chemistry* **1994**, 98, 2963.
[55] X. Liu, C. Li, J. Xu, J. Lv, M. Zhu, Y. Guo, S. Cui, H. Liu, S. Wang, Y. Li, *The Journal of Physical Chemistry C* **2008**, 112, 10778.
[56] S. Zhu, F. Li, C. Du, Y. Fu, *Sens. Actuator B-Chem.* **2008**, 134, 193.
[57] A. J. Haes, R. P. Van Duyne, *J. Am. Chem. Soc.* **2002**, 124, 10596.
[58] D. B. Cairns, M. A. Khan, C. Perruchot, A. Riede, S. P. Armes, *Chem. Mater.* **2003**, 15, 233.
[59] S. F. Lascelles, S. P. Armes, *J. Mater. Chem.* **1997**, 7, 1339.
[60] Y. Bao, W. An, C. H. Turner, K. M. Krishnan, *Langmuir* **2010**, 26, 478.
[61] M. Logar, B. Jancar, A. Recnik, D. Suvorov, *Nanotechnology* **2009**, 20, 275601.
[62] J. Hu, Y. Liu, *Langmuir* **2005**, 21, 2121.
[63] J. S. Lee, O. S. Kwon, S. J. Park, E. Y. Park, S. A. You, H. Yoon, J. Jang, *ACS Nano* **2011**, 5, 7992.
[64] K. Xiao, Y. Liu, T. Qi, W. Zhang, F. Wang, J. Gao, W. Qiu, Y. Ma, G. Cui, S. Chen, X. Zhan, G. Yu, J. Qin, W. Hu, D. Zhu, *J. Am. Chem. Soc.* **2005**, 127, 13281.
[65] Y. Lu, G. L. Liu, L. P. Lee, *Nano Lett.* **2005**, 5, 5.
[66] T. Peng, W. Sun, C. Huang, W. Yu, B. Sebo, Z. Dai, S. Guo, X. Z. Zhao, *ACS Appl Mater Interfaces* **2014**, 6, 14.

[67] *Nanocomposites*.

[68] P. Prins, L. P. Candeias, A. J. J. M. van Breemen, J. Sweelssen, P. T. Herwig, H. F. M. Schoo, L. D. A. Siebbeles, *Adv. Mater.* **2005**, 17, 718.

[69] S. Porel, S. Singh, S. S. Harsha, D. N. Rao, T. P. Radhakrishnan, *Chem. Mater.* **2005**, 17, 9.

[70] A. M. Azad, S. A. Akbar, S. G. Mhaisalkar, L. D. Birkefeld, K. S. Goto, *J. Electrochem. Soc.* **1992**, 139, 3690.

[71] B. Bourrounet, T. Talou, A. Gaset, *Sens. Actuator B-Chem.* **1995**, 27, 250.

[72] N. Barsan, M. Schweizer-Berberich, W. Göpel†, *Fresenius. J. Anal. Chem.* **1999**, 365, 287.

[73] E. Schaller, J. O. Bosset, F. Escher, *LWT - Food Science and Technology* **1998**, 31, 305.

[74] K. Ihokura, J. Watson, *The stannic oxide gas sensor: Principles and applications*, **2017**.

[75] H. Yoon, M. Chang, J. Jang, *J. Phys. Chem. B* **2006**, 110, 14074.

[76] S. Ko, J. Jang, *Biomacromolecules* **2007**, 8, 182.

[77] O. S. Kwon, S. J. Park, H. Yoon, J. Jang, *Chem. Commun.* **2012**, 48, 10526.

[78] T. Seiyama, A. Kato, K. Fujiishi, M. Nagatani, *Anal. Chem.* **1962**, 34, 1502.

[79] I.-D. Kim, A. Rothschild, H. L. Tuller, *Acta Mater.* **2013**, 61, 974.

[80] B. Cho, J. Yoon, M. G. Hahm, D.-H. Kim, A. R. Kim, Y. H. Kahng, S.-W. Park, Y.-J. Lee, S.-G. Park, J.-D. Kwon, C. S. Kim, M. Song, Y. Jeong, K.-S. Nam, H. C. Ko, *J. Mater. Chem. C* **2014**, 2, 5280.

[81] M. G. Chung, D.-H. Kim, D. K. Seo, T. Kim, H. U. Im, H. M.

Lee, J.-B. Yoo, S.-H. Hong, T. J. Kang, Y. H. Kim, *Sens. Actuator B-Chem.* **2012**, 169, 387.

[82] L. Huang, Z. Wang, J. Zhang, J. Pu, Y. Lin, S. Xu, L. Shen, Q. Chen, W. Shi, *ACS Appl. Mater. Interfaces* **2014**, 6, 7426.

[83] V. Dua, S. P. Surwade, S. Ammu, S. R. Agnihotra, S. Jain, K. E. Roberts, S. Park, R. S. Ruoff, S. K. Manohar, *Angew. Chem. Int. Ed.* **2010**, 49, 2154.

[84] Y. Awano, presented at 2009 IEEE International Electron Devices Meeting (IEDM), 7-9 Dec. 2009, **2009**.

[85] H. Yoon, J. Jang, *Adv. Funct. Mater.* **2009**, 19, 1567.

[86] G. Korotcenkov, S. D. Han, J. R. Stetter, *Chem. Rev.* **2009**, 109, 1402.

[87] S. K. Arya, S. Krishnan, H. Silva, S. Jean, S. Bhansali, *Analyst* **2012**, 137, 2743.

[88] Y. H. Hu, L. Zhang, *Adv. Mater.* **2010**, 22, E117.

[89] J. L. Johnson, A. Behnam, S. J. Pearton, A. Ural, *Adv. Mater.* **2010**, 22, 4877.

[90] C. Fournier, K. Rajoua, M. L. Doublet, F. Favier, *ACS Appl Mater Interfaces* **2013**, 5, 310.

[91] J. Shao, W. Xie, X. Song, Y. Zhang, *Sensors* **2017**, 17, 2144.

[92] X. Chen, G. Wu, Z. Cai, M. Oyama, X. Chen, *Microchim. Acta* **2014**, 181, 689.

[93] J. T. Farrar, V. K. Zworykin, J. Baum, *Science* **1957**, 126, 975.

[94] R. S. Mackay, *Nature* **1964**, 204, 355.

[95] H. Messer, A. Zinevich, P. Alpert, *Science* **2006**, 312, 713.

[96] R. A. M. Receveur, F. W. Lindemans, N. F. d. Rooij, *Journal of Micromechanics and Microengineering* **2007**, 17, R50.

[97] W. J. Fleming, *New Automotive Sensors—A Review*, **2008**.

[98] R. Joro, P. Dastidar, V. Iivonen, H. Ylänen, S. Soimakallio, *NADINE: New approaches to detecting breast cancer by*

sequential μm-wavelength imaging with the aid of novel frequency analysis techniques, **2012**.

[99] K. Finkenzeller, *RFID Handbook: Fundamentals and Applications in Contactless Smart Cards and Identification*, Wiley, **2003**.

[100] H. Lehpamer, *RFID Design Principles*, **2008**.

[101] A. P. Sample, D. J. Yeager, P. S. Powledge, A. V. Mamishev, J. R. Smith, *IEEE Transactions on Instrumentation and Measurement* **2008**, 57, 2608.

[102] R. A. Potyrailo, C. Surman, N. Nagraj, A. Burns, *Chem. Rev.* **2011**, 111, 7315.

[103] J. Jun, J. Oh, D. H. Shin, S. G. Kim, J. S. Lee, W. Kim, J. Jang, *ACS Appl. Mater. Interfaces* **2016**, 8, 33139.

[104] H. Yoon, M. Chang, J. Jang, *The Journal of Physical Chemistry B* **2006**, 110, 14074.

[105] L. Qiu, B. Liu, Y. Peng, F. Yan, *Chem. Commun.* **2011**, 47, 2934.

[106] X. Q. Zeng, M. L. Latimer, Z. L. Xiao, S. Panuganti, U. Welp, W. K. Kwok, T. Xu, *Nano Lett.* **2011**, 11, 262.

[107] J. Kong, M. G. Chapline, H. Dai, *Adv. Mater.* **2001**, 13, 1384.

[108] F. Favier, E. C. Walter, M. P. Zach, T. Benter, R. M. Penner, *Science* **2001**, 293, 2227.

[109] Y. Pak, S.-M. Kim, H. Jeong, C. G. Kang, J. S. Park, H. Song, R. Lee, N. Myoung, B. H. Lee, S. Seo, J. T. Kim, G.-Y. Jung, *ACS Appl. Mater. Interfaces* **2014**, 6, 13293.

[110] D.-T. Phan, G.-S. Chung, *Sens. Actuator B-Chem.* **2014**, 199, 354.

[111] P. V. Tong, N. D. Hoa, N. V. Duy, V. V. Quang, N. T. Lam, N. V. Hieu, *Int. J. Hydrogen Energy* **2013**, 38, 12090.

[112] G. Cho, B. M. Fung, D. T. Glatzhofer, J.-S. Lee, Y.-G. Shul,

Langmuir **2001**, 17, 456.

[113] R. Liu, Y. Liu, Q. Kang, A. Casimir, H. Zhang, N. Li, Z. Huang, Y. Li, X. Lin, X. Feng, Y. Ma, G. Wu, *RSC Advances* **2016**, 6, 9402.

[114] R. Rajagopalan, J. O. Iroh, *Appl. Surf. Sci.* **2003**, 218, 58.

[115] K. Idla, A. Talo, H. E.-M. Niemi, O. Forsén, S. Yläsaari, *Surf. Interface Anal.* **1997**, 25, 837.

[116] X. Zhang, R. Bai, *Langmuir* **2002**, 18, 3459.

[117] J. Joo, J. K. Lee, S. Y. Lee, K. S. Jang, E. J. Oh, A. J. Epstein, *Macromolecules* **2000**, 33, 5131.

[118] Y. Li, G. He, *Synth. Met.* **1998**, 94, 127.

[119] K. Cheah, M. Forsyth, V. T. Truong, *Synth. Met.* **1998**, 94, 215.

[120] J. S. Lee, J. Oh, J. Jun, J. Jang, *ACS Nano* **2015**, 9, 7783.

[121] J. M. Azzarelli, K. A. Mirica, J. B. Ravnsbæk, T. M. Swager, *Proceedings of the National Academy of Sciences* **2014**, 111, 18162.

[122] S. Manzari, A. Catini, G. Pomarico, C. D. Natale, G. Marrocco, *IEEE Sensors Journal* **2014**, 14, 3616.

[123] L. Fiddes, N. Yan, *RFID tags for wireless electrochemical detection of volatile chemicals*, **2013**.

국문초록

최근 우수한 물성과 전기적, 화학적 성능을 보이는 나노재료의 연구와 개발에 대해 지대한 관심이 있다. 특히, 무기물과 유기물을 결합한 복합나노재료는 각 물질의 상호작용으로 서로의 단점을 보완하고 우수한 물성을 보이기에 많은 산업분야에서 연구가 진행 중이다. 그 중에서도 금속과 전도성 고분자를 결합한 복합나노재료는 고분자의 낮은 기계적 특성을 보완해주고 금속 나노재료의 응집 현상을 막아주어 높은 안정성을 가지고 있다. 또한 뛰어난 성능의 전기적 특성을 가지고 있기 때문에 전기화학센서, 형광센서, 촉매, 에너지 변환 및 저장 장치에서 주목 받고 있다. 하지만, 현재 일정한 형태의 복합나노재료를 제조하는 기술이 부족하고 적용하는 금속 또한 백금, 금, 은 등의 안정성이 높은 귀금속에만 국한되어 있기 때문에 더 많은 연구가 필요한 상황이다.

스마트 화학센서는 트랜스듀서를 기반으로 하는 장치로 특징 있는 환경적 요소들을 감지하는데 뛰어난 성능을 보인다. 센서는 타겟물질을 감지하는 센싱 트랜스듀서가 필요한데 이

트랜스듀서는 전기, 온도, 형광 등 다양한 신호의 변화를 통해 타겟물질을 감지할 수 있으며 트랜스듀서가 감지한 신호를 디지털 신호로 바꾸어 디지털 기기를 통해 타겟물질의 유무 및 농도 변화를 확인하여 위험하고 폭발 가능성이 있는 기체에 대해 미리 알려주는 역할을 할 수 있기에 뛰어난 성능을 가진 센서는 많은 산업분야에서 유용하게 사용될 수 있다. 따라서, 뛰어난 감지 성능을 가지는 센싱 트랜스듀서 물질개발은 중요한 요소 중 하나이다. 뛰어난 성능을 판단하는 기준은 다음의 6가지 기준을 제시할 수 있다: 1) 높은 감도; 2) 넓은 범위의 감지 농도; 3) 타겟물질에 대한 선택성; 4) 빠른 감지와 회복 속도; 5) 반복감지에 대한 안정성; 6) 상온에서의 감지가능, 이렇게 6가지의 성능에 대한 테스트가 필요하다.

본 학위 논문에서는 전도성 고분자의 일종인 폴리피롤 나노입자 위에 금속물 중 하나인 루테늄 나노구조물이 올라간 일정한 형태의 금속과 전도성 고분자의 하이브리드 복합나노재료를 간단하고 창의적인 방법을 이용하여 제조하고, 이들의 전기적 물성을 체계적으로 고찰하여 센서용 트랜스듀서로 적용하는 연구를 기술하였다.

우선, 카르복실기를 함유한 폴리피롤 나노입자를 제조하고

이를 분산한 수용액에 루테늄 전구체를 넣어 초음파처리와 화학적 환원을 통해 루테늄 나노입자가 일정하게 박힌 폴리피롤 나노입자를 제조하였다. 이때, 루테늄 전구체의 농도를 조절하여 폴리피롤 나노입자 표면에 도입되는 루테늄 나노입자의 밀도를 조절하였으며 루테늄 나노입자의 밀도에 따른 수소 감지성능을 비교하였다. 그 결과, 루테늄 나노입자의 밀도가 증가함에 따라 센서가 감지할 수 있는 수소가스의 농도가 낮아지고 더 넓은 농도범위의 수소가스를 감지할 수 있는 것을 확인하였다.

더 나아가, 산 용액과 염기 용액을 이용하여 복합나노입자에 화학적 처리를 했을 시 루테늄 나노입자와 폴리피롤 나노입자에 어떤 구조적 변화가 발생하고 이 변화가 수소감지 성능에 미치는 영향에 대하여 연구하였다. 결과에 따르면 산과 염기 용액 처리에 의해서 루테늄 나노입자의 구조에는 변화가 생기지 않는 것을 확인하였다. 하지만, 처리하는 용액의 pH가 낮아질수록 폴리피롤의 고분자 구조가 이중 분극자 형태의 구조를 가지는 것을 확인 할 수 있었다. 이에 따라 트랜스듀서가 수소를 감지하는 속도와 감지 후 원상태로 회복하는 속도가 더 빨라지는 것을 확인 할 수 있었다. 감지농도와 감지가능한 농도범위에는 큰 변화가

발생하지 않는 것을 통해 수소감지에는 루테늄이 필수적으로 필요한 것 또한 확인 가능하였다.

마지막으로, IoT 시대가 도래함에 따라 이에 맞춰 제조한 트랜스듀서를 무선센서로 응용하는 연구를 진행하였다. 수동적 RFID 무선태그를 이용하면 배터리가 없이 신호를 주고 받을 수 있어 소형화가 가능하고 환경을 고려하지 않고 어디에든 적용가능한 무선센서를 제조할 수 있다. 이를 위해 RFID 무선태그의 일정부분에 산소 플라즈마와 화학적 처리를 통하여 아미노 관능기를 도입하였고 촉매를 이용하여 폴리피롤 나노입자 표면의 카르복실기와 공유결합시켜 안정적이고 단단하게 트랜스듀서 물질을 RFID 무선태그 표면에 도입하는 실험을 진행하였다. 그 결과, 수소가스의 유무에 따라 무선신호가 변화하는 것을 확인하였고 농도의 변화에 따라서도 신호변화 크기가 달라져 농도 측정 또한 가능한 것을 확인하였다.

정리하면, 본 학위 논문에서는 폴리피롤 나노입자 표면에 루테늄 나노입자를 고르게 도입하여 표면적이 극대화되고 수소에 대하여 선택적으로 반응할 수 있는 복합나노재료를 제조하였으며 수소화학센서와 무선센서로 응용 가능성에 대한 연구를 수행하였다. 본 학위 논문에서 사용된 간단하고

독창적 제조방법과 구조 변형 방법들은 다양한 나노물질의 제조에도 응용 가능할 것으로 기대된다.

주요어: 복합나노재료; 폴리피롤; 루테늄; 스마트 화학센서; 무선센서; 수소가스

학 번: 2014-22613

감사의 글

대학원 생활을 시작할 때 5년간의 긴 생활을 어떻게 견디나 했는데 떠날 때가 되니 아쉬움이 더 많이 남습니다. 흔히들 박사과정은 자기 자신과의 외로운 싸움이라 하는데 주변의 응원해주시는 분들과 동료분들이 함께하였기에 외롭지 않은 행복한 박사과정을 보낸 것 같습니다. 그 고마운 분들께 감사의 인사를 전하며 이 박사학위 논문을 끝마치고자 합니다.

먼저 가족들에게 감사의 인사를 전하고자 합니다. 박사과정동안 경제적으로 정신적으로 부족함이 없게 물심양면 지원해주신 부모님, 인생의 평생친구이자 귀여운 여동생에게 감사드립니다. 앞으로 인생을 살면서 받은만큼 갚으며 함께 살아갔으면 좋겠습니다.

저를 제자로 받아주신 지도교수님, 장정식교수님께 감사인사를 드립니다. 항상 부족한 제자였음에도 불구하고 타박하지 않으시고 지켜보시며 박사로서의 마음가짐과 큰 물줄기를 제시해주시고 바른 길로 인도해주셨기에 박사학위를 받을 수 있지 않았나 싶습니다. 사회에 나가서도 가르침을 마음에 새기고 교수님 이름에 누가 되지 않도록

정진하겠습니다. 졸업 후 기회가 될 때마다 찾아뵙고 감사의 마음을 전하고자 합니다. 아울러 새벽마다 저의 건강을 염려해주시고 기도해주신 사모님께도 큰 감사를 드립니다.

5년간 박사과정을 하면서 정말 많은 연구실 동료분들과 함께 생활하였습니다. 그 중 특히 인연이 깊었고 감사한 분들께도 인사를 전하고자 합니다. 먼저 사수와 부사수 관계를 맺어 함께 연구를 진행했던 사수 이준섭형 그리고 부사수 정고은누나에게 감사합니다. 이준섭형은 사수로써 저에게 연구의 기본을 가르쳐주었습니다. 때로는 혹독하게 가르침을 전해주셨지만 그런 가르침이 없었다면 지금의 저는 없었을 거라 생각합니다. 부사수 정고은누나와의 생활을 통해서는 누군가에게 연구를 가르치고 지도하는 방법을 배웠습니다. 두 분과는 1~2년의 짧은 생활만을 함께하였지만 제 박사과정 중 가장 중요한 배움을 함께하였기에 기억에 가장 남습니다.

다음으로 연구실 동기였던 유해준형, 이경섭형, 조경희누나, 그리고 김윤기형에게 인사를 전합니다. 서로 다른 분야를 연구했기에 연구적 교류는 적었지만 같은 순간을 함께하고 같은 고민을 겪는 사람들이 함께한다는 것만으로도 마음 속 깊은 위로와 버팀목이 되었습니다. 모두 사회에 나가 자신이

원하는 바 이룰 수 있도록 앞날을 축복하겠습니다.

센서팀 선배들과 후배들께도 감사인사를 전하고자 합니다. 선배였던 신동훈형, 안지현형, 박진욱형, 전재문형에게 먼저 감사인사를 드립니다. 이분들과 함께하여 연구실생활이 힘들지만은 않은 즐거운 생활이었습니다. 특히 전재문형은 사수인 이준섭형이 졸업하고 나서 생활적으로도 연구적으로도 아직 부족할 때 사수의 역할을 해주셔서 큰 고마움을 느낍니다. 졸업후배인 김성근형, 나원주형, 김우영에게도 감사인사를 전합니다. 연구실 인원이 줄어들 때 함께 교수님의 과제들을 많이 진행했었던 기억들이 납니다. 모두들 남은 박사과정 무사히 끝마치고 성공적인 사회생활 하실 수 있길 기원합니다.

정말 마지막으로 지면상 언급하지 못한 함께 생활했던 연구실 모든 분들께 감사인사를 전합니다. 앞으로 제 인생에 또 어떤 일들이 펼쳐질지는 저도 아직 알지 못하지만 연구실에서의 경험들은 미래의 일들과 어려움을 해결해나가는데 큰 도움이 될 것을 믿어 의심치 않습니다. 그동안 감사했습니다.

오정균 드림